Smoothed Particle Hydrodynamics Simulations Of Colliding Molecular Clouds.

(*Thesis submitted to the University Of Wales at Cardiff in fulfillment of the requirements of the degree of Doctor Of Philosophy.*)

by
Mr. Sumedh. V. Anathpindika
(September 2008)

"... A law in sense-'a natural law'-is describing a strict, unvarying regularity which either in fact holds in nature (in this case, the law is a true statement)or does not hold (in this case, it is false). If we do not know whether a law of nature is true or false, and if we wish to draw attention to our uncertainty, we often call it an 'hypothesis'. A law of nature is unalterable; there are no exceptions to it. For if we are satisfied that something has happened which contradicts it, then we do not say that there is an exception or an alteration to the law, but rather our hypothesis has been refuted, since it has turned out that the supposed strict regularity did not hold, or in other words, that the supposed law of nature was not a true law of nature, but a false statement. Since laws of nature are unalterable, they can be neither broken nor enforced. They are beyond human control, although the may possibly be used for technical purposes, and although we may get into trouble by not knowing them, or by ignoring them."

-- Sir Karl Popper in
(The Open Society And Its Enemies - Vol. 1; p. 59)

ProQuest LLC
789 East Eisenhower Parkway
P.O. Box 1346
Ann Arbor, MI 48106-1346

Acknowledgments

Monuments may be envisaged by the engineers, but are realised by the dexterous and lugubrious workers, toiling away day in and day out. The monument so constructed is the direct outcome of the sweat and blood invested by these humble people. Similarly, the present work has seen sterling contributions from several people without which, tit would have been well neigh impossible. I take this opportunity to thank them all.

I must begin by expressing my humble gratitude and obeisance to the champions of the depressed classes in India. It is solely due to the illustrious leadership and intellectual lacuna of stalwarts like Mahatma Phule, His Highness Shahu Maharaj, Dr. B. R. Ambedkar among others, that I am in the gratuitous position, I currently find myself in, and can think of elevating it in future. Next, I thank the State Government Of Maharashtra (India) for awarding their prestigious scholarship for meritorious candidates belonging to one of the most downtrodden communities of the state, in the name of His Highness Shahu Maharaj. This scholarship accounted for 90% of the expenses borne by myself towards the completion of this work. The remainder 10% was provided by the George Education Trust, London. I whole heartedly thank the esteemed trust.

I also take this opportunity to humbly thank a few of my teachers who have played a significant role in making me what I am, including my parents. I begin by thanking my mathematics teachers in in the higher secondary, Mr S. Naik and Mr A. Shankarnarayan (both St' Vincent's High School & Junior College, Pune). I specially thank my mathematics teachers in the senior college, Dr. V. V. Acharya, Dr. S.R. Kulkarni and Mr P.S. Bagul (all Fergusson College, Pune University). Special thanks to Prof. J.V. Khedkar (Head Of Electronics Department, Fergusson College, Pune University) and Dr. S. B. Ogale (Department Of Superconductivity, Maryland University; now scientist at National Chemical Laboratories, Pune), who in many ways have acted as my mentors and provided invaluable guidance and support. I also thank my astronomy teachers, Dr. J. Chengalur (NCRA - TIFR, Pune), Prof. K. Subramanian (IUCAA, Pune) and Dr. P. Subramanian (IISER, Pune).

I express my sincere gratitude to my thesis supervisor

and guide for the present research, Prof. A. P. Whitworth. It was extremely pleasurable to have his expertise. The present work couldn't have been possible without his diligent supervision. I also thank Prof. D. Ward-Thompson for his guidance on an associated project. In this same regard, I also thank Dr. David Nutter for his kind assistance in helping out with some astronomical software packages and making available processed data for part of this project. I take this opportunity to thank Dr. James Di Francesco for providing processed data for rest of the project.

The simulations for the current work were performed using the SPH code DRAGON. I thank Dr. Simon Goodwin for making available the latest version of the code. I also thank Dr. David Hubber for his assistance in various related matters. All the column density plots in the present work have been prepared using the graphics and analysis package SPLASH, prepared by Dr. Daniel Price. I am extremely thankful to him for his help and efforts in sorting a few technical issues with it.

Also special thanks to Dr. R. Weunch for his generous aid towards using supporting graphics packages. I also thank all my friends and colleagues here for their direct/indirect, major/minor contribution. I also take this opportunity to thank the technical staff for their prompt and efficient services. I must also thank -
Mr. P. Dummett (Fees officer, Finance department, Cardiff university) and Dr. R. Jones (Chief Coordinator, International Office, Cardiff university) for their special efforts in helping with important technical matters.

Abstract

The galactic disk is largely composed of hot, rarefied gas also called the inter cloud medium (ICM). The cooler regions of the ICM are dominated by molecular species and dust. Immersed in this neutral medium are dense agglomerations of primarily H_2, called giant molecular clouds (GMCs). The GMCs have a velocity dispersion of order a few km s^{-1}, superimposed on their orbital motion. A GMC, over a single period of rotation of the galaxy, may undergo a few tens of collisions. In the present work, we investigate this rather violent phenomenon and examine the prospects of star formation in the post collision composite gas body. The star formation code, DRAGON, employed for the present work is ill equipped to study the effects of cloud collision on the chemical composition of the ICM.

We draw a distinction between the regime of high velocity (precollision Mach numbers in excess of ten) and low velocity (precollision Mach numbers of order unity) cloud collisions, on the basis of the evolution of the gas slab produced in either cases. While the former leads to the formation of a dense shock compressed gas slab, the latter results in a dense pressure compressed gas slab. We observe that strong internal shear in a shock compressed slab suppresses gravitational instability in it.

In particular, we observe evidence for the non-linear thin shell instability (NTSI) in the shocked slab formed in a head-on cloud collision. The slab thus dissipates thermal energy and upon the loss of thermal support, collapses to form a thin, long filament along the collision axis. Star formation proceeds in this filament. There is however, no evidence of the NTSI in the oblique shocked slab resulting from off centre cloud collisions, although it is dominated by internal shearing motion.

On the other hand, the pressure compressed slab is dominated by gravitational instability and fragments, when the fatsest growing mode dominates. The slab develops a number of floccules, which merge to form larger clumps and filamentary structures. The densest regions in these large scale structures then collapse gravitationally. We suggest this as a possible mechanism for the formation of star clusters.

YSOs forming in filamentary structures are fed with material streaming along the axis of respective filaments. This material also transfers angular momentum to the accreting protostellar core and the attendant accretion disk is orthogonal to the angular momentum vector of this inflowing material. In the filaments resulting from the collapse of the post-collision shocked slab in a head-on cloud collision, we observe that the accretion disks circumscribing

the sinks, are orthogonal to the filament.

However, the gas slab resulting from a low velocity, off centre cloud collision is wrapped around by angular momentum and gravitationally fragments to form filaments. This slab tumbles in the plane of the collision (and therefore the axis about which it tumbles, comes out of this plane), the filaments in the slab also tumble with it. In the process they become offset relative to each other and feed angular momentum to the candidate protostellar core along the direction normal to the angular momentum axis. Thus, any attendant accretion disk is expected to be parallel to the filament (also the angular momentum) axis (Whitworth *et al*, 1995).

To test this hypothesis, we collated data for YSOs located in filamentary star forming regions, and outflows originating from them. The scope of our work was limited and restricted to only five filamentary star forming regions in the local universe.

Outflows from YSOs generally have small opening angles and are approximately normal to the circumstellar disk. Under this premise, we can get an idea of the orientation of the circumstellar disks relative to their natal filaments. We concluded that 72% outflows were distributed within $\sim 45^\circ$ of being orthogonal to their natal filaments and 28% were distributed within $\sim 45^\circ$ of being parallel to their natal filaments. It is difficult to make a strong claim simply on the basis of this work, which therefore needs to be extended. None the same, it tends to support the mechanism elucidated by Whitworth *et al* (1995).

Contents

Chapter 1

Introduction

Humanity has always been fascinated by the mysterious heavenly bodies. The underlying curiosity to unravel the mystery of these celestial bodies has impelled mankind towards finding a solution to it. The grand question pertains to the universe itself, but on the microlevel there is a more fundamental problem, that of understanding how stars form. This phenomenon is not unique to the present epoch only, but has been traced to the early universe at redshifts greater than five.

The problem of star formation has been studied in great theoretical depths in the past (e.g. Mestel, 1965). Now, with improved computing facilities, it is possible to model certain features of star formation. However, modelling the effects of outflows and including various radiative mechanisms is computationally challenging. Another limitation on numerical codes is the computational expense incurred. Currently these issues are being addressed with great impetus. The study of star formation is computationally demanding since it spans more than twenty orders of magnitude in density.

Models of star formation may for simplicity, be classified into two types (a) the quiescent mode and (b) the dynamical mode. The work discussed in this thesis though, belongs to category (b). The distinction between the modes of star formation however, is not rigorous. A violent phenomenon like for instance, a shock front impinging on a cloud surface compresses the cloud and may induce gravitational collapse in it, i.e. a dynamical mode leading to the quasistable evolution of prestellar cores.

Star formation : According to the currently understood picture of star formation, sufficiently dense regions which are gravitationally unstable collapse

under self gravity. The collapse continues till a protostellar core that is in hydrodynamic equilibrium is formed. This leaves an envelope of gas around the infant core. The core continues to accrete matter from this envelope by forming an accretion disk around itself. The process of accretion transfers angular momentum to the protostar and spins it up. On the other hand, the protostar losses angular momentum through highly collimated outflows and disk winds (Larson, 2007).

The protostellar object evolves through phases 0, I and finally ends up as a T - Tauri star. The T - Tauri stars themselves are classified into two types viz. the classical T - Tauri stars (CTTS, the class II phase) and the weak line T - Tauri stars (WTTS, the class III phase). The classification of various prestellar phases is done on the basis of the amount of mass accreted by the protostar from the envelope cocooning it (Andrè *et al*, 1993), while the WTTS are characterised by the emission lines from singly ionised heavy elements. Stars seldom form in isolation and are found in clusters and the most massive stars occupy the centre of the cluster.

However, the exact process leading to the formation of a star cluster is debated. Two models have been proposed in this regard, one being that of simple gravitational fragmentation (hierarchical fragmentation) and the other being that of competitive accretion. The former process involves fragmentation of a gravitationally unstable core into a number of small cores which then collapse under self gravity to form a single or multiple system. The Jeans mass (M_J) is given as,

$$M_J \sim \left(\frac{\pi k_B}{G m_p \mu}\right)^{\frac{3}{2}} \cdot T^{\frac{3}{2}} \cdot \rho^{\frac{-1}{2}},$$

(Rees, 1976); where m_p is the mass of a proton, μ is the mean molecular weight and k_B is the Boltzmann constant. Observe that the Jeans mass depends strongly on the temperature (T).

Gravitationally collapsing objects can fragment into smaller cores as long as they can cool efficiently and increasing density lowers the Jeans mass, as can be seen from the above equation for M_J. This process is called hierarchical fragmentation. The fragmentation process terminates as soon as the fragments become opaque, after which their evolution becomes adiabatic. Heat can no longer be radiated and the Jeans mass increases rapidly.

Low & Lynden - Bell (1976) estimated the minimum mass of fragments to be a fraction of $M_\odot$ ($\sim$ 0.01 $M_\odot$). They also showed that the fragment mass had a very weak dependence on opacity i.e. a change by a factor of

10^7 in opacity produces a change in the fragment mass by only a factor of 10. However, the gas temperature and density depend more strongly on opacity. The fragments so formed at the end of gravitational fragmentation, presumably go on to form stars. In this eventuality, we would expect the knee of the stellar initial mass function (IMF) to occur at $\lesssim 0.1$ $M_\odot$, contrary to this, it is observed at ~ 0.3 $M_\odot$. I will briefly discuss the IMF in the next section.

On the other hand, according to the competitive accretion model, unbound gas is accreted by star forming clumps. As the name suggests, collapsing clumps compete to accrete gas from the parent core. This theory predicts protostellar seeds of much smaller masses compared to the typical mass of a star (~ 0.5 $M_\odot$). These protostellar seeds then accrete matter form the parent core. Numerical simulations tend to support this theory and show that some stars accrete much more than others do. The process of accretion is highly non uniform (Bonnell *et al*, 1997).

However, this is usually the case since the models considered in numerical simulations are highly simplified. The physical conditions assumed, in no way represent the actual star forming regions. In fact Krumholz *et al* (2005) have argued on the basis of Virial mass of spherical and filamentary star forming regions, to show that the accretion rates predicted by the competitive accretion theory do not agree with those inferred from observations. Simple isothermal models of turbulent molecular clouds produce a network of dense filaments. The density is the highest in regions where these filaments intersect. These are also the regions where prestellar cores form and fragment gravitationally to form star clusters and each protostellar object accretes matter competitively (Klessen & Burkert, 2000).

Young protostars produce jets while the most massive stars emit strong ionising radiation, which has significant effect on the ambient medium. Obviously, isothermal models do not account for such feedback effects. However, according to Bonnell & Bate (2006) the effects of stellar feedback cannot be used to argue against the competitive accretion model since the dynamical time scale over which this feedback operates is generally of order $10^3 - 10^4$ yrs, while on the other hand the cluster dynamic timescale is of order few times 10^5 yrs, which is much greater than the time scale of the feedback.

The competitive accretion theory seems to hinge on the mass of the protostellar seeds, the choice of which does not seem to have any objective criterion. The slope of the IMF so determined, can be easily manipulated by suitably tailoring the seed mass. The Jeans mass argument is theoret-

ically established. A self gravitating clump would undergo gravitational collapse and increasing density will reduce the Jeans mass, as noted above. Sufficiently large individual fragments may form tightly bound multiple systems.

These fragments oscillate for some time before undergoing a catastrophic collapse. Boyd & Whitworth (2004), for instance have shown that the minimum mass of a fragment in turbulent cloud cores is $\sim$0.005 $M_{\odot}$. The matter of virial equilibrium of turbulence within clouds has been recently revisited by Field, Blackman & Keto (2008) where they studied various scaling relations.

The other important issue is that of the energy budget involved in this process. The outflows are highly energetic and travel at velocites of 10 to 100 km s^{-1} as a result of which they can easily pierce the gas envelope around the cluster and escape, hence most of the energy and momentum is deposited outside the envelope (Reipurth & Bally, 2001). Stellar winds are less energetic and deposit energy in the cluster following which it is likely to be disrupted. Even in this eventuality, accretion by individual protostellar objects may slow down but it does not appear to stop. See also Li & Nakamura (2006). While, if there is not much energy deposited through feedback then the process of star formation can continue in the parent clump.

Observations of various star forming regions show that stars form in clusters and the most massive stars in a particular cluster occupy the centre of the cluster potential, which is in agreement with the findings of competitive accretion models. This is because, as a protostellar object continues to accrete matter, it becomes more massive and slowly sinks to the bottom of the cluster potential. The process of accretion thus leads to the segregation of stars that are massive and those that are less massive. This affects the respective slopes of the stellar IMF in the high mass and low mass regimes (Bonnell *et al*, 2001 a & b).

While thus far, we have reviewed the possible fate of self gravitating clumps there are yet other clumps which are thermally supported against self gravity and do not undergo a catastrophic collapse. These starless cores are called Bok globules (Bok, 1948). Cores like L1544, B68, L1529 for instance, are examples under this category. Velocity dispersion studies of the interior of B68, for example, suggest that it is an oscillating core (Lada *et al*, 2003). Radial oscillations of starless cores have been theoretically studied by modelling them as Bonnor - Ebert spheres and deriving the amplitudes of radial

oscillations. This analysis has been performed in the linear regime (Keto *et al*, 2006) and then extended to the non linear regime for B68, in particular (Broderick *et al*, 2007).

1.1 The Stellar IMF :

We know that stars form in collapsing prestellar cores. Stellar masses range from a fraction of a solar mass to a few tens of solar masses. The distribution of stellar masses at the initial epoch of star formation (SF) is called the stellar Initial Mass Function (IMF). However, since the stars observed at the present epoch were formed billions of years ago, the exact nature of their mass distribution at the time of their birth is unknown.

The stellar mass distribution has to be inferred from the luminosity measurements, corresponding to which the luminosity function (LF) is defined. Mass - Luminosity relations can then be invoked to obtain the present day stellar mass function (PDMF) (Chabrier, 2003). This problem has been under investigation for a long time and was first tackled by Salpeter (1955). Based on the then available data, he defined the LF ($\phi(M_v)$), the mass function $\xi(M)$ and the total luminosity function $\psi(M_v)$. See Equations (1), (2) & (3) in Salpeter (1955). Here M_v is the absolute visual magnitude and M is the stellar mass.

The stellar IMF is defined as the number of stars N in a volume of space V at a time t per logarithmic mass interval dlog m

$$\xi(\log m) = \frac{d\left(\frac{N}{V}\right)}{d\log m} = \frac{dn}{d\log m}, \tag{1.1}$$

where $n = \frac{N}{V}$ is the stellar number density. Equation (1.1) is also written in an alternative form to give the stellar mass distribution per mass interval, as

$$\xi(m) = \frac{dn}{dm} = \frac{1}{m \cdot (\ln 10)} \cdot \xi(\log m). \tag{1.2}$$

With these two forms of the IMF, the exponents also differ and the IMF can be simply written as : $\xi(\log m) \propto m^{-x}$ & $\xi(m) \propto m^{-\alpha}$; $x = \alpha - 1$ with $\alpha = 2.35$ and $x = 1.35$ (the Salpeter exponent). He found that the curve resulting from the plot of $\xi(M)$ against M could be approximated

reasonably well by the power-law,

$$\xi(M) \propto \left(\frac{\mathrm{M}}{\mathrm{M}_{\odot}}\right)^{-1.35}, \tag{1.3}$$

for large mass stars with masses in the range $\sim$ 0.5 $\mathrm{M}_{\odot}$ - 10 $\mathrm{M}_{\odot}$ only.

Stars on the main sequence slowly move up in the H-R diagram as they consume their fuel and may either become red giants or white dwarfs. The PDMF therefore, needs to be corrected for stellar evolution. The stellar IMF and the PDMF are connected through the so called creation function which accounts for stellar evolution (Chabrier 2003).

Complete understanding of the SF process is critical to solving the IMF problem, not only for the local Solar neighbourhood, but on the universal scale. Since stars are born in cores, there is a general belief that the key to understanding the nature of the stellar IMF is, understanding the dense core mass function (DCMF).

Some problems in the star formation theory : A key problem in this area is that of establishing a connection between the stellar IMF and the DCMF. With technical advances, it has now become possible to map the dense prestellar cores in greater detail. Observations have now shown that the DCMF can be fitted by a two-piece power-law. This power-law however, is much steeper than the stellar IMF, in the high mass regime. The DCMF has a slope (α) 3.35 as against the stellar IMF, that has a Salpeter slope. See for instance Alves *et al* (2007), Clark *et al* (2007) and Nutter & Ward-Thompson (2007) amongst others. Simulations also tend to suggest a similar core mass function although with a slightly shallower slope,

$$dN(m) \propto m^{-1.5} dm \tag{1.4}$$

i.e. α= 2.5 (e.g. Klessen & Burkert 2000).

The power-law nature of the stellar IMF and the DCMF with similar shapes, has led workers to suggest a 1:1 map between the two distribution functions. However, such a conclusion has been debated for the following two reasons.

1. A collapsing protostellar core need not always produce a single star. Observations have unambiguously shown the existence of star clusters e.g. Pudritz (2002). Simulations too tend to support this claim (e.g. Goodwin *et al* 2008).

2. The timescale of collapse of a protostellar core varies. Denser cores will collapse on a shorter timescale than those, that are less dense. In

this eventuality, some cores are still collapsing in the current epoch, at the end of which, may produce a stellar IMF that may be different from the PDMF. To avoid the timescale problem we need to begin with the assumption that all prestellar cores have roughly the same density.

Correcting for the timescale problem, Clarke *et al* (2007) suggested the following two piece DCMF,

$$\begin{aligned} dN(m) &\propto m^{-0.35}dm; \quad 0.08 < m/\mathrm{M}_\odot < 0.5 \\ dN(m) &\propto m^{-1.35}dm; \quad m/\mathrm{M}_\odot > 0.5. \end{aligned} \tag{1.5}$$

This DCMF looks similar to the Salpeter IMF.

Apart from these two points, a related point is that of the turnover mass ($\sim$ 0.1 $\mathrm{M}_\odot$) in the stellar IMF. It is very close to the Jeans mass corresponding to $\sim$ 5 K and density $\sim 10^{-18}$ g cm^{-3} (Larson 2004). Thus, the conversion of the protostellar mass into stellar mass calls into question the role of other competing effects like the ambient magnetic field and stellar feedback on the star formation efficiency.

Modified stellar IMFs have been proposed to account for the stellar evolution and birth of new stars. This new IMF is still a power law and given as,

$$\xi(\log m) = Am^{-\alpha}. \tag{1.6}$$

A universal power-law i.e. an IMF for the field stars was suggested by Kroupa (2001). It is a four piece power-law and given as,

$$\begin{aligned} \alpha_0 &= +0.3 \pm 0.7; \quad 0.01 \leq m/\mathrm{M}_\odot \leq 0.08 \\ \alpha_1 &= +1.3 \pm 0.5; \quad 0.08 \leq m/\mathrm{M}_\odot \leq 0.5 \\ \alpha_2 &= +2.3 \pm 0.3; \quad 0.5 \leq m/\mathrm{M}_\odot \leq 1.0 \\ \alpha_3 &= +2.3 \pm 0.7; \quad 1.0 \leq m/\mathrm{M}_\odot. \end{aligned} \tag{1.7}$$

Corrections have been proposed to the slopes at the high mass end of the IMF (α_3) to account for inadequate binary statistics and the Malmquist bias (e.g. Massey 1998; Sagar & Richtler 1991). There is also a large uncertainty at the brown dwarf end of the stellar IMF (α_0) due to the completion limit of various surveys and the brown dwarf desert (supposedly caused due to

suppression of fragmentation of protostellar disks around sunlike stars Whitworth & Stametellos (2006)). See for instance Binney, Dehnen & Bertelli (2000) and Kroupa, Aarseth & Hurley (2001).

Plan of the thesis : In the present work, I intend to explore one possible mode of dynamical star formation, that of triggered star formation due to cloud-cloud collision. The arms of a galaxy have a number of Giant Molecular Clouds (GMCs) in orbit. Conservative statistical estimates suggest a cloud-cloud collision every few million years or in other words a single cloud may undergo a few collisions during a single rotation.

The problem of cloud collision is therefore significant. We intend to explore the evolution of the postshock composite gas body and the plausibility of it leading to star formation. We shall revisit the point when we present our results and discuss them in chapters 4 and 5.

The thesis has four chapters further. In chapter 2, I briefly discuss the properties of GMCs and present a simple model for them. In chapter 3, I discuss the smoothed particle hydrodynamics and present cloud collision models investigated in the present work. Additionally, two appendices have been included. In appendix A, a simple derivation of the general Lane-Emden equation has been presented. In appendix B, I discuss an allied short project on studying the association between filamentary star forming regions and jets emerging from YSOs located in those filaments.

Chapter 2

Equilibrium Clouds

In the present chapter, I discuss the properties, composition and various possible ways of classifying Giant Molecular Clouds (GMCs). I then propose a simple polytropic model for them, followed by a Virial analysis of non - rotating clouds, and I conclude with a very brief discussion of their mass spectrum.

2.1 Properties and structure of GMCs :

GMCs are primarily composed of molecular hydrogen, with a small percentage of atomic hydrogen confined mostly to the outer regions of the clouds. These regions are bathed in the interstellar radiation field. The intercloud medium (ICM) is a hot, diffuse ambient medium in galactic arms, and GMCs are cold agglomerations immersed in the ICM. The average density of this ambient medium is $\sim$0.1 cm^{-3}. The hottest regions of the ICM have temperatures as high as 10^4 K and may be classified as plasma. The ICM is mainly composed of singly/multiply ionised elements and highly energetic subatomic particles. The coldest regions, on the other hand, are dominated by molecules and dust.

The GMCs are local density enhancements, acted upon by finite external pressure from the diffuse ICM. The more dense regions within GMCs remain shielded from external radiation and therefore are cold with predominantly molecular composition. However, the outer regions are easily photodissociated and contain mostly atomic hydrogen. The extent of shielding is measured by a quantity called the shielding coefficient (Elmegreen, 1993). The

number density of atomic and molecular hydrogen can be determined by studying the absorption features of Lyman bands, higher the column density greater is the absorption. On this basis, GMCs may be classified as atomic or molecular clouds.

The extent to which external radiation can penetrate into the cloud depends on the shielding ability of the cloud. Most of the shielding occurs in an outer shell of HI. This region is called the Photo Dissociation Region (PDR). The extinction magnitude (A_V) in this region varies between five and ten, increasing in a direction pointing towards the centre of the cloud. The densest regions in the GMC have $A_V \sim 10$.

The number density in the PDR varies between 10^3 to 10^6 cm^{-3}, with temperature as high as $\sim$ 100K. H, O and C^+ are the dominant species and $A_V < 2$. In the deeper regions of the PDR i.e. in the regions with $A_V \sim 5$, the temperature drops to $\sim$ 20 K and the gas consists of H, O and CO. The innermost regions of the GMCs are colder at <10 K, and here molecular species start dominating. The external radiation heats up the gas in regions having $A_V \sim 5$, and emits through CO emission.

Cosmic rays penetrate deeper into the cloud. This leads to CI emission at 370 μm and CO emission at 609 μm. The PDR also radiates in the IR at 3.3, 6.2, 7.3 and 11.3 μm due to IR fluorescence of polyaromatic hydrocarbons (PAHs). These are small aromatic carbon compounds having 20 to 50 carbon atom chains, that are vibrationally excited due to the incident FUV radiation. The first ionisation potential for a 20 carbon atom PAH is $\sim$7 eV while the second one is above that of atomic hydrogen (Hollenbach *et al*, 1991). The dust grains in the PDR are at temperatures between $\sim$ 10 and 30 K.

For equilibrium to be maintained in this transition region, it is necessary that the rate of recombination and photodissociation of atomic hydrogen be approximately the same. This in turn depends on the average intensity of incident radiation. Once the recombination rate is known then with the help of general requirements of equilibrium, the shielding function can be defined. The details of these calculations can be found in Elmegreen (1993).

Using the shielding function we can approximate the density distribution within a GMC. On this basis, GMCs can be very broadly classified as diffuse/gravitationally bound molecular clouds. In diffuse clouds gravity is not important and further, if the internal velocity dispersion is low (compared to local sound speed), we may assume that such clouds have constant internal

number density n that depends on the external pressure (P_{ext})

$$n = \frac{P_{ext}}{k_B T},$$

where k_B is the Boltzmann constant and T is the approximately uniform temperature within the GMC. On the other hand in gravitationally bound clouds, the density varies as $n(r) \sim n_B\left(\frac{r_B}{r}\right)^2$, which is approximately the isothermal density profile (n_B is the number density at the cloud edge). Here r_B is the cloud radius and r is the outward radial distance from the centre of the cloud. The average number density in such clouds is $< n > \sim 3n_B$, which in turn is related to external pressure by the Virial theorem.

GMCs can also be classified on the basis of number density. The critical number density above which a cloud can collapse under self gravity is

$$< n >_{crit} = 10^3 \frac{T^3}{\left(\frac{M}{M_\odot}\right)^2},$$

while those with $< n >$ less than $< n >_{crit}$ are not prone to gravitational collapse (Roberts, 1969). On this basis larger clouds are estimated to have masses $\sim 10^4$ $M_\odot$ and radii $\sim$20 pc with $< n > \sim$20 cm^{-3}, although extremely massive GMCs have also been reported in the Milky Way with mass $\sim 10^6 M_\odot$ in the southern Carina arm (Solomon *et al*, 1987). Depending on the predominance of atomic or molecular hydrogen, the GMCs can also be classified into four types viz. diffuse atomic, diffuse molecular, self gravitating molecular and non - self gravitating molecular clouds (Elmegreen, 1993).

GMCs also occur in clusters called Molecular Cloud Clusters (MCCs). These clusters have masses well in excess of $10^6 M_\odot$ and a survey within the Milky Way has shown that most of these complexes are concentrated in an annular region between four to eight parsecs from the galactic centre. Usually MCCs are in Virial equilibrium and typically have velocity dispersions of order a few kms^{-1} to a few tens of kms^{-1}.

Observations suggest that the ratio of H_2 column density to the intensity of CO emission is $\sim 6 \times 10^{20}$ molecules cm^{-2} K^{-1} (km s^{-1})$^{-1}$ (Sodroski, 1991). GMCs have been mapped in mm and submm wavelengths due to line emission from ^{13}CO, C^{18}O, NH_3 and CS. In particular CO is a good tracer of molecular hydrogen because they appear to be coextensive. Also CO is readily excited due to its lower excitation energy, and it is relatively abundant. The warmer regions like the PDRs can be studied from spectral lines

of ionised heavier elements like oxygen, silicon, carbon etc. These studies have revealed that the distribution of matter within GMCs is highly non uniform. There are several highly dense regions called globules or clumps with densities of order 10^5 cm^{-3}.

These clumps are in constant random motion, referred to as internal turbulent motion of GMCs. Lubow & Pringle (1996) did a numerical study of the internal dynamics of a typical GMC and proposed a stochastic mechanism of interaction between large amplitude Alfvèn waves and the gas within GMCs, to explain clump formation. According to this mechanism, clumps are formed in regions where the waves interfere constructively leading to enhanced amplitude. A similar idea was also proposed by Bash *et al* (1981). The former authors assumed a simple cloud model having mass $\sim 10^5 M_\odot$ and radius 20 pc. Dynamical equilibrium of the cloud then demands a mean velocity dispersion of $\sim$3.4 kms^{-1}.

Surveys of GMCs like NGC 2071, NGC 2068, NGC 2024 and L 1630 in the past, have revealed that the mass of the dense regions is only about eight percent of the total cloud mass. Often there is a hierarchy of smaller, denser clumps being embedded in larger, more diffuse clumps. Observations suggest that clumps are usually gravitationally unbounded (Carr, 1987; Lada, 2008). In highly turbulent environments there is a constant recycling of material, with clumps forming and dispersing on a time scale of $\sim 10^6$ years.

There have been numerous efforts in the past to study various physical properties of these clumps. A related study by Larson (1979) revealed that clump velocities follow a Kolmogorov like power law dispersion relation. Later, a much larger survey spanning eleven cloud complexes including Orion, ρ Ophichus and Taurus among others, was used to determine this dispersion relation. Once again a simple power law relation was found connecting the velocity dispersion (σ) of the clumps with the linear dimension (L)

$$\sigma(\mathrm{km/s}) = 1.10 L^{0.38}(\mathrm{pc}) \tag{2.1}$$

(Larson, 1981). The RMS deviation of $\log\sigma$ is about 0.14 i.e approximately 1.38 in σ. This equation holds for $0.1 \leq L \leq 100$ pc and bears close resemblance with the subsonic turbulence relation (Kolmogorov Law), $\sigma \propto L^{\frac{1}{3}}$. The velocity dispersion in GMCs is supersonic. The corresponding power law dispersion relations for clump masses and densities are

$$\sigma(\mathrm{km/s}) = 0.42 M^{0.20}(\mathrm{M}_\odot) \tag{2.2}$$

$$< n(\mathrm{H_2}) > (\mathrm{cm}^{-3}) = 3400 L^{-1.10}(\mathrm{pc}), \tag{2.3}$$

where M is the clump mass.

Apart from internal turbulence, GMCs are also threaded by magnetic fields whose magnitude varies approximately as the square root of density. The strength of magnetic field can be determined by studying the Zeeman splitting of spectral lines and by looking at the polarisation properties of dust grains. The magnetic field strength varies from a few μG to a few tens of μG. For instance in Orion A, the magnetic field measured along the line of sight is $\sim$ 125 μG, while in Orion B it is $\sim$ 38 μG. The supersonic turbulence within GMCs is inefficient in providing buoyancy against gravitational collapse. Interclump collisions within GMCs leads to energy dissipation through internal shocks.

The GMCs are therefore expected to contract on a dynamic time scale, see Equations (2.51) & (2.52). But the actual life time of GMCs is greater than the dynamic time scale by almost an order of magnitude. The magnetic field is crucial in providing additional support to the cloud against self gravity and inhibits gravitational collapse. We shall see this further in the Virial analysis of a GMC. On the other hand ambipolar diffusion assists gravitational collapse of clouds and in fact, may even trigger it. To measure the dominance of the magnetic field in supporting clouds, we define a critical magnetic mass as,

$$M_{cr} = 0.13\frac{\Phi}{G^{\frac{1}{2}}} \sim 10^3 \mathrm{M}_\odot \Big(\frac{B}{30\mu\mathrm{G}}\Big) \cdot \Big(\frac{R}{2\mathrm{pc}}\Big)^2$$

(Shu *et al*, 1987).

Clouds having masses (M_{cld}) smaller than M_{cr} are magnetically subcritical while those having masses greater than M_{cr} are magnetically supercritical. The criticality implied here, is in the sense that the magnetic field is dominant over other forms of support against self gravity. For clouds in virial equilibrium, the kinetic energy and the gravitational potential energy must be balanced. The kinetic energy due to velocity dispersion σ is $\frac{1}{2}M\sigma^2$ and the gravitational potential energy is $\sim \frac{-2GM^2}{L}$. The Virial theorem then demands that

$$\sigma^2 \sim \frac{2GM}{L}. \tag{2.4}$$

The quantity $Q = \left(\frac{2GM}{\sigma^2 L}\right)$ is called the Virial ratio. Q obeys the following power law

$$Q = 0.92 L^{0.14}(\mathrm{pc}) \tag{2.5}$$

(Larson, 1981). A plot of $\log Q$ against $\log L$ is a straight line with slope 0.14, suggesting that the GMCs in the particular sample were gravitationally bound. The column density is given by $< n(H_2) > \cdot L$ and in view of Equation (2.3) above, it follows that the column density varies as $L^{-0.1}$, which suggests that it is more or less independent of size. GMCs have high column densities and this fact may lend credence to the theory that they are formed in galactic shocks. However, it could also be a result of the fact that this conclusion was based on data obtained from ^{13}CO line emission only and may therefore suffer from selection effects.

The clumpy structure within GMCs has led some people to perform fractal analysis of clouds. Such studies have shown that the boundaries of GMCs have a projected fractal dimension of $\sim$1.3. A simple method of estimating fractal dimension is the Box - Counting method, where the region under investigation is fitted with a large number of boxes, say N, each of size δ, so that the structure being analysed is completely spanned by boxes. The fractal dimension D is given by

$$D = \lim_{\delta \to 0} \left(\frac{\log N}{-\log \delta} \right) \tag{2.6}$$

(Falconer, 1997). Further, the distribution of cloud sizes (S) and masses (M_{cld}) are found to be

$$n(S)dS \sim S^{(1+D)}dS \tag{2.7}$$

$$n(M_{cld})dM_{cld} \sim M_{cld}^{\frac{-1-\kappa}{D}} dM_{cld}. \tag{2.8}$$

respectively. Here $D \sim 2.3$ and $\kappa \sim 3$. It has been found that clouds having masses in the range 10^2 to 10^7 $M_\odot$ obey these values quite well (Elmegreen & Flagrone, 1996; Elmegreen, 1997). I will discuss the cloud mass spectrum briefly towards the end in §2.2.3.

Another quantity which gives a measure of the density distribution within a non - uniform medium is the volume filling factor, f_V. The filling fraction for the low density ICM is

$$f_{hole} = 1 - f_V = 1 - C^{\frac{D}{3}-1} \sim 80\%, \tag{2.9}$$

where C is the density contrast between the regions separated. The above value of f_{hole} has been calculated for $C = 10^3$, by assuming that the density of the diffuse medium is 0.1 cm^{-3} to 100 cm^{-3} while that in the clouds is 10^2 cm^{-3} to 10^5 cm^{-3}. Thus, a rather large value of f_V suggests that most of the interstellar medium is rarefied.

Since clouds are clumpy, there are some regions (the holes between clumps) which produce no absorption lines, while there are other regions (the clumps) which produce strong absorption features. These are compact, clustered regions. Using fractal models, it has been shown that on average there are about three clumps along the line of sight with an average mean free path of about 330 pc (Elmegreen, 1999).

2.1.1 Formation of GMCs :

Having reviewed the properties of the GMCs let us now look at the possible process by which they are formed. Galactic shocks influence the dynamics on small (up to 10 pc) and large scales (a few kpc). Large scale shocks are called galactic shocks. Density waves thread the arms of a spiral galaxy and theoretical predictions suggest that the amplitude of these waves grows and leads to the formation of periodically located shocks. The gravitational potential of spiral galaxies has four components that corresponds to the central bulge, the galactic disk, the spiral arms and the unseen halo (Binney & Tremaine, 1994).

The generation of spiral waves is the result of perturbation from the spiral component to the overall potential. The dynamics of gas passing through this type of gravitational potential yields a set of equations whose solution requires that the gas pass through two periodically located shocks, coincident with the spiral equipotential curves in the disk. This forms a streamtube which must repeat itself after every half rotation of gas in the disk. Additionally, the streamtubes themselves must satisfy the condition that there is no transfer of mass, momentum or energy across them. This solution is called the Streamtube Shock (STS) wave solution (Roberts, 1969). Gas passing through these streamtubes experiences sudden shocks, causing them to compress eight to ten times their original density. As a result the entire medium gets segregated into two phases; a warm diffuse phase (ICM) with a temperature $\sim 10^4$ K and the cold dense phase (clouds) at $\sim$10 K to 200 K (Shu *et al*, 1972).

Using this two phase model the maximum and minimum pressure that leads to cloud formation, can be calculated. Since the ICM is a rarefied medium, the atoms are collisionally excited/ionised, while the de - excitation takes place radiatively. For an equilibrium between the two media, these two processes must balance each other. Accounting for the total heat gain, radiative losses, rate of ionisation and recombination, the maximum and

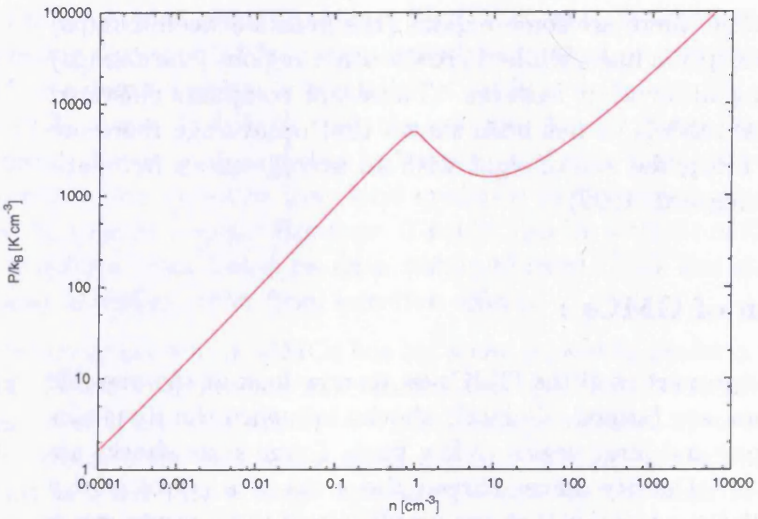

Figure 2.1: Plot of equilibrium temperature against the number density. At $n \sim 1$ cm^{-3} the plot ceases to be linear, while for $n \gtrsim 10$ cm^{-3} the equilibrium temperature once again rises monotonically. The transition phase between densities 1 cm^{-3} to 10 cm^{-3} is thermally unstable.

minimum pressure within which this equilibrium can be maintained is,

$$\log\left(\frac{P_{max}}{k_B}\right) = 3.18.$$

and

$$\log\left(\frac{P_{min}}{k_B}\right) = 2.48.$$

The average pressure of the combined medium is $P = (n + n_e)k_BT$; where n is the number density of atoms and n_e is that of free electrons.

If $P_{min} \leq P \leq P_{max}$ then the two phases can remain in equilibrium with each other. An intermediate phase would be unstable. Thus, if a blob of gas is suspended in the ICM, it will evolve into one of the two phases. If the pressure in the medium increases above P_{max}, some of the intercloud material will condense into cloud material while if the pressure in the medium is reduced below P_{min}, some of the cloud material will evaporate to form the inter cloud material. The process is governed by thermal instabilities and an imbalance in one of the two phases leads to a run - away process (Shu *et al*, 1972). This can be seen from the plot of thermal pressure against H_2 column

density shown in Figure (2.1) above. The maxima and minima in this curve correspond to P_{max} and P_{min} respectively. In order to study the evolution and dynamics of GMCs theoretically and simulate them numerically, it is necessary to model them correctly.

A powerful tool for modelling them is that of *polytropes*. These have also been successfully employed to model stellar structures. Fundamentally they are solutions to the Lane - Emden equation. Here GMCs are simply modelled as isothermal spheres confined by finite external pressure, called Bonnor - Ebert (BE) spheres. Below, I review some of their physical parameters.

2.2 The Bonnor-Ebert sphere :

An isothermal gas has a uniform sound speed (say a_0). If $P(r)$ and $\rho(r)$ are the pressure and density respectively, as function of the radial coordinate then

$$P(r) = a_0^2 \rho(r). \tag{2.10}$$

The square of the sound speed a_0 is defined as

$$a_0^2 = \frac{k_B T}{\bar{m}}, \tag{2.11}$$

where T is the temperature of the gas and $\bar{m}$ is the average mass of a single gas particle.

If ρ_c is the central density of the sphere then,

$$\rho(r) = \rho_c e^{-\frac{\phi}{a_0^2}}. \tag{2.12}$$

$\phi(r)$ is the gravitational potential per unit mass. Since it is convenient to work in dimensionless variables, we introduce a length scaling factor, R_0. It is defined as,

$$R_0^2 = \frac{a_0^2}{4\pi G \rho_c}. \tag{2.13}$$

We also introduce a function $\psi(\xi)$ such that, $\phi = a_0^2 \psi$. The general Lane-Emden equation has been derived in Appendix A (see Equation (A.10)). Here we simply quote the equation for the isothermal case ($\gamma = 1, n = \infty$),

$$\Rightarrow \frac{d}{d\xi}\left(\xi^2 \frac{d\psi}{d\xi}\right) = \xi^2 e^{-\psi}. \tag{2.14}$$

Let

$$\mu = \xi^2 \frac{d\psi}{d\xi}, \tag{2.15}$$

so that Equation (2.14) becomes

$$\frac{d\mu}{d\xi} = \xi^2 e^{-\psi}. \tag{2.16}$$

The potential is so chosen that $\phi(0) = 0$. The other boundary conditions are $\psi(0) = 0$ and $\frac{d\psi}{d\xi}\Big|_{\xi=0} = 0$. Note that equation (2.16) cannot be integrated exactly, hence we resort to the series solution method. Let us assume the solution to be of the form

$$\psi(\xi) = a\xi^2 + b\xi^4 + c\xi^6 + ... \tag{2.17}$$

Evaluating the required derivatives, substituting them back in Equation (2.14) and then expanding the exponential term in its power series, before finally comparing coefficients on both sides of the equation, yields

$$\psi(\xi) = \frac{1}{6}\xi^2 - \frac{1}{120}\xi^4 + \frac{1}{1890}\xi^6 - ... \tag{2.18}$$

This is the asymptotic series solution applicable only near the origin. Figure (2.2) shows the function $\psi(\xi)$, while Figure (2.3) shows the plot of $\frac{d\psi(\xi)}{d\xi}$. The isothermal sphere has infinite radius as $\xi \to \infty$. However, we are interested to have an isothermal sphere with finite radius, say ξ_B, called the BE sphere (Bonnor, 1956).

Let us now look at the fundamental state variables, viz. the pressure and density of the Bonnor - Ebert sphere. We first obtain an expression for the mass interior to a shell and the density $\rho(r)$. If r is the radial coordinate from the centre of the sphere outward, then the mass interior to r is

$$M(r) = \int_{r'=0}^{r'=\xi} \rho(r') \cdot 4\pi r'^2 dr'.$$

Now using equation (2.13) and that $r' = R_0\xi'$, the above equation becomes

$$M(r) = 4\pi\rho_c \Big(\frac{a_0^2}{4\pi G\rho_c}\Big)^{\frac{3}{2}} \int_{\xi'=0}^{\xi'=\xi} e^{-\psi}\xi'^2 d\xi', \tag{2.19}$$

where we have used equation (2.13) to substitute for R_0

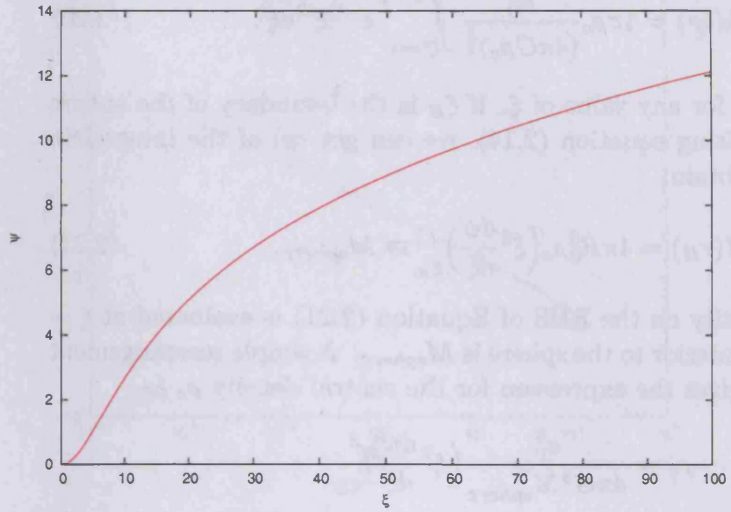

Figure 2.2: Plot of $\psi(\xi)$.

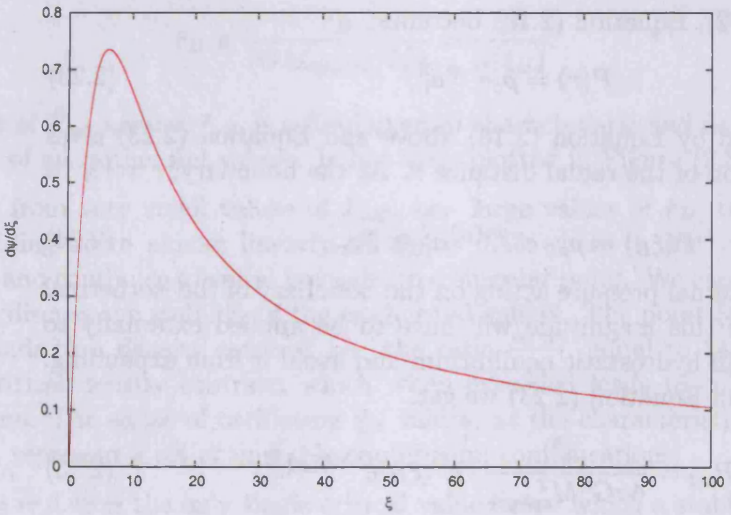

Figure 2.3: Plot of $\frac{d\psi(\xi)}{d\xi}$.

$$\Rightarrow M(r) = 4\pi\rho_c \frac{a_0^3}{(4\pi G\rho_c)^{\frac{3}{2}}} \int_{\xi'=0}^{\xi'=\xi} e^{-\psi} \xi'^2 d\xi'. \tag{2.20}$$

This equation holds for any value of ξ. If ξ_B is the boundary of the sphere then $r_B = \xi_B R_0$. Using equation (2.14), we can get rid of the integral in equation (2.20) to obtain,

$$M(r_B) = 4\pi R_0^3 \rho_c \Big(\xi^2 \frac{d\psi}{d\xi}\Big)_{\xi_B} \equiv M_{sphere}. \tag{2.21}$$

The bracketed quantity on the RHS of Equation (2.21) is evaluated at $\xi = \xi_B$. The total mass interior to the sphere is M_{sphere}. A simple rearrangement of Equation (2.21) gives the expression for the central density ρ_c as,

$$\rho_c = \frac{a_0^6}{4\pi G^3 M_{sphere}^2} \Big(\xi^2 \frac{d\psi}{d\xi}\Big)_{\xi_B}^2$$

$$\Rightarrow \rho(r) = \frac{a_0^6}{4\pi G^3 M_{sphere}^2} \Big(\xi^2 \frac{d\psi}{d\xi}\Big)_{\xi_B}^2 \cdot e^{-\psi(\xi)}. \tag{2.22}$$

This is the expression for density within the Bonnor - Ebert sphere as a function of the radial coordinate.

Using Equation (2.12), Equation (2.10) becomes,

$$P(r) = \rho_c e^{-\psi} a_0^2, \tag{2.23}$$

with $\psi(\xi)$ as defined by Equation (2.18) above and Equation (2.23) gives pressure as a function of the radial distance r. At the boundary; $r = r_B$ i.e $\xi = \xi_B$,

$$P(\xi_B) = \rho_c \cdot e^{-\psi(\xi_B)} a_0^2 \equiv P_{ext}. \tag{2.24}$$

This is the finite external pressure acting on the boundary of the isothermal sphere. Pressure of this magnitude will have to be applied externally to maintain the cloud in hydrostatic equilibrium and avoid it from expanding. Substituting for ρ_c in Equation (2.23) we get,

$$P_{ext} = \frac{a_0^8}{4\pi G^3 M_{sphere}^2} \cdot \mu^2(\xi_B) e^{-\psi(\xi_B)}. \tag{2.25}$$

We can recast this equation in dimensionless form as

$$\hat{P}_{ext} \equiv \frac{P_{ext}}{(a_0^8/4\pi G^3 M_{sphere}^2)} = \mu^2(\xi_B) e^{-\psi(\xi_B)}. \tag{2.26}$$

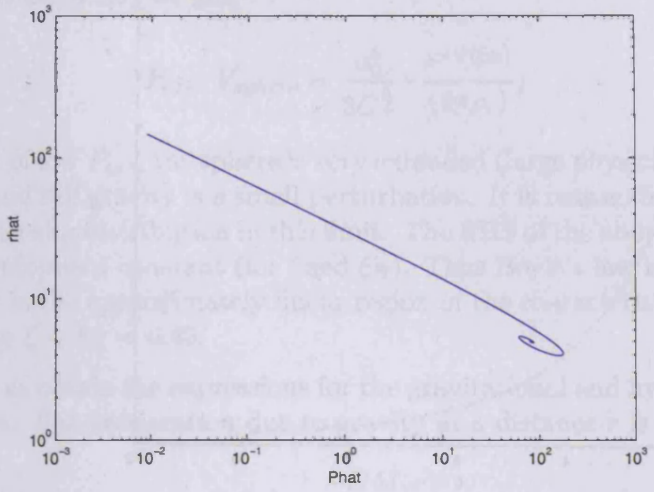

Figure 2.4: Plot of $\hat{P}_{ext}$ Vs $\hat{r_B}$.

Also, the boundary radius $r_B = R_0\xi_B$. We can define the dimensionless radius $\hat{r}_B$ as

$$\hat{r}_B \equiv \frac{r_B}{(GM_{sphere}/a_0^2)} = \frac{\xi_B}{\mu(\xi_B)}. \tag{2.27}$$

The plot of $\hat{P}_{ext}$ against $\hat{r}_{ext}$ is a fundamental characteristic and defines the stability of an isothermal sphere. It has been plotted in Figure (2.3).

Starting from very small values of $\hat{P}_{ext}$, i.e. large values of $\hat{r}_B$, the curve keeps sliding down almost linearly till $\xi_B = 6.45$ where it first twists in, reverses and continues to spiral inwards, to a singular point. We can use this curve to discuss the stability of the isothermal sphere. The point $\xi_B = 6.45$ corresponds to a density contrast i.e. the ratio $\frac{\rho(r_B)}{\rho_c}$, equal to 14.1. This is the critical density contrast, which when exceeded leads to collapse of the sphere. The series of oscillating ξ_B values, as the characteristic spirals inwards, represent a set of unstable equilibrium configurations.

Thus, $\xi_B = 6.45$ is the only single critical value below which a stable equilibrating structure is possible. This stable region corresponds to the roughly linear portion of the curve in Figure (2.4). In this region, any increase in the external pressure leads to a decrease in the sphere radius. The cloud remains gravitationally stable till P_{ext} becomes so large that $\frac{\rho(r)}{\rho_c} > 14.1$. The mass

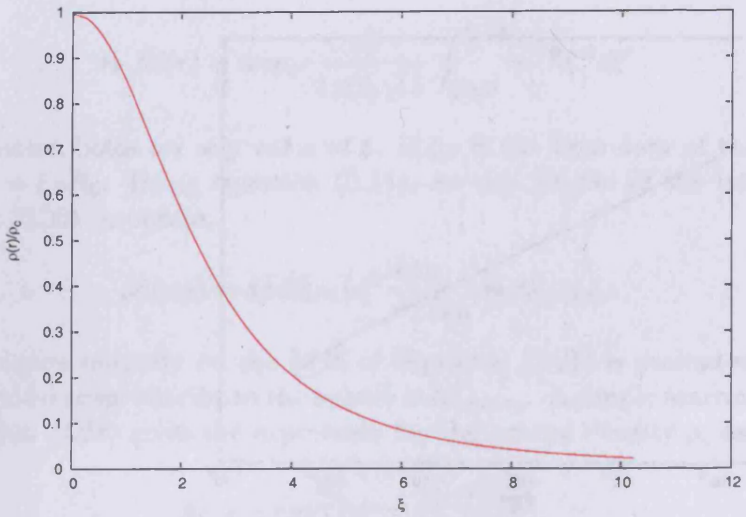

Figure 2.5: Plot of $\frac{\rho(r)}{\rho_c}$ Vs ξ.

within the sphere of critical radius (ξ_B=6.45) is called the Bonnor - Ebert mass (M_{BE}). By plugging in this critical value of ξ_B and the corresponding value of $(\frac{d\psi}{d\xi})_{\xi_B}$ from the Emden table, in Equation (2.21) we get

$$M_{BE} = 8.8\frac{a_0^3}{G^{3/2}\rho^{1/2}}. \tag{2.28}$$

The same result can be obtained in a more rigorous manner starting from first principles, see Bonnor (1956).

A stable equilibrium state implies that a small perturbation to the equilibrium configuration will produce oscillations about the stable state and then slowly return to the initial state of equilibrium. There is no cataclysmic collapse. The maximum external pressure corresponds to a density contrast of 14.1. This can be seen from Figure (2.5), which is a plot of density contrast against radial distance. Note that $\rho(r)$ drops to $(14.1)^{-1} \sim 0.071$ of its value at the centre, at $\xi_b = 6.45$. It would be interesting exercise to look at the product of P_{ext} and the volume of the sphere (V_{sphere}) i.e

$$P_{ext} \cdot V_{sphere} = P_{ext}\frac{4}{3}\pi r_B^3$$

$$= \frac{a_0^8}{4\pi G^3 M_{sphere}^2} \cdot \mu^2(\xi_B)e^{-\psi(\xi_B)}\frac{4\pi}{3}\xi_B^3\frac{a_0^3}{(4\pi G\rho_c)^{\frac{3}{2}}}.$$

Using Equation (2.25) we get,

$$P_{ext} \cdot V_{sphere} = \frac{a_0^5}{3G^{\frac{3}{2}}} \cdot \frac{e^{-\psi(\xi_B)}}{(4\pi\rho_c)},$$

In the limit of low P_{ext}, the sphere is very extended (large physical radius but small ξ_B) and self gravity is a small perturbation. It is reasonable to assume a uniform density distribution in this limit. The RHS of the above expression therefore becomes a constant (for fixed ξ_B). Thus Boyle's law is verified, as is expected in the approximately linear region of the characteristic in Figure (2.3) i.e. for $\xi < \xi_B = 6.45$.

Finally, let us obtain the expressions for the gravitational and hydrodynamic acceleration. The acceleration due to gravity at a distance r is given by

$$a_g(r) = \frac{-GM(r)}{r^2},$$

using Equation (2.21) and $r = R_0\xi$, the above equation becomes

$$a_g(r) = \frac{-a_0^4}{GM_{sphere}} \left(\xi^2 \frac{d\mu}{d\xi}\right)_{\xi_B} \cdot \left(\frac{d\psi}{d\xi}\right)_{\xi=\frac{r}{R_0}}. \tag{2.29}$$

On the other hand, for a spherically symmetric system the hydrodynamic acceleration at a distance r due to pressure $P(r)$ is

$$a_p(r) = \frac{1}{\rho(r)} \cdot \frac{dP(r)}{dr},$$

using Equations(2.22) and (2.24) we get,

$$a_p(r) = \frac{a_0^4}{GM_{sphere}} \left(\frac{\xi^2 d\mu}{d\xi}\right)_{\xi_B} \cdot \left(\frac{d\psi}{d\xi}\right)_{\xi=\frac{r}{R_0}}. \tag{2.30}$$

Observe that $a_p(r)$ and $a_g(r)$ are equal in magnitude but opposite in direction, as is necessary for an equilibrium configuration.

Numerical analysis of the stability of the isothermal sphere and its collapse has been studied in detail by Larson (1969), Penston (1969) and Shu (1977) among others. Shu's self similar collapse solutions show the occurrence of a reflection shock at the boundary of the isothermal sphere, which propagates inwards and further enhances gravitational collapse. As the central core gets denser its temperature starts rising. The resulting thermal support inhibits

further collapse of outer shells. The time required for complete collapse of the isothermal sphere to a singular point is effectively infinity.

This picture however, assumes static boundaries which is incorrect. The collapse therefore no longer remains homologous. A strong rarefaction shock wave, reflected by the static boundary propagates into the collapsing cloud which accelerates the cloud collapse. Such a collapse simply piles up the material at the centre and the central density becomes enormously high. Disney (1976) for instance, suggested comoving a boundary of a collapsing cloud to alleviate the discrepancy in the former analysis. We shall however, not into any further details of the matter here.

2.2.1 Virial analysis of GMCs :

GMCs appear to be gravitationally bound. It has been noted in the previous section that supersonic turbulence within GMCs alone cannot support them against self gravity. The role played by various forces in providing support against self gravity will now be investigated using Virial analysis.

If $\Phi_g(r)$ is the gravitational potential, the corresponding force per unit mass is $\nabla\Phi_g$. The equation of hydrostatic equilibrium is therefore,

$$-\frac{1}{\rho}\nabla P - \nabla\Phi_g = 0. \tag{2.31}$$

We assume that the fluid under consideration is inviscid. The general equation of motion of the fluid must also contain the ambient magnetic field. Thus,

$$\rho\frac{D\mathbf{u}}{Dt} = -\nabla P - \rho\nabla\Phi_g + \frac{1}{c}\mathbf{j}\times\mathbf{B}, \tag{2.32}$$

where $\frac{D\mathbf{u}}{Dt}$ is the total time derivative of the velocity $\mathbf{u}$ of a fluid element and defined as

$$\frac{D\mathbf{u}}{Dt} = \left(\frac{\partial\mathbf{u}}{\partial t}\right)_x + (\mathbf{u}\cdot\nabla)\mathbf{u}. \tag{2.33}$$

The third term on the right hand side of Equation (2.32) is the magnetic force per unit volume acting on a current density $\mathbf{j}$. The magnetic field $\mathbf{B}$ and the current density $\mathbf{j}$ are related by Ampere's law

$$\nabla\times\mathbf{B} = \frac{4\pi}{c}\mathbf{j}. \tag{2.34}$$

The displacement current, $\frac{1}{c}\left(\frac{\partial\mathbf{E}}{\partial t}\right)$, has been neglected ($\mathbf{E}$ being the electric field) since there is negligible change in electric field on the relevant

timescales. Using Equation (2.34), Equation (2.32) becomes

$$\rho\frac{D\mathbf{u}}{Dt} = -\nabla P - \rho\nabla\Phi_g + \frac{1}{4\pi}(\mathbf{B}\cdot\nabla)\mathbf{B} - \frac{1}{8\pi}\nabla|\mathbf{B}|^2. \tag{2.35}$$

The last term on the right hand side of Equation (2.35) represents the magnetic tension due to twisting of magnetic field lines (magnetic shear). By taking the scalar product of Equation (2.35) with the position vector $\mathbf{r}$ and integrating it over volume, we get the expression for Virial equilibrium given by equation (2.36) below; the reader is referred to Stahler & Palla (2004) for details of this derivation,

$$\frac{1}{2}\frac{\partial^2\mathcal{I}}{\partial t^2} = 2\mathcal{T} + 2\mathcal{U} + \mathcal{W} + \mathcal{M} - \int\left(P + \frac{B^2}{8\pi}\right)\mathbf{r}\cdot\hat{n}d^2\mathbf{x} + \frac{1}{4\pi}\int(\mathbf{r}\cdot\mathbf{B})\mathbf{B}\cdot\hat{n}d^2\mathbf{x}. \tag{2.36}$$

Various terms in the Virial expression given by Equation (2.36) are as follows: On the left hand side,

$$\mathcal{I} = \int \rho x_j x_j d^3\mathbf{x}, \tag{2.37}$$

is the moment of inertia.

$\mathcal{T}$ is the total kinetic energy and defined as,

$$\mathcal{T} = \frac{1}{2}\int \rho|\mathbf{u}|^2 d^3\mathbf{x}. \tag{2.38}$$

For a non-relativistic fluid the internal pressure is $\frac{2}{3}\mathcal{U}$, where $\mathcal{U}$ is the thermal energy density and defined as,

$$\mathcal{U} = \frac{3}{2}\int nk_B T d^3\mathbf{x}$$

$$= \frac{3}{2}\int P d^3\mathbf{x}.$$

Next, the gravitational potential $\Phi_g(\mathbf{r})$ is given as

$$\Phi_g(\mathbf{r}) = -G\int\frac{\rho(\mathbf{r}')}{|\mathbf{r}-\mathbf{r}'|}d^3\mathbf{x}.$$

The gravitational potential energy $\mathcal{W}$ is defined as,

$$\mathcal{W} = \frac{1}{2}\int \rho(\mathbf{r}) \cdot \phi(\mathbf{r})(\mathbf{r}) d^3\mathbf{x} \tag{2.39}$$

Finally, the magnetic energy is defined as,

$$\mathcal{M} = \frac{1}{8\pi}\int |\mathbf{B}|^2 d^3\mathbf{x}, \tag{2.40}$$

Now, if P_e, ρ_e and a_e are the pressure, density and sound speed, respectively at the cloud edge, ρ_e is related to the mean internal density according to the relation

$$\rho_e = A < \rho > \tag{2.41}$$

$$P_e = \rho_e a_e^2 = A < \rho > a_e^2 = \frac{3AMa_e^2}{4\pi R^3}. \tag{2.42}$$

For a cloud in Virial equilibrium, all the Virial components in Equation (2.36) should balance each other. The relative importance of magnetic field and thermal pressure is represented by the fifth term in this equation and we may define a parameter τ as

$$\tau = \frac{B^2}{8\pi P}, \tag{2.43}$$

which is the ratio of magnetic to thermal pressure. When $\tau \longrightarrow 0$, the role of magnetic field is insignificant and becomes important as $\tau \longrightarrow 1$.

A comparison of thermal pressure with the magnetic pressure suggests that the magnetic field, $B \propto \rho^{\frac{\gamma}{2}}$ ($\gamma = 1$). Magnetic fields play an important role in providing support against self gravity. However, gravitational collapse may be induced by a trigger, either external or internal. It is believed that the collapsing material follows magnetic field lines (in case of strong magnetic fields) (e.g. Alves, Franco & Girart, 2008), following which the cloud forms an hour glass structure. In non magnetic case, simple dimensional analysis suggests that the stability of a GMC depends on a parameter λ, defined as the ratio of the thermal pressure at the edge and pressure due to self gravity,

$$\lambda = \frac{P_{ext}R^4}{GM^2}. \tag{2.44}$$

2.2.2 The cloud mass spectrum :

Before concluding this chapter, I would like to briefly discuss the GMC mass spectrum. As with the stellar mass function seen previously, the convention is to fit the distribution of GMC masses with a power - law. Observations suggest that the number of clouds in the mass range M_{cld} and $M_{cld} + dM_{cld}$ is

$$n(M_{cld})dM_{cld} \propto M_{cld}^{\gamma} dM_{cld}, \tag{2.45}$$

where γ ranges between -1.5 to -2 (e.g. Solomon *et al*, 1987; Dickey & Garwood, 1989; Stutzki *et al*, 1998). By fitting power - law scaling relations to the ISM components like the density (volume and column), turbulent velocity etc., it is possible to arrive at a power - law similar to the one quoted in equation (2.45) above (Fleck, 1996).

In general, equation (2.45) can be rewritten as,

$$\frac{dn(M_{cld})}{dM_{cld}} = f(M_{cld}). \tag{2.46}$$

The cumulative mass distribution can then be obtained by integrating equation (2.46) as,

$$N(M' > M_{cld}) = \int_{M_{cld}=M_{max}}^{M_{cld}=M'} f(M_{cld})dM_{cld}. \tag{2.47}$$

This equation gives the number of clouds having masses greater than a reference mass, M_{cld}, as a function of the reference mass. The cloud mass spectrum as given by equation (2.45) above, is based on CO surveys, and therefore may suffer from selection effects and incompleteness due to the minimum flux detection criteria. Surveys in the past for the Milky Way, for instance, suggest a turnover mass (towards lower cloud masses) of $\sim 5{\times}10^4$ $M_{\odot}$ (Solomon *et al*, 1987).

To account for this feature, truncated power - laws have been suggested. Using equation (2.45) in equation (2.47) we get

$$N(M' > M_{cld}) = N_0\Big[\Big(\frac{M_{cld}}{M_{max}}\Big)^{\gamma+1} - 1\Big], \tag{2.48}$$

where N_0 is the number of clouds at the high mass end and M_{max} is the maximum mass upto which the power - law fit is valid, in other words it is the turnover mass, to which we referred above. For $N_0 = 1$, there is no deviation from the power - law (Williams & McKee, 1997; Rosolowsky,

2005). For the Milky Way, $N_0 = 105$ and the maximum mass, M_{max}, is 6×10^6 $M_\odot$. In case of shallower power - laws with $\gamma > -2$, most of the cloud mass is contained at the high mass end and vice - versa for steeper power laws ($\gamma < -2$).

In the following chapter, I will briefly look at the numerical scheme employed by us for our cloud collision simulations.

Chapter 3

Smoothed Particle Hydrodynamics

In this chapter I will review some basic aspects of Smoothed Particle Hydrodynamics (SPH). Additional mathematical details related to the SPH interpolant and the choice of the interpolating kernel are worth discussing, but have been omitted in the interests of brevity. The interested reader, instead is referred to Parzen (1960) and Parzen (1962). Below, I first describe the SPH density calculation, followed by a brief discussion of the calculation of (non periodic) gravity and its softening, and the form of numerical viscosity used in SPH. Finally, I shall discuss the time stepping and the integration scheme used to integrate the equations of motion.

In fluid dynamics, the equations governing the fluid flow are non linear, and therefore hard to solve. It may not always be possible to solve hydrodynamic equations using standard analytic techniques, and so one has to resort to numerical methods. There are two types of numerical schemes available viz. the finite difference schemes and the interpolation schemes. In the former, the computational domain is spatially divided into a hierarchy of grids. The equations governing fluid motion are then solved on this grid and the final solution is obtained by summing over it.

However, numerical errors contribute cumulatively and accumulate over grid cells. As a result, there is substantial magnification of the initial error. Physical quantities like linear and angular momentum therefore, may not be conserved, which is a major concern. Further, as condensations start forming in the computational domain, the use of grids with adaptive sizes becomes

computationally expensive as the grid structure becomes successively refined over such regions. SPH, on the other hand is a particle based interpolation scheme. It was first introduced by Lucy (1977) and Gingold & Monghan (1977) for simulation of problems in astrophysical hydrodynamics, since then its use has been extended to other areas involving fluids.

In SPH, the fluid under investigation is treated as an ensemble of particles, which are not point masses. Being a Lagrangian scheme the frame of reference co-moves with the fluid. This is an advantage as additional coordinate transformations are not necessary. SPH does not reproduce shocks very well as the numerical viscosity employed in SPH causes smearing (excessive smoothing) of shocks. The inability of SPH in handling hydrodynamic instabilities like the Rayleigh - Taylor (RT) & Kelvin - Helmholtz (KH) has recently been reported (Agertz *et al*, 2007). However, this shortcoming, especially in connection with the latter instability has been resolved (Price, 2007).

The resolution offered by SPH depends on the number of particles used. Hubber *et al* (2006) for instance, have shown that gravitational fragmentation is suppressed if the Jeans wavelength is inadequately resolved. However, Comercon *et al* (2008) suggest that a under - resolved system fragments on a time scale smaller than the growth rate of the Jeans instability, a numerical artifact. The question of adequate resolution of a system needs to be investigated in more detail.

We may draw a simple analogy between the particle - mesh (PM) method and SPH. The PM method is a hybrid scheme which uses features of both particle and grid methods. The force is calculated at a point and the field (Poisson) equation describing the underlying potential, is solved over the grid pervading the computational domain. The Laplacian operator in the Poisson equation is then replaced by its finite difference approximation on the grid. The potentials and the forces at particle positions are obtained by interpolation on the grid cells. This approximation introduces truncation errors. However, the accuracy of the results can be improved by making the mesh finer, in other words the spatial resolution provided by particle schemes (like SPH) can be improved by increasing the number of particles used, as has already been mentioned above.

3.1 Formulation of SPH equations :

In this section, I introduce the SPH equations. We shall not present any rigorous mathematical derivation of these equations here. In due course, some more features of this numerical scheme will also become clear. As mentioned above, SPH treats the fluid under investigation as an assembly of particles and the macroscopic properties of the fluid are estimated by first calculating the corresponding microscopic properties. The distribution of particles in the computational domain evolves both spatially and temporally. The statistical weights attached to contributions from individual particles smooth out random noise on the smallest scales. We shall revisit this below.

3.1.1 Density distribution :

Each SPH particle has a finite extent, the size of which is governed by a quantity called the smoothing length h. Thus, each SPH particle has a sphere of influence of radius $2h$ and particles lying within this sphere are called the nearest neighbours of the respective SPH particle. For the i^{th} SPH particle, if ρ_i, $\triangle v_i$ (note that this is not the SPH volume of a particle), and $\mathbf{r}_i$ are respectively, the density, volume, and position of its centre of mass, then its equation of motion is

$$\rho_i \triangle v_i \frac{d^2\mathbf{r}_i}{dt^2} = -\triangle v_i \nabla P + \rho_i \triangle v_i \mathbf{F}_i \tag{3.1}$$

$$\Rightarrow \frac{d^2\mathbf{r}_i}{dt^2} = -\frac{1}{\rho_i}\nabla P + \mathbf{F}_i, \tag{3.2}$$

where $\mathbf{F}_i$ is an external force acting on it and ∇P is the pressure gradient at $\mathbf{r}_i$. The individual particle density ρ_i is calculated by summing over weighted density contributions from the nearest neighbours. This weighting is done with the help of the weighting function, $W(r,h)$, also called the interpolating kernel. The purpose of the kernel function is to smooth discontinuities on the scale of the smoothing length. The search for the nearest neighbours of a particle can be performed using either the *gather* or the *scatter* scheme (Hernquist & Katz, 1989). Our SPH code DRAGON uses a hybrid combination of the two (Goodwin *et al*, 2004).

In the *scatter* approach every particle is treated as an extended point mass in space and has a finite mass associated with it, distributed according to the kernel $W(r,h)$. The density at a point in space is then calculated

by summing contributions from the densities of the surrounding particles. On the other hand, in the *gather* approach, every particle is treated as a point marker in the fluid and the density at a single point is calculated by summing over contributions from particles within the kernel radius of this single particle. If N_{neibs} is the desired number of neighbours that a SPH particle should have then, the individual SPH particle density is,

$$\rho_i \equiv \rho(\mathbf{r}_i) = \sum_{j=1}^{N_{neibs}} m_j \cdot W(\mathbf{r}_i - \mathbf{r}_j, h)$$

where j is the identifier of the nearest neighbours of the i^{th} SPH particle.

The smoothed density of the fluid, $\rho_s(\mathbf{r})$, is then given as,

$$\rho_s(\mathbf{r}) = \int W(\mathbf{r} - \mathbf{r}', h) \cdot \rho(\mathbf{r}')d\mathbf{r}', \tag{3.3}$$

where $\rho(\mathbf{r}')$ is the density of the fluid element at $\mathbf{r}$ and the kernel $W(\mathbf{r}-\mathbf{r}', h)$ satisfies the condition

$$\int W(\mathbf{r} - \mathbf{r}', h)d\mathbf{r}' = 1, \tag{3.4}$$

where the integration is carried out over the entire space (Gingold & Monaghan, 1977). In writing Equations (3.3) and (3.4) we have approximated the fluid as a continuum, so that discrete fluid particles now become fluid elements having the same spatial extent as individual SPH particles. Equation (3.3) is the SPH integral interpolant, however, for numerical work the particle approximation is preferable. The density of the i^{th} particle is given by the expression for ρ_i above. We can replace the integral in Equation (3.3) by a summation over N_{tot} particles and rewrite the equation as

$$\rho_{N_{tot}}(\mathbf{r}) = \frac{M}{N_{tot}} \sum_{i=1}^{N_{tot}} W(\mathbf{r} - \mathbf{r}'_i, h), \tag{3.5}$$

where

$$M = \int \rho(\mathbf{r}')d\mathbf{r}', \tag{3.6}$$

and once again the integration is over the entire space. This is the total mass of the system. The error introduced in approximating $\rho(\mathbf{r})$ by $\rho_{N_{tot}}(\mathbf{r})$ is of order σ^2, the variance. By definition,

$$\sigma^2 = < (\rho_{N_{tot}}(\mathbf{r}) - \rho(\mathbf{r}))^2 >$$

$$=< \rho^2_{N_{tot}}(\mathbf{r}) > - < \rho(\mathbf{r}) >^2$$

(by using the identity [1]). Using Equations (3.5) and (3.4), the above expression becomes,

$$\sigma^2 = \frac{M^2}{N^2_{tot}} \sum_i W^2(\mathbf{r} - \mathbf{r}_i, h) - \Big[\int W(\mathbf{r} - \mathbf{r}', h)\rho(\mathbf{r}')d\mathbf{r}' \Big]^2$$

$$\sim \frac{M^2}{N^2_{tot}} \sum_i W^2(\mathbf{r} - \mathbf{r}_i, h) - \frac{1}{N_{tot}} \Big[\frac{M}{N_{tot}} \sum_i W(\mathbf{r} - \mathbf{r}', h) \Big]^2. \qquad (3.7)$$

From Equation (3.7) we can see that the summation approximation of the integral interpolant introduces an error $O(N^{-2}_{tot})$. The kernel therefore, needs to be so chosen that in the limit $N_{tot} \to \infty$; $\rho_{N_{tot}}(\mathbf{r}) \to \rho(\mathbf{r})$ and $\rho_s(\mathbf{r}) \to \rho(\mathbf{r})$, in which limit $\sigma \to 0$. A delta function would be the ideal choice for the kernel.

Alternatively, the SPH equation of motion can be recast in Lagrangian form in which case the individual particle density and smoothing length can be self consistently determined. This also ensures exact conservation of energy (Price & Monaghan, 2006).

3.1.2 Estimating errors in SPH calculations :

The task of error estimation in SPH is non trivial since the particles are non static as their positions evolve with time. None the less, a simple 1-d error analysis will give us an idea of the order of approximation involved in the SPH interpolation scheme. The one dimensional SPH interpolant $F_I(x)$ is,

$$F_I(x) = \int F(x')W(x - x', h)dx'$$

$$= \int (F(x') - F(x) + F(x))W(x - x', h)dx' \qquad (3.8)$$

$$= F(x) + \int (F(x') - F(x))W(x - x', h)dx'.$$

We can now expand $F(x')$ using a Taylor series as,

$$F(x') = F(x) + (x - x')\frac{dF}{dx} + (x - x')^2 \frac{d^2F}{dx^2} + ...,$$

[1] if $b =< a >$, then $< (a - b)^2 >=< a^2 - 2ab + b^2 >=< a^2 > -2a < a > + < a >^2 =< a^2 > - < a >^2$.

so that the expression for $F_I(x)$ above becomes,

$$F_I(x) \sim F(x) + \int \Big((x-x')\frac{dF}{dx} + (x-x')^2\frac{d^2F}{dx^2}\Big)W(x-x',h)dx'$$

$$=F(x) + \int (x-x')\frac{dF}{dx}W(x-x',h)dx' + \int (x-x')^2\frac{d'^2F}{dx^2}W(x-x',h)dx' \tag{3.9}$$

$$=F(x) + \Big[(x-x')^2\frac{d^2F}{dx^2} - \int \Big(2(x-x')\frac{d^2F}{dx^2} + (x-x')^2\frac{d^3F}{dx^3}\Big)dx'\Big]$$

The first integral in Equation (3.9) has an odd integrand and therefore vanishes. Similarly, the third one vanishes on grounds of symmetry arguments. Using the definition of the variance in 1-d, the above expression then becomes,

$$F_I(x) = F(x) + \frac{\sigma^2}{d}\frac{d^2F}{dx^2} + ... \tag{3.10}$$

Equation (3.10) shows that, at least a second order error is involved in the interpolation scheme and, presumably in the fourth order as well. The reader is referred to Monaghan (2005) for a detailed discussion of the spatial error analysis and the stability analysis of the SPH interpolation can be found in Price (2004).

3.1.3 SPH smoothing length :

Let h_a and h_b be the respective smoothing lengths for the *gather* and *scatter* methods of neighbour finding. The hybrid smoothing length is defined as

$$\bar{h}_{ab} = \frac{1}{2}(h_a + h_b).$$

It has been found that the linear and angular momentum is better conserved using this latter prescription, as it maintains the symmetric nature of inter particle forces much better as compared to either of the other two, used individually (Hernquist & Katz, 1989). However, with spatially varying smoothing length the conservation of energy is not exact.

It is therefore necessary to calculate the smoothing length as accurately as possible which means a very small tolerance on the number of neighbours, ideally zero. To demonstrate the adverse effect of allowing tolerance over the number of neighbours on SPH density calculation, we carried out a

simple test. For the purpose, we use a fixed smoothing length i.e. all SPH particles are assigned the same smoothing length each time a neighbour search is attempted. This scheme admits a large tolerance on the number of neighbours each particle has, which in turn leads to large fluctuations in SPH densities. Let us fix the desired number of neighbours, $N_{neibs} = 50$. Particles located well within the computational domain easily find the desired N_{neibs} and some have surplus neighbours. The SPH sphere of influence of particles located near the edge of the computational domain, lies only partially within the domain. Such particles therefore, have fewer neighbours than desired, N_{neibs}.

As a test case consider a uniform density sphere of unit radius and unit mass (1 pc and 1 $M_\odot$ respectively), with N_{SPH} particles. The SPH density of particles within this sphere is calculated by using the expression for ρ_i stated above, with a fixed smoothing length h. This smoothing length is chosen according to Equation (3.11) below. The smoothing length for particles located very close to the edge of the sphere is then corrected by accounting for the SPH volume lost. Let N'_{neibs} be the number of neighbours actually found by these particles.

For simplicity let us assume that each particle has the same mass, m, where $m = \frac{1}{P_{SPH}}$. Particles in the sphere are positioned randomly using three random number generators, R_x, R_y, and R_z respectively, for the x, y, and z coordinates of a particle given by,

$$x = 1 - 2R_x$$
$$y = 1 - 2R_y$$
$$z = 1 - 2R_z.$$

Figure (3.1) below shows a projection of 5000 particles so assembled in this sphere.

The smoothing length of particles having $N'_{neibs} \neq N_{neibs}$, is iterated till they find N_{neibs} neighbours. For rapid convergence, the Newton - Raphson (NR) scheme is employed. In case the NR scheme failed to converge, a simple bisection method is implemented to force it.

The actual density of the sphere, ρ^{true}, is $\rho^{true} = \frac{3M_{sphere}}{4\pi R^3_{sphere}}$, which in the present case, is ~ 0.23 $M_\odot$ pc^{-3}. The volume of a SPH sphere of influence of a SPH particle is, $\frac{32\pi h^3}{3}$, so that the total volume of this sphere is the product of the number of particles (N_{SPH}) and the volume of an individual

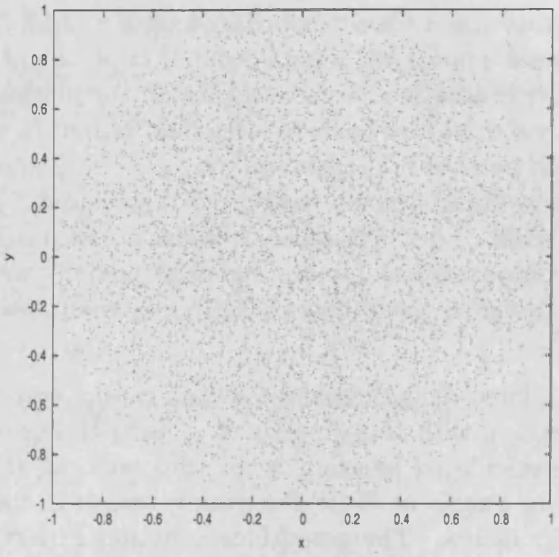

Figure 3.1: A 2-d projection of a uniform density sphere in the xy plane, $P_{SPH} = 5000$.

particle, i.e.

$$\frac{4\pi}{3} N_{neibs} \cdot 1^3 \cdot 1 = N_{SPH} \frac{32\pi h^3}{3}$$

$$\Rightarrow h = \frac{1}{2}\Big(\frac{N_{neibs}}{N_{SPH}}\Big)^{\frac{1}{3}}. \tag{3.11}$$

With this choice of the smoothing length, a nearest neighbour search is carried out for every particle. Neighbour deficient particles have fewer neighbours to sum over, and consequently SPH densities lower than ρ^{true}, converse is the case for particles having surplus neighbours. This is evident from the histogram of SPH densities shown in Fig. (3.2). It can be seen that there is a large spread of SPH densities about the expected density, ρ^{true}. This is a serious disadvantage of using a fixed smoothing length.

We now apply a volume compensation scheme to the particles located in an outer shell of thickness $2h$. Figure (3.3) shows a schematic diagram of this scheme. A projection of the uniform density sphere of radius R has been shown with a particle close to the edge, located at distance r_{mag} from its centre. The projected SPH sphere of influence of this particle has radius $H = 2h$, some part of which lies outside the projected parent sphere. Below,

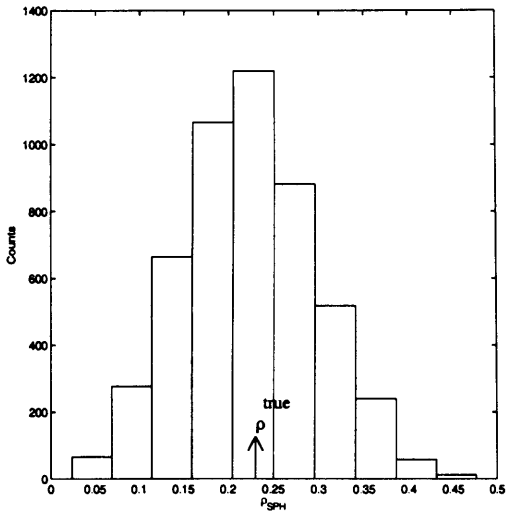

Figure 3.2: A histogram of ρ_{SPH} for $P_{tot} = 5000$. The arrow on the x axis indicates the expected density, ρ^{true}.

we first estimate the volume lost by a particle located in this region, using which the smoothing length is corrected. Let us call this corrected smoothing length h_{new}. The interpolating kernel is calculated using h_{new} and summed over the number of neighbours, the particle actually has (N'_{neibs}).

Let us now estimate the volume, V, lost by one such particle. Consider an infinitesimally thin ring of width dr at a distance r from the centre of the parent sphere, as shown in Fig. (3.3). Now, $\theta \equiv r\hat{}r_{mag}$, so that using the law of cosines we have,

$$H^2 = r_{mag}^2 + r^2 - 2r_{mag}r\cos\theta$$

$$\Rightarrow \theta = \cos^{-1}\left(\frac{r_{mag}^2 + r^2 - H^2}{2r_{mag}r}\right) \equiv \theta_{max}. \tag{3.12}$$

The required volume, V, is then

$$V = \int_{r=R}^{r=r_{mag}+H} \int_{\theta=0}^{\theta=\theta_{max}} 2\pi r^2 \sin\theta d\theta dr.$$

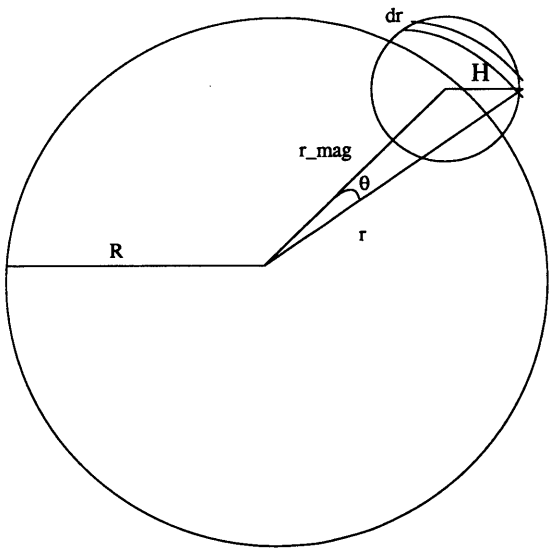

Figure 3.3: Schematic diagram illustrating the volume compensation scheme. See text for description.

Integrating over θ we get,

$$V = 2\pi \int_{r=R}^{r=r_{mag}+H} \Big(1 - \Big(\frac{r_{mag}^2 + r^2 - H^2}{2r_{mag}r}\Big)\Big) r^2 dr$$

$$= \pi \int_{r=R}^{r=r_{mag}+H} \Big(2r^2 - r_{mag}r - \frac{r^3}{r_{mag} + \frac{H^2 r}{r_{mag}}}\Big) dr$$

$$\Rightarrow V = \pi\Big(\frac{2r^3}{3} - \frac{r_{mag}r^2}{2} - \frac{r^4}{4r_{mag}} + \frac{H^2 r^2}{2r_{mag}}\Big)_{r=R}^{r=r_{mag}+H}. \qquad (3.13)$$

The number of neighbours actually found by this particle N'_{neibs} are,

$$N'_{neibs} = N_{neibs} - N_{neibs} \cdot f$$

$$= N_{neibs} - N_{neibs} \cdot \frac{3V}{32\pi h^3},$$

where f is the fraction of volume lost by a particle. Thus,

$$N'_{neibs} = N_{neibs}\Big(1 - \Big(\frac{3V}{32\pi h^3}\Big)\Big). \qquad (3.14)$$

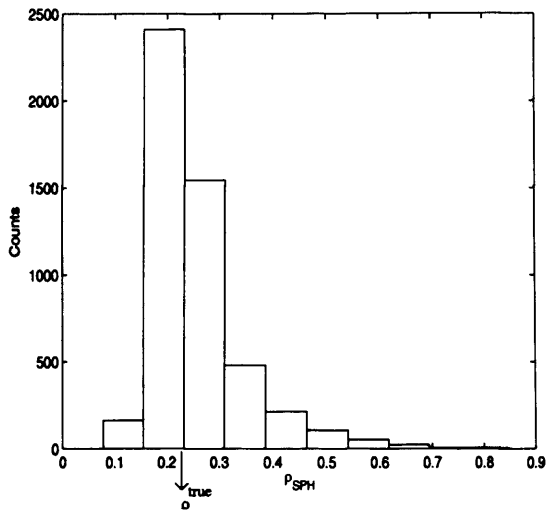

Figure 3.4: The histogram of ρ_{SPH} after implementing the volume compensation scheme, $P_{tot} = 5000$. The arrow indicates the value of the expected density ρ^{true}.

The new smoothing length, h_{new}, is obtained by rearranging Equation (3.14). The SPH density ρ_i for the i^{th} particle, is then calculated using the new smoothing length which is corrected as

$$\rho_i = \frac{\rho_i}{W_i^*}, \tag{3.15}$$

where

$$W_i^* \equiv W_i^*(\mathbf{r}_i) = \sum_{j=1}^{N'_{neibs}} W(\mathbf{r}_i - \mathbf{r}_j, h_{new}), \tag{3.16}$$

and all symbols have their usual meanings. Figure (3.4) shows the histogram of the SPH densities of particles after implementing this scheme. The arrow along the x axis as in the previous case, points at the actual density, ρ^{true}. This histogram is remarkably different from the one shown in Fig (3.2). Only $\sim$ 5% particles now have densites lower than the self density and a small percentage of them have exceptionally large densitites compared to ρ^{true}. This is certainly an improvement as compared to the previous calculation. The volume compensation scheme described above, is effectively a correction for missing neighbours. It avoids particles from having perilously

low densities as was evident from the histogram in Figure (3.2) above. We remind the reader, that the smoothing length of individual particles lying well within the computational domain is also iterated so that the number of neighbours they possess is always equal to the desired number N_{neibs}.

The importance of having zero tolerance on N_{neibs} has also been stressed by Attwood *et al* (2007), who showed that, admittance of a non - zero tolerance on N_{neibs} led to energy dissipation in an oscillating polytrope. However, the time scale of this energy dissipation is of order a few sound crossing times. The effects of the missing neighbour problem, on dynamical timescales therefore, need to be ascertained.

SPH resolution : In SPH, the extent of the smallest resolvable spatial element is governed by the smoothing length which in turn is decided by the number of particles used to represent the system under investigation. In the past it has been shown that particle methods performed better, as the number of particles used are increased (Potter, 1966). This holds true in case of SPH as well.

Hubber *et al* (2006) defined a resolution factor, $\mathcal{R}$, for resolving of the Jeans instability, as

$$\mathcal{R} = \left(\frac{mN_{neibs}}{M_{Jeans}}\right)^{\frac{1}{3}}, \tag{3.17}$$

where M_{Jeans} is the Jeans mass. According to them, the Jeans instability is best resolved when $\mathcal{R} << 1$. From Equation (3.17), it can be seen that the number of SPH particles available for resolving the instability is $\mathcal{R}^{-3} \cdot N_{neibs}$. Thus as $\mathcal{R} \rightarrow 0$, greater is the number of particles available to resolve the instability, for a fixed value of N_{neibs}. On the other hand, $\mathcal{R} > 1$ leads to poor resolution and the instability is suppressed.

Poor resolution of gravitational instability means that the subsequent gravitational fragmentation is also suppressed. Hence it is necessary to have sufficiently large number of particles to represent the system under investigation. Greater the number of particles used, smaller is the smoothing length, which in turn allows the smallest spatial regions to be resolved.

3.1.4 The SPH kernel :

The kernel plays a crucial role in convergence of the scheme and therefore, demands caution while choosing it. Since we desire localised contributions from particles (fluid elements), the kernel must satisfy the following two

properties,

$$\int W(\mathbf{r}-\mathbf{r}',h)d\mathbf{r}' = 1$$

and

$$\lim_{h\to 0} W(\mathbf{r}-\mathbf{r}',h) = \delta(\mathbf{r}-\mathbf{r}').$$

Ideally, a delta function would best suit the calculation of the contribution from individual particles; the prescription however, is difficult to handle mathematically. Hence splines are employed and in the limit of a vanishingly small smoothing length, they mimic the delta function. Thus, the contribution from every particle is reasonably localized.

A variety of options are available from which the kernel can be chosen, like the Gaussian or the (Heaviside) step function, spherical delta spline and polynomials. The polynomials, especially cubic splines (M_4) have yielded better results and since a cubic spline introduces errors only to the fourth order, it is more convenient to use them. [2] Other workers have experimented with Gaussian and various other splines as well. The standard M4 spline used is

$$W(\mathbf{r}-\mathbf{r}',h) = \frac{C}{h^\nu}\begin{cases} 1-\frac{3}{2}s^2+\frac{3}{4}s^3 & ;0\leq \mathrm{s}\leq 1 \\ \frac{1}{4}(2-s)^3 & ;1\leq \mathrm{s}\leq 2 \\ 0 & ;\text{otherwise,}\end{cases}$$

where $s = \frac{r}{h}$, ν is the number of dimensions and C is the normalisation constant, which in one, two, and three dimensions respectively, is $\frac{2}{3}$, $\frac{10}{7\pi}$, $\frac{1}{\pi}$ (Monaghan, 1992). Figure (3.5) shows the nature of this kernel. The argument s is plotted along the x - axis while the kernel $W(s)$ is plotted on the y - axis. In Figure (3.6) the first derivative (the spatial gradient) of the kernel has been plotted against its argument s.

Observe that, the gradient of the kernel has a local minima at $s \sim \frac{2}{3}$, the force between closely interacting particles is extremely small leading to particle clumping. To avoid this, an alternative is to add a conservative, non - zero repulsive force at vanishingly small separations. This ensures a monotonic

[2] Interpolation using polynomials of order higher 4 provide greater efficiency in the desired approximation. These are the *pp* (piecewise polynomial) functions and the basis over which such functions are defined is the B(Basis)- spline series. The space of mono splines forms a linear subspace on this basis. The cubic splines provide an accuracy of order $O(k)^4$, k is called the knot (sub interval within the interval on which the spline is defined) of the spline. Also, the fourth derivative of these splines vanish.

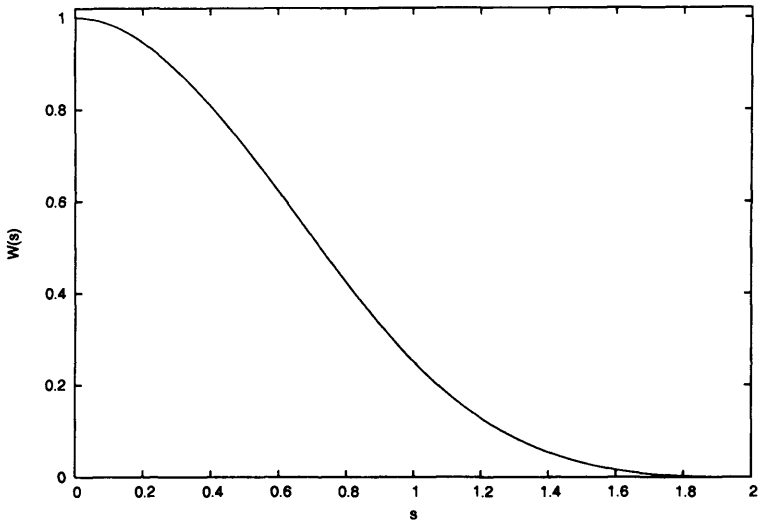

Figure 3.5: The standard M4 kernel.

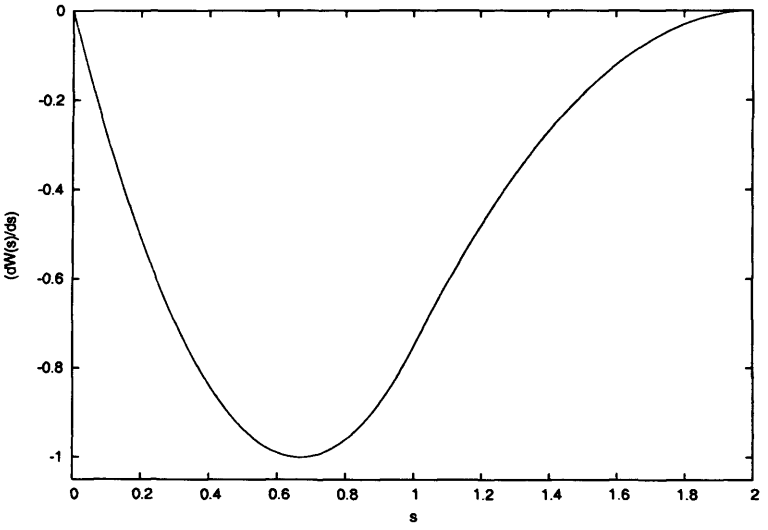

Figure 3.6: The derivative of the standard M4 kernel.

gradient of the kernel,

$$\frac{dW}{ds} = -\frac{1}{4\pi}\begin{cases} 4 & ,\mathrm{s} \leq \frac{2}{3} \\ 3s(4-3s) & ,\frac{2}{3} < \mathrm{s} \leq 1 \\ 3(2-s)^2 & ,1 < \mathrm{s} \leq 2 \\ 0 & ,\text{otherwise} \end{cases}$$

(Thomas & Couchman, 1992). Let us now look at the gravity calculation.

3.2 Calculating gravity using the Tree :

Computing the net gravitational force on a particle by direct summation is a trivial exercise. It has its advantages over other methods of calculations, in being very simple and Lagrangian. As a result, energy and momentum are exactly conserved and since all particles have the same size, the inter particle force is symmetric. However, the time required for computation is $O(N_{tot}^2)$, which makes the exercise computationally expensive, although advancements in technology have significantly increased the upper limit on N_{tot}. In a manageable simulation, the number of particles with which direct summation may be deemed feasible however, is still quite small. The computational expense is reasonable for a few hundred particles but enormous for a few thousand and unattainable for a few million particles.

Hence alternative methods have been tried. The Particle In Cell (PIC) method was one such scheme that was popularly used. The basic procedure involves construction of a grid enclosing the computational domain and physical quantities like the density, is calculated by solving the Poisson equation on the grid. The centre of mass of each cell on the grid acts as a fluid element (particle). This point particle has physical properties like mass, density, velocity etc. The total time required for the calculation is $O(N_{tot} + M \log M)$, where M is the number of vertices on the mesh. In practise $M << N_{tot}$, so that the computational time is $\sim O(N_{tot})$.

The PIC codes have shown good efficiency for a variety of astrophysical problems but are inefficient in dealing with strongly non uniform particle distributions, strongly correlated systems and systems with complex geometries. A variant of this scheme is the Particle - Particle Particle - Mesh (P^3M) method. It is a hybridisation of the PP and PM methods. In the P^3M method, the far field solution is corrected by including the local particle - particle interactions. However, this scheme requires that particles

are approximately uniformly distributed in the computational domain. The method provides solutions to a relatively low precision and fails in case of clustered distribution of particles. The computational expense increases with increasing local interactions (Potter, 1966).

To overcome the shortcomings of such schemes, Barnes & Hut (1986) and others proposed to use a nested hierarchy of clusters/cells. The net gravitational force on a particle is obtained by allowing each particle to interact with other particles in this hierarchy. The force due to the nearby particles is calculated by direct summation. Remote cells are treated as extended point masses and the accuracy of force calculation is improved by including their higher order moments. The earlier versions of such hierarchical trees by Appel, Jernigan and others had a few difficulties. The structure of these trees was arbitrary and unbalanced, some branches went too deep while others were shallower before terminating in leaf cells. Such an arrangement demanded complicated book keeping.

The Barnes-Hut algorithm : The essential feature of this tree is to confine the entire computational domain to a sufficiently large cube called the root (mother) cell. This cell is then spatially decomposed into eight daughter cells. . The particles are then cast into daughter cells. If any two particles fall in the same daughter cell then that cell is divided into eight subcells (child cells). The subdivision is continued so that finally, there is either one or no particle in the child cells at the lowest level of the tree. The empty daughter cells are discarded and only those having at least a single particle are retained. The tree is built at each step prior to evaluating gravitational and hydrodynamic forces.

The implementation of this algorithm in the SPH code DRAGON is slightly different (Goodwin, 2004). The mother cell is divided into eight daughter cells at the first level. Then at subsequent higher levels each daughter cell is further sub divided into eight child cells. This process is continued so that finally there are one to four particles in every child cell. The empty cells are discarded and the rest are numbered serially. Records of the occupants of every cell and the hierarchical order of the cells are maintained along with essential cell properties like the centre of mass and mass of each cell.

Once the tree is constructed, it can then be used to search the nearest neighbours of an individual particle. This is usually done by looking for a suitably large bounding box that contains the desired number of neighbours, N_{neibs}. The search can either be bottom up or top bottom.

3.2.1 Calculating gravity using the tree :

It has been noted above that the contribution from nearby particles is summed directly while that from the remote particles, is suitably approximated. We now define the criteria which decides the closeness/remoteness of cells. Each cell has size s, which for simplicity is approximated as the diagonal of that cell. Figure (3.8) shows one such cell located at a distance d from a particle, marked by $(\times)$. The angle subtended by this cell at the particle location is,

$$\theta = \frac{s}{d}. \tag{3.18}$$

This angle decides the nearness/remoteness of a cell and θ_{crit} is the maximum allowed value of θ. Distant cells subtend a small angle and vice - versa.

Cells qualifying the condition, $\theta > \theta_{crit}$, are *opened* and contributions from particles that cell are added by direct summation. On the other hand, those cells failing to satisfy this criterion are treated as extended point masses (pseudo particles). The parameter θ is therefore called the cell opening angle. θ_{crit} is usually less than unity and for most calculations the suggested value is 0.5 (Potter, 1966). For the present purpose $\theta_{crit} \sim 0.45$. Thus, in the limit $\theta \to 0$, the tree gravity scheme reduces to a simple direct summation. An extremely small value of the opening angle may improve the overall accuracy of the calculation, but then, the whole purpose of having a gravity tree is also lost.

If $\phi(r)$ is the potential of a pseudo particle having mass $M(r)$, then

$$\phi(r) = -\frac{GM(r)}{r}, \tag{3.19}$$

where r is the distance from its centre of mass. The RHS can be expanded about the centre of mass as,

$$\phi(r) = -\frac{GM(r_0)}{r_0} + \mathbf{r} \cdot \frac{1}{r_0^2} + \frac{1}{2}\Big(\sum_{l=1}^{3}\sum_{m=1}^{3} \frac{\partial^2 \phi}{\partial x_l x_m} x_l x_m\Big) + ...,$$

where r_0 is the radius of a small local region about the centre of mass. Then working out the respective derivatives in the third term above, we get

$$Q_{lm} = \sum_{l,m=1}^{3} m_{lm}(3x_l x_m - r^2 \delta_{lm}). \tag{3.20}$$

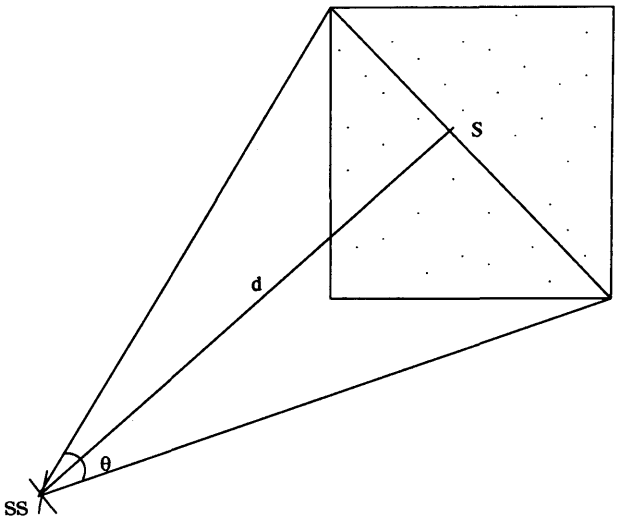

Figure 3.7: The figure shows a cell in the tree hierarchy having size s with particles in it, marked by points. For a particle located at a distance d from the centre of mass of this cell and marked by $\times$, θ is the angle subtended by the cell at this particle.

This is called the traceless quadrupole moment. The second term in the expression for $\phi(r)$ above, vanishes since the expansion is carried out about the CM, acting as the origin. The expression for the potential $\phi(r)$ then becomes,

$$\phi(r) = -\frac{GM}{r_0} - \frac{1}{2}\frac{G}{r_0^5}(\mathbf{r}\cdot\mathbf{Q}\cdot\mathbf{r}) + ... \tag{3.21}$$

Differentiating the potential twice yields the gravitational acceleration, given by

$$\mathbf{a}(\mathbf{r}) = -\frac{GM}{r_0^2}\cdot\hat{\mathbf{r}} + \frac{G}{r_0^4}(Q\cdot\hat{\mathbf{r}}) - \frac{5}{2}G(\hat{\mathbf{r}}\cdot Q\cdot\hat{\mathbf{r}})\frac{\hat{\mathbf{r}}}{r_0^4} + ... \tag{3.22}$$

The higher order terms can be included in the calculation to improve its accuracy.

3.2.2 Performance of trees vis a vis particle-particle methods :

Below, I discuss the performance of the tree gravity scheme, specifically its ability to conserve the essential physical quantities. A fundamental require-

ment of any numerical scheme is that, it should be efficient in conserving force and energy and not produce any undesirable, fictitious non - linear effects due to inter particle interactions. It is also demanded that the scheme is computationally inexpensive.

Processes where particle interactions manifest themselves are called collisional and ideally, we desire non - collisional processes. In reality it may not be possible to completely eliminate relaxation effects. Finite relaxation effects cause non conservation of energy and angular momentum (Hernquist & Barnes, 1990). In astrophysical systems, the two - body effects are negligible as their dynamical time scale is large. The relaxation time, t_r, of a system is defined as the average time over which binary particle interactions become negligible. It is defined as

$$t_r = \frac{\langle \triangle t \rangle}{\langle \sin^2 \gamma \rangle}, \tag{3.23}$$

where $\langle \triangle t \rangle$ is the average transit (crossing) time and $< \sin^2 \gamma >$ is the average value of $\sin^2 \gamma_i$. For a particle i, γ_i is the angle through which it is deflected after a collision. Obviously, larger the number of particles greater is the relaxation time. The total transit time is the sum over all such deflections. It has been found that the relaxation time in tree calculations is not vastly different as compared to other methods like the Particle - Particle (PP) method or the Particle - Particle - Mesh (PPM) method (Hernquist, 1987; Hockney & Eastwood, 1988).

The PP method is known to conserve angular momentum exactly, since it does not involve any approximation in evaluating pairwise interaction. It is simply a direct sum over all interacting particles. But conservation of energy is weakly violated due to truncation errors over subsequent time steps. Being computationally expensive, this method is unsatisfactory, as discussed previously. On the other hand, the errors involved in tree methods depend on the choice of the parameter θ, the cell opening angle. Moreover since a cluster of particles is treated as a single pseudo particle, it immediately implies violation of Newton's third law, due to asymmetry in the size of interacting particles. Consequently, there is also non conservation of linear and angular momenta. Smaller the value of θ, the more discretely is the particle ensemble treated in which limit, the tree scheme reduces to the PP method.

This has been demonstrated through numerical experiments, for instance by Barnes & Hut (1989). As a test case they consider the collision between two

identical spherical systems. Then with a fixed time step of 0.025 and $\theta = 1$, they note that the tree algorithm underestimates the potential by 0.3% to 0.8%, while the energy conservation is violated by ~2%. They then repeated the experiment, first by halving the time step, which had no effect either on the energy conservation or on estimation of the potential well. However, reduction of the opening angle to $\theta = 0.7$ showed that the violation of energy conservation reduced to ~1%.

Hernquist (1987) experimented with the calculation of gravity of the uniform density sphere and found that with a simple Leap - Frog integrator and a fixed time step = 0.025, the energy was conserved to 0.20 % for $\theta = 0$. Truncation errors were the main cause for this violation. For a large value of θ i.e. $\theta = 1$, after a thousand time steps the energy conservation was upto 0.68 % while that for $\theta = 0.5$ and the same number of time steps, violation of energy was less severe (0.32 %), but the percentage change in angular momentum was ~50 %. This experiment was performed with 4096 particles. With 32768 particles, after five hundred time steps the angular momentum was better conserved, upto 0.05 % for $\theta = 1$.

However, their results were corrupted due to the non conservation of linear momentum. A serious artifact of which is the dislocation of the centre of mass of the system. The effect was more pronounced for $\theta = 1$ and was observed to reduce considerably for $\theta = 0.5$. Numerical errors creep in for large values of θ due to asymmetry in particle sizes. To account for the force contribution of an enormous particle, it is essential to include its higher order moments, which increases computational expense and requires additional memory for storage of auxiliary variables. But neglecting them also exacts a cost. Thus, it is desirable to proceed with smaller values of θ. Thus, the tree method is robust, subject to an optimal choice of θ_{crit}.

3.2.3 Kernel softened gravity :

The force $\mathbf{F(r)}$ between two particles i, j having masses m_i and m_j respectively, and separated by distance r is

$$\mathbf{F(r)} = -\frac{Gm_i m_j \mathbf{r}}{r^3}, \tag{3.24}$$

where $\mathbf{r}$ is the vector from particle i to j. For vanishingly small particle separations this force tends to infinitely large values due to the singular nature of Newtonian gravity. Obviously, singularities are undesirable and

removal of this singularity yields a softened force. There are two ways in which this can be done, one is the Plummer softening and the second is Kernel softening. Plummer softening is straightforward and implemented by simply adding a vanishingly small constant ϵ in the denominator of Equation (3.24) to remove the singularity. Thus,

$$\mathbf{F}(\mathbf{r}) = -\frac{Gm_i m_j \mathbf{r}}{(r^2+\epsilon^2)^{\frac{3}{2}}} \tag{3.25}$$

This technique however, tends to excessively smooth Newtonian gravity as compared to the kernel softening. The extent of force softening depends on the choice of ϵ. Too large a value of ϵ tends to soften gravity much more than desired and vice versa. While studying problems like that of galactic mergers, small but finite value of ϵ may be insufficient in suppressing spurious noise on small scales. Thus, making an optimal choice of ϵ is a difficult question.

The second alternative, that of kernel softened gravity is more elegant as compared to the former. It uses the fact that SPH particles have a finite extent, governed by their respective smoothing length, h. The softened force between the particles i and j is,

$$\mathbf{F}(\mathbf{r}) = -\frac{4\pi G m_i m_j \mathbf{r}}{r^3} \int_0^r W(r,h) r^2 dr. \tag{3.26}$$

If $\Phi(r)$ is the corresponding gravitational potential per unit mass then, we know that

$$\mathbf{F} = -\nabla\Phi(r). \tag{3.27}$$

The SPH density of the i^{th} particle is,

$$\rho(\mathbf{r}_i) = \sum_{j=1}^{N_{neibs}} m_j W(\mathbf{r}_i - \mathbf{r}_j, h). \tag{3.28}$$

We now define the potential $\Phi(r)$ in analogy with equation (3.28) as

$$\Phi(r) = -G \sum_{j=1}^{N_{neibs}} m_j \phi(|\mathbf{r} - \mathbf{r}_j|, h), \tag{3.29}$$

where ϕ is the gravity softening kernel, a function of particle separation and smoothing length, h. $\Phi(r)$ is then the modified gravitational potential

per unit mass. Using Equations (3.28) and (3.29), the Poisson equation becomes,

$$-G\sum_{j=1}^{N_{neibs}} m_j \frac{1}{r^2}\frac{\partial}{\partial r}\Big(r^2\frac{\partial\phi}{\partial r}\Big) = 4\pi G\sum_{j=1}^{N_{neibs}} m_j W(r,h)$$

$$\Rightarrow W(r,h) = -\frac{1}{4\pi r^2}\frac{\partial}{\partial r}\Big(r^2\frac{\partial\phi}{\partial r}\Big). \tag{3.30}$$

This equation relates the density kernel, $W(r,h)$, to the softening kernel, $\phi(r,h)$. Those kernels having a finite nonzero kernel density as $r \to 0$ are called compact. Then, from Equation (3.30) it follows that

$$\frac{\partial\phi}{\partial r} \equiv \phi' = -\frac{4\pi}{r^2}\int_0^r W\cdot r'^2 dr', \tag{3.31}$$

where $W(r,h)$ is the standard M4 kernel. A trivial integration then yields,

$$\phi' = \begin{cases} \frac{1}{h^2}\Big(\frac{4}{3}s - \frac{6}{5}s^3 + \frac{1}{2}s^4\Big) & ;0 \le s \le 1 \\ \frac{1}{h^2}\Big(\frac{8}{3}s - 3s^2 + \frac{6}{5}s^3 - \frac{1}{6}s^4 - \frac{1}{15s^2}\Big) & ;1 \le s \le 2 \\ \frac{1}{r^2} & ;s > 2 \end{cases}$$

ϕ' is also called the force kernel. Integration of Equation (3.31) yields the gravitational softening kernel. Thus,

$$\phi(r,h) = 4\pi\int_0^r \frac{1}{r^2}\Big[\int_0^r Wr'^2 dr'\Big]dr,$$

integrating by parts we get,

$$= 4\pi\Big[-\frac{1}{r}\int_0^r Wr'^2 dr' + \int_0^r Wr' dr'\Big] + C,$$

For large values of r, the first term on the right hand side above vanishes and the density kernel, by its construction, vanishes outside the SPH sphere of influence of radius $2h$. In other words, $\phi(r,h)$, vanishes outside the kernel radius. This requirement of the gravitational kernel allows us to determine C, so that the above expression becomes,

$$\phi(r,h) = 4\pi\Big[-\frac{1}{r}\int_0^r Wr'^2 dr' + \int_0^r Wr' dr' - \int_0^{2h} Wr' dr'\Big]. \tag{3.32}$$

For the M4 cubic spline the softening kernel can be trivially evaluated using the above equation as,

$$\phi(r,h) = \begin{cases} \frac{1}{h}\left(\frac{2}{3}s^2 - \frac{3}{10}s^4 + \frac{1}{10}s^5 - \frac{7}{5}\right) & ;0 \leq s \leq 1 \\ \frac{1}{h}\left(\frac{4}{3}s^2 - s^3 + \frac{3}{10}s^4 - \frac{1}{30}s^5 + \frac{1}{15s} - \frac{8}{5}\right) & ;1 \leq s \leq 2 \\ -\frac{1}{r} & ;s > 2 \end{cases}$$

Not only is it essential for the kernel to fall off steeply to zero as $r \rightarrow 0$, but also the force, its first and (at least) the second derivative needs to be continuous (Dehnen, 2001).

3.3 Artificial viscosity :

Numerical techniques can handle equations of fluid dynamics with greater ease, in the absence of shocks. However, actual systems are seldom so simplified and colliding flows produce shocks. These are regions where physical quantities like density, temperature, velocity and entropy undergo rapid change accompanied with energy dissipation. This abrupt transition is treated by the Rankine - Hugoniot jump conditions. Mathematically, shocks are regions of discontinuities.

Solving the relevant differential equations across the surface of discontinuity becomes difficult if boundary conditions (BCs) are not properly defined. Hence BCs need to be so defined that physical variables on either sides of the surface of discontinuity are *smoothly* connected. We desire a mechanism that can account for this energy dissipation and heat conduction. Once this is done, the fluid can then be treated as a continuum. The artificial viscosity (AV) facilitates this process in SPH. However, the shock then no longer remains a surface having infinitesimally small thickness, but gets smeared over a finite region in space.

AV prevents interacting particles from penetrating through each other. In the absence of AV, SPH particles will just not *feel* each other in regions where they are within a few smoothing lengths. The full SPH equation of motion for i^{th} particle is

$$\frac{d\mathbf{v}_i}{dt} = -\sum_{j=1}^{N_{neibs}} m_j\left(\frac{P_i}{\rho_i^2} + \frac{P_j}{\rho_j^2} + \Pi_{ij}\right) \cdot \nabla_i W_{ij}, \tag{3.33}$$

where ∇_i is the spatial gradient of the kernel and W_{ij} is the usual interpolating kernel evaluated over particles i and j while Π_{ij} is the AV term,

defined as

$$\Pi_{ij} = \begin{cases} \frac{-\alpha \bar{a}_{ij} \mu_{ij} + \beta \mu_{ij}^2}{\bar{\rho}_{ij}} & ; \mathbf{v}_{ij} \cdot \mathbf{r}_{ij} < 0 \\ 0 & ; \mathbf{v}_{ij} \cdot \mathbf{r}_{ij} > 0; \end{cases} \tag{3.34}$$

where

$$\mu_{ij} = h_{ij} \frac{\mathbf{v}_{ij} \cdot \mathbf{r}_{ij}}{|\mathbf{r}_{ij}|^2 + \eta^2}, \tag{3.35}$$

$\bar{a}_{ij} = \frac{1}{2}(a_i + a_j)$, $h_{ij} = \frac{1}{2}(h_i + h_j)$, $\bar{\rho}_{ij} = \frac{1}{2}(\rho_i + \rho_j)$ and η is a vanishingly small constant which removes the singularity in the shock term (μ_{ij}), defined by Equation (3.35). Observe that AV vanishes for $\mathbf{v}_{ij} \cdot \mathbf{r}_{ij} > 0$, a condition analogous to $\nabla \cdot \mathbf{v} > 0$, which shows that AV is indeed dissipative. The interested reader is referred to Von - Neumann and Richtmeyer (1950) for a detailed perturbative analysis of the equations describing shocks, where numerical viscosity is shown to effectively damp perturbations in shocked regions and propagate without any amplification or decay, in normal regions.

In the context of SPH, this translates as: particles receding from each other are not influenced by AV as is evident from Eqn. (3.34). Shocks can be reasonably well captured with the standard choice of AV parameters, $\alpha = 1$ and $\beta = 2\alpha$. However, people experimenting with lower values of these parameters note the corruption of results due to post shock ringing effects. These are a consequence of pure bulk viscosity as in finite difference schemes and inadequate resolution of the interpolating kernel (Monaghan & Gingold, 1983; Meglicki, 1993). From Equation (3.34) it can be seen that the AV has two components, the first produces bulk viscosity while the quadratic term resembles the Von Neumann - Richtmeyer viscosity which prevents penetration of particles at high Mach numbers. AV in SPH is Galelian invariant and vanishes for pure rotation, also it conserves linear and angular momentum (Monaghan, 1992).

It is still the case that standard AV is far too efficient in damping, leading to softening of shocks. It suffers from another problem, that of spurious generation of entropy. It is therefore necessary to reduce it. Two alternatives have been suggested for the purpose. One being the time dependent viscosity and the other being the Balsara viscosity. In the former scheme, the bulk viscosity coefficient (α) falls off exponentially on either sides of the shock with a characteristic e - folding time (Monaghan, 1997). In the latter scheme however, the shock term is modified as,

$$\begin{aligned} \mu_{ij} &= \frac{h \mathbf{v}_{ij} \cdot \mathbf{r}_{ij}}{(a_i + a_j)(r_{ij}^2 + \eta^2)} (f(i) + f(j)), \mathbf{r}_{ij} \cdot \mathbf{v}_{ij} < 0; \\ &= 0, \text{otherwise}; \end{aligned} \tag{3.36}$$

where

$$f(i) = \frac{|\langle \nabla \cdot \mathbf{v} \rangle_i|}{|\langle \nabla \cdot \mathbf{v} \rangle_i| + |\langle \nabla \times \mathbf{v} \rangle_i| + \frac{0.0001 a_i}{h}}$$

(Balsara, 1995).

The functions $f(i)$ and $f(j)$ are called form functions. These functions carry information about the local flow around a particle. They contain terms for local compression and vortices. The form functions are designed such that they approach unity in regions of strong compression and vanish in regions of strong vorticity. We avoid a detailed discussion regarding the alternative forms of AV since they are not implemented in the current work. All simulations here have been performed using the standard AV prescription. It ia a matter of independent investigation to study the effect of variation of the standard AV parameters, on the colliding cloud experiments and the subsequent growth of shearing instabilities.

Finally, let us look at the time evolution of the thermal energy of SPH particles. The rate of change of thermal energy ($\mathcal{U}$) per unit mass is

$$\frac{d\mathcal{U}}{dt} = -\left(\frac{P}{\rho}\right) \cdot (\nabla \mathbf{v}).$$

Then, for the i^{th} particle this equation becomes,

$$\frac{d\mathcal{U}_i}{dt} = \frac{P_i}{\rho_i^2} \sum_{j=1}^{N_{neibs}} m_j \mathbf{v}_{ij} \cdot (\nabla_i W_{ij}), \tag{3.37}$$

where use has been made of the relation[3] for the gradient of the interpolant, and $\mathbf{v}_{ij} = (\mathbf{v}_i - \mathbf{v}_j)$, $W_{ij} = W(\mathbf{r}_i - \mathbf{r}_j, h)$.

Using the identity

$$\nabla \cdot \mathbf{v} = \frac{1}{\rho}[\nabla(\rho \mathbf{v}) - \mathbf{v}(\nabla \rho)] \tag{3.38}$$

[3]The summation interpolant A_I is given by

$$A_I = \sum_{j=1}^{N_{neibs}} m_j \frac{A_j}{\rho_j} W(\mathbf{r} - \mathbf{r}_j, h),$$

where symbols have their usual meanings. The gradient of A_I is then,

$$\nabla \cdot A = \sum_{j=1}^{N_{neibs}} m_j \frac{A_j}{\rho_j} \nabla W(\mathbf{r} - \mathbf{r}_j, h).$$

However, for higher accuracy it is advisable to use the identity $\rho \nabla A = \nabla(\rho A) - A \nabla \rho$.

and the following expressions,

$$\nabla\rho = \sum_{j=1}^{N_{neibs}} m_j(\nabla W(\mathbf{r}-\mathbf{r}_j,h)) \tag{3.39}$$

$$\nabla(\rho\mathbf{v}) = \sum_{j=1}^{N_{neibs}} m_j\mathbf{v}_j(\nabla W(\mathbf{r}-\mathbf{r}_j,h)), \tag{3.40}$$

the expression for the gradient of velocity for the i^{th} particle becomes

$$(\nabla\mathbf{v})_i = \frac{1}{\rho_i}[\sum_{j=1}^{N_{neibs}} m_j\mathbf{v}_j(\nabla_i W(\mathbf{r}_i-\mathbf{r}_j,h)) - \sum_{j=1}^{N_{neibs}} m_j\mathbf{v}_i(\nabla_i W(\mathbf{r}_i-\mathbf{r}_j,h))]$$

$$\Rightarrow \rho_i(\nabla\mathbf{v})_i = \sum_{j=1}^{N_{neibs}} m_j(\mathbf{v}_j-\mathbf{v}_i)\cdot(\nabla_i W_{ij}). \tag{3.41}$$

Following this, the thermal energy equation given by Equation (3.37) with the dissipative term, becomes

$$\frac{d\mathcal{U}_i}{dt} = \frac{P_i}{\rho_i^2}\sum_{j=1}^{N_{neibs}} m_j\mathbf{v}_{ij}\cdot(\nabla_i W_{ij}) + \frac{1}{2}\sum_{j=1}^{N_{neibs}} m_j\Pi_{ij}\mathbf{v}_{ij}\cdot(\nabla_i W_{ij}). \tag{3.42}$$

A factor of $\frac{1}{2}$ appears in the second term of the above equation to avoid repeated contribution during the summation over all particles. The energy equation in this form is asymmetric and leads to violation of linear and angular momentum conservation. It is therefore beneficial to symmetrise the expression. This can be done as follows. The rate of change of internal energy per unit mass can be alternatively written as,

$$\frac{d\mathcal{U}}{dt} = -\nabla\Big(\frac{P}{\rho}\mathbf{v}\Big) + \mathbf{v}\nabla\Big(\frac{P}{\rho}\Big).$$

Then making use of the identity in footnote 3, we get

$$\nabla\Big(\frac{P}{\rho}\mathbf{v}\Big) = -\sum_{j=1}^{N_{neibs}} m_j\frac{P_j}{\rho_j^2}\mathbf{v}_j\cdot(\nabla W_{ij}) \tag{3.43}$$

and

$$\mathbf{v}\cdot\nabla\Big(\frac{P}{\rho}\Big) = \sum_{j=1}^{N_{neibs}} m_j\frac{P_j}{\rho_j^2}\mathbf{v}_j\cdot(\nabla W_{ij}). \tag{3.44}$$

Hence,

$$\frac{d\mathcal{U}_i}{dt} = \sum_{j=1}^{N_{neibs}} m_j \frac{P_j}{\rho_j^2} \mathbf{v}_{ij} \cdot (\nabla_i W_{ij}), \tag{3.45}$$

where $\mathbf{v}_{ij} = \mathbf{v}_i - \mathbf{v}_j$. Then combining Equations (3.42) and (3.45) we get

$$\frac{d\mathcal{U}_i}{dt} = \frac{1}{2} \sum_{j=1}^{N_{neibs}} m_j \Big(\frac{P_j}{\rho_j^2} + \frac{P_i}{\rho_i^2} \Big) \mathbf{v}_{ij} \nabla_i W_{ii}, \tag{3.46}$$

but without the dissipation term Π_{ij}, and the total energy E of the system is,

$$E = \sum_{i=1}^{N_{tot}} m_i \Big(\frac{1}{2} |\mathbf{v}_i|^2 + \mathcal{U}_i \Big). \tag{3.47}$$

3.4 Time stepping, the integration scheme and its stability :

3.4.1 Time stepping :

The simplest time stepping scheme is one which uses a predefined fixed time step. However, one is then required to make an optimal choice of this time step, which may not always be a trivial task. The time step needs to be so chosen that the integration remains stable and the trajectory of the particles is well described.

In the global time stepping scheme, this choice of the time step, dt, is assigned to all the particles in the computational domain. One objective criterion for choosing an optimal time step is the Courant condition, which sets a upper limit on the time step. This in turn is related to the maximum spatial resolution available in the system under investigation (Hockney & Eastwood, 1988). In SPH calculations, the spatial resolution depends on the smoothing length h so that the Courant condition yields,

$$dt_{CFL} = \min_i \Big(\frac{h_i}{v_i + a_i} \Big); \tag{3.48}$$

where i is the identifier of a particle and a_i is the sound speed associated with it.

Apart from this, time steps based respectively, on the force per unit mass and artificial viscosity are calculated as

$$dt_a = \min_i\left(\sqrt{\frac{h_i}{|\mathbf{f}_i|}}\right) \tag{3.49}$$

$$dt_V = \min_i\left(\frac{h_i}{v_i + 1.2(\alpha a_i + \beta \max_j \mu_{ij})}\right); \tag{3.50}$$

where symbols have their usual meanings. The i^{th} particle is then assigned the time step,

$$dt = 0.02 \cdot \min(dt_{CFL}, dt_a, dt_V).$$

The premultiplier in the expression above is to ensure stability of the integration scheme.

Using the time step, dt, so calculated, every particle in the simulation is advanced. The integration process is described in the following sub section. Before proceeding to the description of the integration scheme, we must look at the disadvantages of this simple scheme. That would also pave the way to the more sophisticated, block time stepping scheme.

The disadvantage of the global time stepping scheme is clearly evident. It may work satisfactorily as long as the density of individual particles in a simulation is not too high and there are no condensations. However, once they start forming in a particular region, the local density increases dramatically as a result of which the smoothing length becomes extremely small. Consequently the corresponding time step also becomes very small. If rest of the particles in the simulation are assigned this time step then, obviously the simulation will crawl at snail's pace and eventually come to grinding halt. The scheme is thus, computationally expensive and hence, unsatisfactory.

3.4.2 Integration scheme :

The equations of motion are not continuous in the strictest sense, but are discretised in suitable subintervals of time. The position and velocity of the particles at the present instant of time is calculated by using the corresponding values at the previous instant. Here we use a simple second order Runge - Kutta (RK) integration scheme. The RK integration schemes are quite accurate and have the added advantage of not requiring to store too many auxiliary variables. Hence they are one of the best known integration schemes (Henricki, 1962).

At a given time step, each particle in the simulation is advanced and the necessary forces are recalculated. Thus, the gravity tree is built at each time step. Time step here, implies the actual real time interval of advancement. The total number of time steps required over the entire integration period are counted by integer time steps, both of which are recorded and updated separately. In practice one real time step dt corresponds to two integer time steps. This is simply to avoid keeping track of the fraction $\frac{1}{2}$ corresponding to each half of the RK integration scheme, a half integration step corresponds to one integer time step.

Integration of the equation of motion of a particle yields the velocity of that particle ($\mathbf{v}_i^n(\mathbf{r},t)$). The subscript refers to the identifier of the i^{th} particle and the superscript is the n^{th} integer time step. To calculate the position $\mathbf{r}_i^n$ and the velocity $\mathbf{v}_i^n$, we require their respective values at the $(n-1)^{th}$ time step. The particle i is then advanced to the new position $\mathbf{r}_i^{n+1}$ according to the following set of equations,

$$\mathbf{v}_i^{n-1} = \frac{1}{2}\mathbf{v}_i^{n-1} \tag{3.51}$$

$$\mathbf{r}_i^n = \mathbf{r}_i^{n-1} + (\mathbf{v}_i^{n-1} \cdot dt) \tag{3.52}$$

$$\mathbf{v}_i^n = \mathbf{v}_i^{n-1} + (\mathbf{a}_i^{n-1} \cdot dt). \tag{3.53}$$

Once the particles have been advanced using Equation (3.51), the forces are recalculated and the particles are advanced through the next half step of the RK scheme,

$$\mathbf{r}_i^{n+1} = \mathbf{r}_i^n + (\mathbf{v}_i^n \cdot dt) \tag{3.54}$$

$$\mathbf{v}_i^{n+1} = \mathbf{v}_i^n + (\mathbf{a}_i^n \cdot dt). \tag{3.55}$$

Rigorous error analysis of the RK scheme has shown that it is stable and amplification of errors can be limited by having a sufficiently small time step. The reader is referred to Henrici (1962) for the relevant mathematical details.

3.4.3 Block time stepping scheme :

This scheme, also called multiple particle time stepping, is used to overcome the disadvantage of the global time stepping scheme described in §3.4.1. This

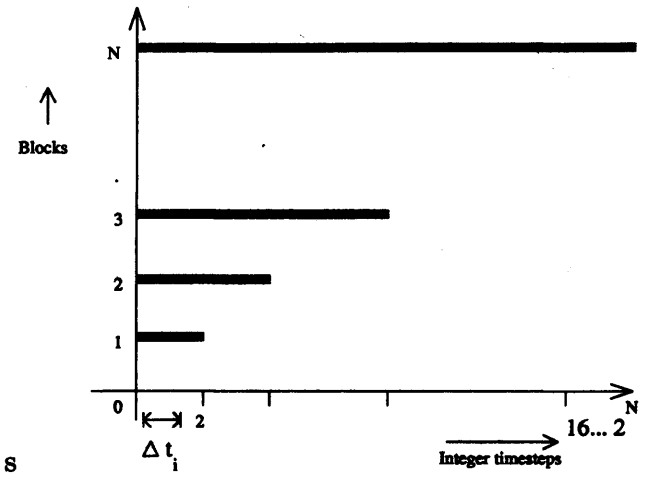

Figure 3.8: Diagram illustrating the block time stepping scheme. In the case shown here, Δt_i is the real time step of a particle i, whose corresponding integer time step is smaller than 2^1, hence it belongs to the first block.

scheme is able to account for different time scales of evolution of particles in the computational domain. Particles belonging to quiescent regions evolve on a longer dynamic timescale than others and vice - versa. However, in order to keep a record of the global real time, synchronisation of particles is essential. Individual particle time steps are assigned in hierarchical blocks, in powers of 2 (Mc Millan & Aarseth, 1993).

If dt_i is the time step of the i^{th} particle then

$$dt_i = 2^N dt_0, \tag{3.56}$$

where dt_0 is some fictitious time step and N is an integer, sum of two quantities viz. the minimum number of time stepping levels allowed for a particle to find a suitable time step block to which it belongs and a certain number of extra levels to account for the occurrence of extremely small time steps when a condensation begins to occur in the computational domain. These additional levels act as a safeguard against particles running out of suitable time stepping blocks. In the current calculations fifteen spare levels have been used. Alternatively, one could opt for many more levels but various numerical experiments suggest that this number is sufficient (private communication; Goodwin, 2006).

Depending on the real time step dt_i, suitable time stepping blocks are as-

signed to particles. At a given instant of time, consider particles belonging to a certain block say n, all of which do not need to be transferred to a new block, say m. Since we do not need to transfer particles enmasse, the scheme is computationally inexpensive and scales as $(N_{tot})^{\frac{1}{3}}$, while in case of dense clustering (i.e. with large number of condensations - the worst case scenario), the scheme costs only as much as $O(N_{tot})$ (Makino, 1991). The objective now is to predict the particles whose time stepping block needs to be updated, which is done using the integer time steps. We need to maintain a record of the maximum integer time corresponding to the time block to which the particle belongs. Let n_i be this block, so that the corresponding integer time step length is 2^{n_i}. Additionally, the integer length of the current time step is also maintained.

The real time step is given by Equation (3.56). Figure (3.8) gives a rough idea of how the scheme works. On the x axis, the integer time step has been marked in powers of two. On the y axis, time stepping blocks have been shown. To illustrate the scheme, a real time step Δt_i with corresponding integer time step less than 2^1 has been shown. Obviously, it belongs to the first block on the y axis.

When the current integer time step length for particles in a certain block becomes greater than the maximum integer time step length of a block then all particles of that block are updated to a new block. Nothing is done to particles which fail to qualify this test. They continue to hold the same time stepping block as previously held. Once all the particles are assigned respective blocks, the list of the presently and previously held integer time steps by individual particles, is updated. Forces need to be recalculated for those particles which have reached their half time steps (i.e the integer division of the integer time step held by a particle with two, should yield 1). The forces are then recalculated in the usual way. All the particles are advanced with the respective time steps they posses. Figure (3.9) shows a flow chart of this time stepping scheme.

This scheme is computationally cheap but, with block time steps almost every particle is forced to have a time step smaller than its actual time step, at least by a factor of $2^{\frac{1}{2}}$ on average (McMillan & Aarseth, 1993). This does introduce a slight error in time stepping, but within acceptable limits.

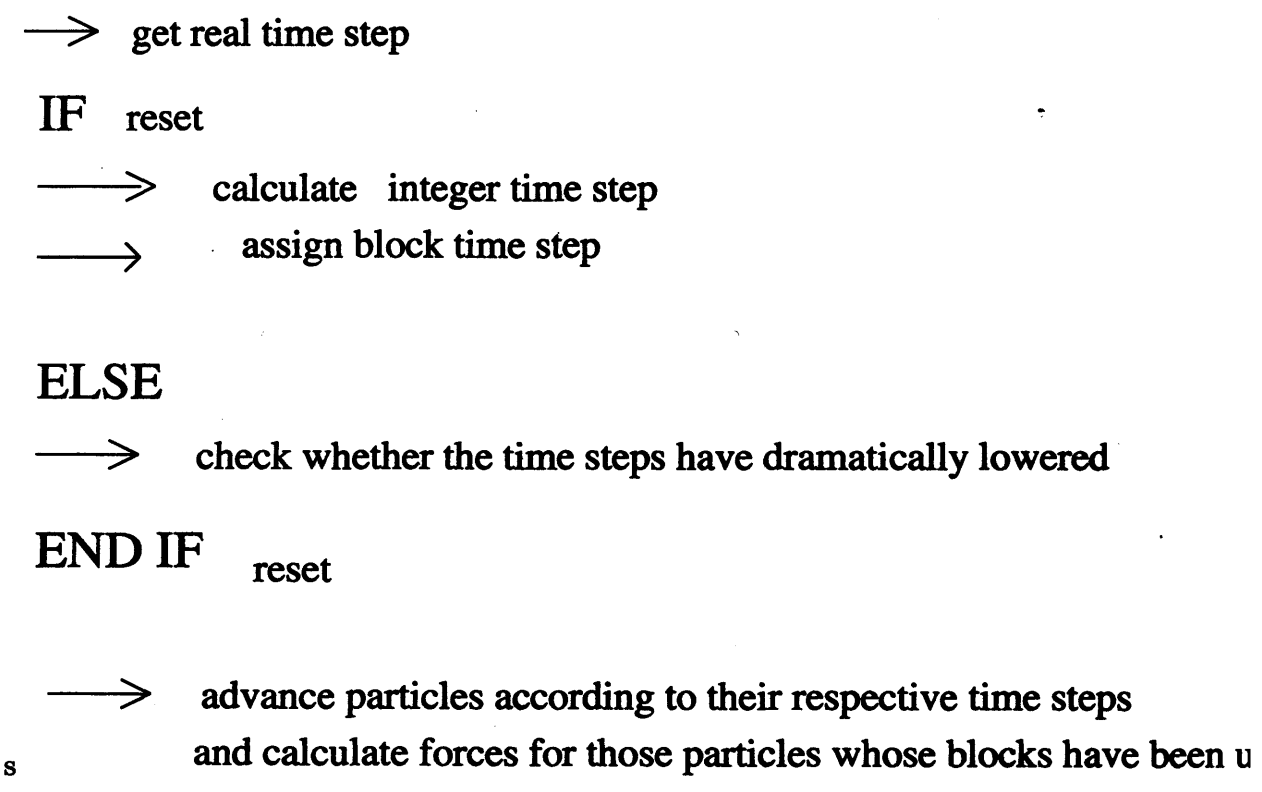

Figure 3.9: Flow chart of the block time stepping scheme.

Chapter 4

Cloud - Cloud Collisions

After a brief synopsis of the numerical scheme used for the investigation of the cloud collision problem, below I first describe our simple model for the molecular clouds (MCs), and then the process of setting up the initial conditions for the MC collision experiments. I then list the simulations performed. All but one, are head on collision experiments of physically identical clouds. The one exception is that of two identical clouds colliding at a small impact parameter leading to the formation of an oblique shock compressed slab.

4.1 Modelling MCs :

The MCs have been simply modelled as external pressure confined isothermal (Bonnor - Ebert) spheres, discussed previously in chapter 2. Various relevant physical properties of these spheres have already been examined in §2.2.1. For simplicity we assume that the gas in the cloud is plain H_2.

4.1.1 Assembling the isothermal sphere :

Particles can be assembled either on a regular HCP lattice or randomly positioned. In the present case, we choose this latter approach. Random positioning of particles is associated with statistical noise, which can be minimised by increasing the number of particles used. To further minimise noise in the particle assembly, we relax the configuration before commencing an experiment. Such a relaxed configuration is called a *glass*.

As a test case, we first assemble an isothermal sphere with N_{sphere} particles and settle it to form a glass. This test sphere has unit mass (1 $M_\odot$) and unit radius (1pc) so that it can be readily scaled to any desired physical dimension. In §2.2.1 above we briefly discussed the stability of an isothermal sphere. There it was shown that a hydrodynamically stable configuration is possible for $\xi < \xi_{crit} = 6.45$. In all our simulations we choose $\xi = \xi_B = 3$, where the symbols have their usual meanings.

For a fixed dimensionless radius of an isothermal sphere, the isothermal sound speed a_0 within the sphere can be obtained as follows. We know that $r_B = R_0 \xi_B$ i.e.

$$r_B = \frac{a_0 \xi_B}{(4\pi G \rho_c)^{\frac{1}{2}}}, \tag{4.1}$$

where we have simply used the definition of the physical scale factor, R_0. The mass interior to r_B i.e. the total mass of the sphere is given by Equation (2.26). Taking the ratio of M_{sphere} with r_B we get,

$$\frac{M_{sphere}}{r_B} = \frac{a_0^2 \mu(\xi_B)}{G \xi_B}$$

$$\Rightarrow a_0^2 = \frac{G M_{sphere} \xi_B}{r_B \mu(\xi_B)}. \tag{4.2}$$

We now convert Equation (4.2) into its dimensionless form. Let $\hat{a}_0$ be the dimensionless isothermal sound speed and $T_\square$, $L_\square$ & $M_\square$ be the SFC units of time, length and mass respectively. Then simple dimensional analysis suggests that

$$\hat{a}_0^2 = \frac{T_\square^2 a_0^2}{L_\square^2}$$

but,

$$T_\square^2 = \frac{L_\square^3}{G M_\square}$$

$$\Rightarrow \hat{a}_0^2 = \frac{L_\square a_0^2}{G M_\square}.$$

If $\hat{M}_{sphere}$, $\hat{R}_{sphere}$ are the dimensionless mass and radius of the sphere respectively, then $M_{sphere} = M_\square \hat{M}_{sphere}$ and $R_{sphere} = L_\square \hat{R}_{sphere}$. Then using these relations and Equation (4.2), the expression for the dimensionless sound speed becomes,

$$\hat{a}_0^2 = \frac{\hat{M}_{sphere} \xi_B}{\hat{R}_{sphere} \mu(\xi_B)}. \tag{4.3}$$

By choice, $\hat{M}_{sphere} = 1$ and $\hat{R}_{sphere} = 1$ each, so that Equation (4.3) simply reduces to

$$\hat{a}_0^2 = \frac{\xi_B}{\mu(\xi_B)}. \tag{4.4}$$

The physical isothermal sound speed is defined as

$$a_0 = \left(\frac{k_B T}{\bar{m}}\right)^{\frac{1}{2}}, \tag{4.5}$$

where $\bar{m}$ is the mean molecular mass and $\bar{m} \sim 4 \times 10^{-24}$ gm. Equations (4.2) and (4.5) fix the temperature of the particles within the sphere.

Three random number generators, each generating a random number in the range (0,1) are used to fix the positions of individual particles within this sphere. A random number $\mathcal{R}_r$ is chosen such that,

$$\frac{M(r)}{M_{sphere}} = \frac{\mu(\xi)}{\mu(\xi_B)} \equiv \mathcal{R}_r \tag{4.6}$$

$$\Rightarrow \mu(\xi) = \mu(\xi_B)\mathcal{R}_r.$$

Knowing the RHS of the above expression, the corresponding dimensionless radius ξ can be obtained from the Lane - Emden table. The radial distance r at which a particle is positioned within the sphere is then given by $r = \frac{\xi}{\xi_B}$. The probability that a particle will lie within the range θ and $\theta + d\theta$ of the poloidal angle is

$$p_\theta d\theta = \frac{\sin\theta}{2} d\theta.$$

So the total probability over the range of the variable θ is,

$$P(\theta) = \int_{\theta'=0}^{\theta'=\theta} \frac{\sin\theta'}{2} d\theta' = \frac{1 - \cos\theta}{2} \equiv \mathcal{R}_\theta, \tag{4.7}$$

where $\mathcal{R}_\theta$ is the second random number. Thus,

$$\cos\theta = 1 - 2\mathcal{R}_\theta.$$

Finally the azimuthal coordinate, ϕ, of a particle is given by $\phi = 2\pi\mathcal{R}_\phi$, where $\mathcal{R}_\phi$ is the third random number. The (r, θ, ϕ) coordinates of a particle are easily converted to their cartesian form in the usual way.

Equation (2.27) gives the density as a function of the radial coordinate for an isothermal sphere of infinite extent. By substituting $\xi = \xi_B$ in this equation, we get the density for a truncated isothermal sphere. In all the simulations

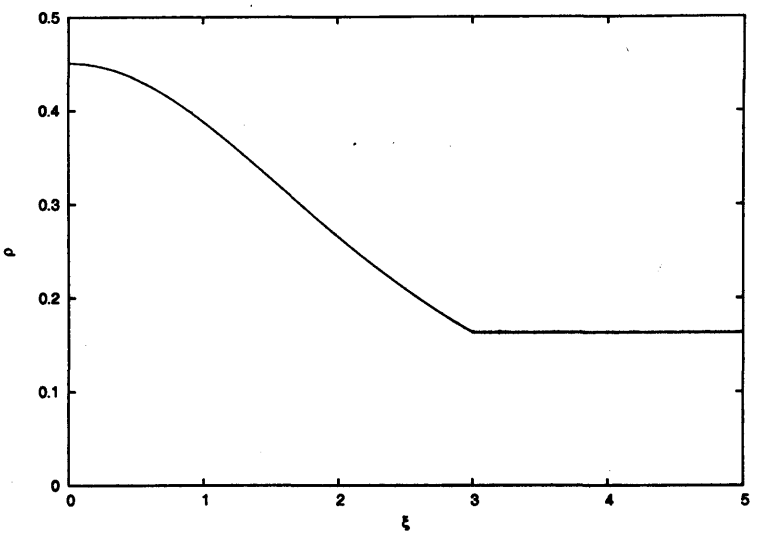

Figure 4.1: Density profile for truncated isothermal sphere (ξ_B=3).

performed here, we set $\xi_B = 3$ so that the isothermal sphere is in the stable regime of its equilibrium characteristic (see Figure (2.4)). The density profile of such a sphere having mass and radius 1 $M_\odot$ and 1pc respectively, is shown in Figure (4.1). Note that the region outside the sphere is maintained at the same density as that at the edge of the sphere.

4.1.2 Assembling external pressure particles :

Without external pressure such a sphere would simply diffuse away in space. The magnitude of external pressure (P_{ext}) required to confine this sphere is given by Equation (2.30) above. We assemble particles that mimic the ICM by exerting a finite external pressure (P_{ext}) on the cloud boundaries.

The ICM particles are non self - gravitating and, are separately assembled in an envelope of thickness, ηh_B, where η is a nonzero integer ($\eta = 5$ in the present case) and h_B is the average smoothing length for a SPH particle. We first obtain an expression for the density at the edge of the cloud in its dimensionless form. Using Equation (4.2), we transform Equation (2.27) into dimensionless variables, to get

$$\hat{\rho}_B = \frac{\xi_B^3 e^{-\psi(\xi_B)}}{4\pi\mu(\xi_B)}. \tag{4.8}$$

The particle number density at the edge of the sphere is $\hat{n}_B = \frac{\hat{\rho}_B}{m} \equiv N_{sphere}\hat{\rho}_B$. The mass of a single particle is $m = \frac{1}{N_{sphere}}$, for a sphere of unit mass. The volume of the envelope is then $\frac{4\pi[(1+\eta \cdot h_B)^3-1]}{3}$, so that the number of particles to be assembled in the envelope is the product of this volume with the particle number density ($\hat{n}_B$). The average smoothing length of a SPH particle is calculated using Equation (3.11).

For a sphere with $N_{sphere} = 1500$ and $\eta = 5$, the number of particles in the envelope is $N_{env} = 6159$. The radial coordinate (r) of a particle in the envelope is fixed by choosing a random number $\mathcal{R}_r$ such that the volume interior to this radius is proportional to the volume in the envelope i.e

$$\mathcal{R}_r = \frac{(r^3 - 1)}{((1 + \eta h_B^3)^3 - 1)}.$$

The poloidal angle (θ) for a particle, is obtained by using Equation (4.7) and the azimuthal angle (ϕ), as before. The polar coordinates of individual particles are then converted to cartesian form by invoking the usual coordinate transformation. With this the assembly of the sphere - envelope system is completed.

This assembly of the sphere - envelope combination is then placed in a periodic box and allowed to evolve. The periodic box is only meant for ghosting particles near the box edges. Particles leaving from one face of the cube re - enter from the opposite face. The configuration is evolved for a fraction of the sound crossing time and allowed to relax. Figures (4.2) through (4.4) show the SPH density, gravity and the hydro acceleration respectively, after about half a sound crossing time. By this time the noise in the calculation of these quantities has considerably diminished. They are now in reasonable agreement with the expected profile, marked by the dashed continuous curve in respective figures.

4.2 Experiments with colliding MCs :

The MCs used in collision experiments are physically identical in every respect. This restriction simplifies the matter of setting up initial conditions however, it could be easily relaxed. Both MCs have the same initial speed but opposite directions, and move towards each other. As a result, post - collision a stationary shock compressed slab is formed.

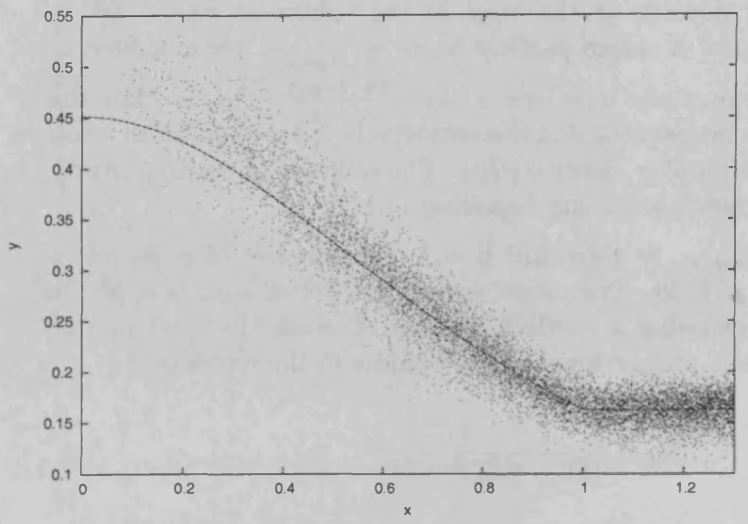

Figure 4.2: ρ_{SPH} for a truncated isothermal sphere (ξ_B=3). The continuous line is the expected density profile for this sphere. (x≡ ξ; y≡ ρ_{SPH}), P_{sphere}= 1500.

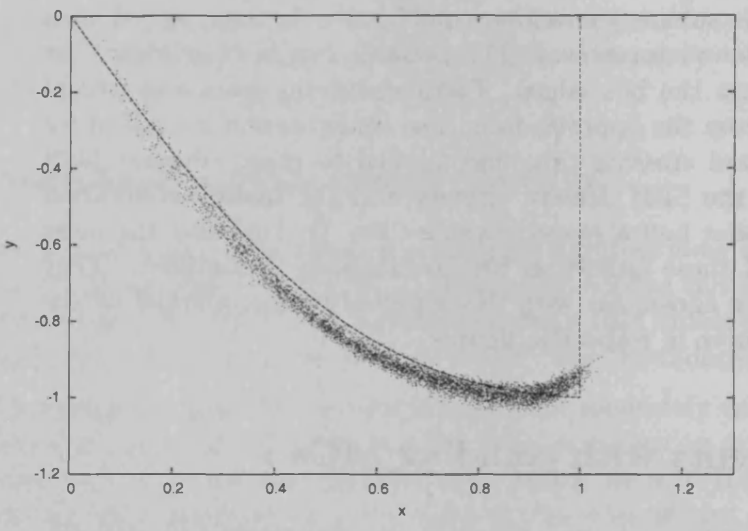

Figure 4.3: Gravity for a truncated isothermal sphere (ξ_B=3). The continuous line is the expected profile of a_{grav} for this sphere. (x≡ ξ;y≡ a_{grav}), P_{sphere}= 1500.

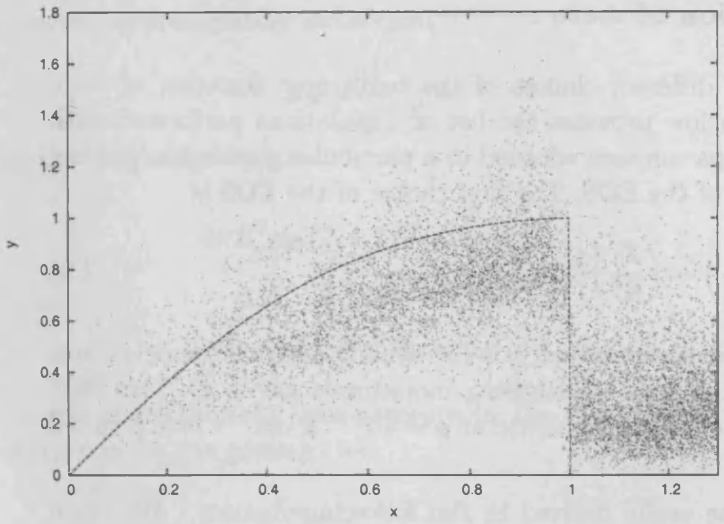

Figure 4.4: Hydro acceleration for a truncated isothermal sphere (ξ_B=3). The continuous line is the expected profile of a_{hydro} for this sphere. (x≡ ξ; y≡ a_{hydro}), P_{sphere}= 1500.

In all the experiments described here, the MCs move at supersonic precollision velocities. We performed two sets of simulations. In the first set, MCs have precollision Mach numbers of order unity while in the second set the precollision Mach number is greater than ten. In some cases the MCs are immersed in ICM. Periodic boundaries are in place and meant simply for ghosting particles at box edges. Due to the peculiar nature of our star formation code, DRAGON, we use a cubic periodic box even though a cuboid would be best suited. This particular choice imposes a considerable amount of additional computational expense, as most of the computational domain remains unutilised.

In the remaining cases, we simply use naked MCs. It is much simpler to set up the required initial conditions in this case. At the same time the number of gas particles in the clouds can be easily increased and therefore, the resolution.

4.2.1 The equation of state :

We make use of two different choices of the barotropic equation of state (EOS). Table (4.1) below provides the list of simulations performed with the relevant physical parameters adopted in a particular simulation and the corresponding choice of the EOS. The first choice of the EOS is

$$\left(\frac{T}{\mathrm{K}^\circ}\right) = \left(\frac{T_0}{\mathrm{K}^\circ}\right)\left[1 + \left(\frac{\rho}{10^{-14}\mathrm{g\ cm}^{-3}}\right)^{\gamma-1}\right], \tag{4.9}$$

where T_0 is the ambient temperature, ρ is the density and γ is the polytropic constant which, for the non - relativistic, monatomic gas is $\frac{5}{3}$. This EOS flips from being isothermal to adiabatic at $\rho = 10^{-14}$ g cm^{-3}. It is denoted as (EOS-B) in Table (4.1).

Equation (4.9) can be easily derived in the following manner. We begin by considering a spherical mass of gas having radius, R, volume, V, and pressure, P. If this mass is held at a uniform temperature, T_0, which is further assumed to behave like a perfect black body, then the amount of work done on it due to an infinitesimal change in its volume, dV, is

$$-PdV = a_0^2 \rho 4\pi R^2 dR.$$

Here a_0 is the isothermal sound speed, as defined by Equation (4.5). The time rate of change of the internal energy i.e. minus the luminosity is,

$$P\frac{dV}{dt} = a_0^2 \rho 4\pi R^2 \frac{dR}{dt}$$

$$= 3M_0 a_0^2 \cdot \frac{\dot{R}}{R}. \tag{4.10}$$

The luminosity L of a perfect black body is,

$$L = 4\pi R^2 \sigma_B T_0^4, \tag{4.11}$$

where σ_B is the Stefan - Boltzmann constant. For a non - ideal case, there is an efficiency factor associated with the luminosity, indicating how good a black body radiator a given mass of gas is. In the present case, since we have approximated the mass of gas as an ideal black body, this efficiency factor equals unity.

The gas remains approximately isothermal if,

$$L + p\frac{dV}{dt} \geq 0.$$

Neglecting the inequality, we get

$$4\pi R^2 \sigma_B T_0^4 + 3M_0 a_0^2 \frac{\dot{R}}{R} = 0$$

$$\sigma_B T_0^4 + a_0^2 \dot{R}\rho = 0.$$

Combining the expressions for gas pressure in the two regimes gives the general expression for gas pressure as,

$$p = a_0^2 \rho + K_1 \rho^\gamma, \tag{4.12}$$

where the first term corresponds to the isothermal regime and the second term corresponds to the adiabatic regime of the gas. Differentiating Equation (4.12) with respect to ρ we get,

$$\frac{dp}{d\rho} = a_0^2\Big(1 + \frac{K_1\gamma}{a_0^2}\rho^{\gamma-1}\Big) \tag{4.13}$$

Differentiating the polytropic pressure - density relation, $p = K_2\rho^\gamma$, with respect to ρ, we get

$$\frac{dp}{d\rho} = K_2\gamma\rho^{\gamma-1} = \frac{\gamma p}{\rho}.$$

Substituting this expression in Equation (4.13) we get,

$$\frac{\gamma P}{\rho} = a_0^2 + K_1\gamma\rho^{\gamma-1} \tag{4.14}$$

$$\Rightarrow \frac{\bar{m}_H \gamma P}{k_B \rho} = T_0 + T_0\Big(\frac{K_1\gamma}{a_0^2}\Big)\rho^{\gamma-1},$$

where we have simply made use of the definition of a_0^2. On the left hand side of the above expression we have the temperature, $T(\rho)$, and the quantity in brackets in the second term on the RHS is identified as $\rho_c^{1-\gamma}$, where ρ_c is the critical density. Making these substitutions, the above expression becomes

$$\Big(\frac{T}{K^\circ}\Big) = \Big(\frac{T_0}{K^\circ}\Big)\Big[1 + \Big(\frac{\rho}{\rho_c}\Big)^{\gamma-1}\Big],$$

as stated in Equation (4.9) above.

For the present purpose, we choose the critical density $\rho_c = 10^{-14}$g cm^{-3}. For $\rho \leq \rho_c$, $T \sim T_0$ while for $\rho > \rho_c$, the EOS becomes adiabatic and $\rho \propto T^{\frac{2}{3}}$, for a monatomic gas. The alternative form of the barotropic EOS we use here is,

$$\left(\frac{T}{\mathrm{K}^\circ}\right) = \left(\frac{T_0}{\mathrm{K}^\circ}\right)\left[(2.1 \times 10^{-19}) \cdot \left(\frac{\rho}{\mathrm{g\ cm^{-3}}}\right)^{-1} + 1 + (2.4 \times 10^{10}) \cdot \left(\frac{\rho}{\mathrm{g\ cm^{-3}}}\right)^{\frac{2}{3}}\right] \tag{4.15}$$

According to this EOS, initially the temperature (T) decreases as ρ^{-1} up to $\rho \sim 10^{-19}$ g cm^{-3}, then remains constant at $\sim$10 K in the range $\rho \in (10^{-19}, 10^{-15})$ g cm^{-3} and finally as the density increases beyond $\sim 10^{-15}$g cm^{-3}, this EOS mimics Equation (4.9). Thus, the EOS has three regions in the $T - \rho$ space as can be seen from Fig. (4.5), and each region is marked by numbers 1, 2 and 3, respectively. The first region is dominated by radiative cooling, the second (flat) region is where approximate isothermality is maintained and the third corresponds to adiabatic heating. A detailed derivation of this EOS can be found in Low & Lynden - Bell (1976). In Table (4.1) below, this EOS is denoted as (EOS-mod).

With this choice of the EOS, the precollision clouds start at the top of region 1 in Figure (4.5) and then subsequently slide down along the $\log(T) - \log(\rho)$ characteristic. Post-collision, a dense shock compressed layer is formed. For a strongly radiating shock, the slab is approximately isothermal. Regions in the slab which are dense enough, have temperatures $\sim$10 K as can be seen from Figure (4.5). Radiative cooling takes place through a variety of mechanisms. Molecular line emission, recombination line emission, collisional emission, collisional excitation of dust grains, corrosion of dust grains or grain - grain collisions (also called dust sputtering), are the dominant mechanisms.

The contribution from individual cooling mechanisms depends on the strength of the shock which in turn depends on the precollision velocity of the clouds. For instance, in case of highly supersonic cloud collision, with individual clouds moving at a few tens of km s^{-1}, there could be significant ionization of atomic hydrogen (Kaplan 1966). Using the Rankine - Hugoniot jump conditions it can be shown that,

$$\frac{\rho_2}{\rho_1} = \frac{(\gamma+1)\left(\frac{P_2}{P_1}\right) + (\gamma-1)}{(\gamma-1)\left(\frac{P_2}{P_1}\right) + (\gamma+1)} \tag{4.16}$$

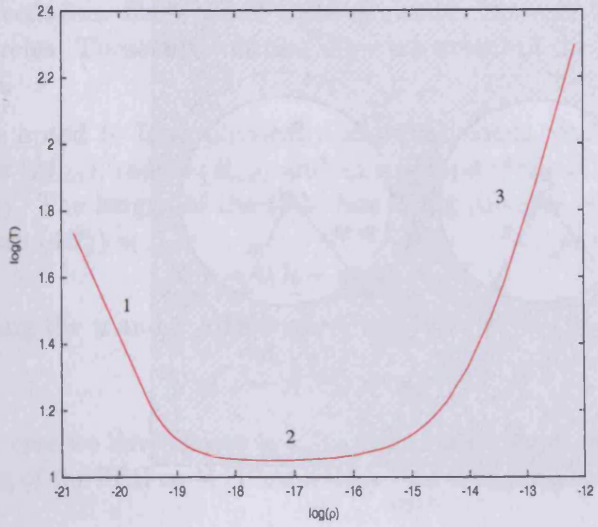

Figure 4.5: The $\log(T) - \log(\rho)$ space for the new EOS in experiment 5 (see Table (4.1) below). Temperature (T) measured in degree Kelvin and density (ρ) in g cm^{-3}.

The subscripts '2' & '1' refer respectively, to the post-shock and preshock quantities. For strong shocks $\left(\frac{P_2}{P_1}\right) \rightarrow \infty$, so that in this limit it follows from Equation (4.16) that, $\frac{\rho_2}{\rho_1} \rightarrow \left(\frac{\gamma+1}{\gamma-1}\right)$. For a monatomic ideal gas, $\gamma = \frac{5}{3}$, so that $\left(\frac{\rho_2}{\rho_1} \rightarrow 4\right)$. Also, the ratio of post shock temperature to the preshock temperature is,

$$\frac{T_2}{T_1} = \frac{[2\gamma M_1^2 - (\gamma - 1)][(\gamma - 1)M_1^2 + 2]}{(\gamma + 1)^2 M_1^2}, \tag{4.17}$$

where M_1 is the preshock Mach number. It can be easily seen that $\frac{T_2}{T_1} \rightarrow \infty$ as $M_1 \rightarrow \infty$. The respective derivations of Equations (4.16) & (4.17) can be found in Stahler & Palla (2005), Appendix F. In case of strong shocks, the molecular bonds are readily disrupted and produce component atoms, which in turn may be ionised if the ambient temperature is sufficiently high. Depending on the ambient conditions many, if not all the radiative cooling mechanisms mentioned above, could play a significant role. In the simulations presented here, post-shock cooling is only approximately incorporated, and a detailed treatment of molecular cooling is necessary (e.g. Koyama &

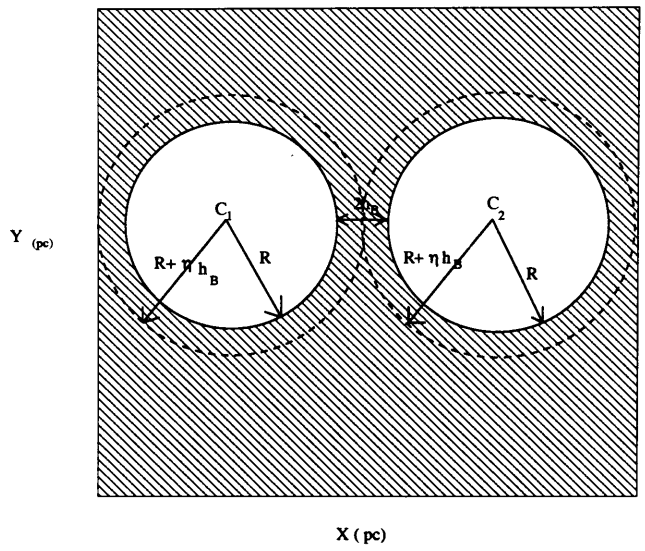

Figure 4.6: Schematic diagram of the initial set up of colliding clouds. For description see text below.

Inutsuka 2000). Radiative cooling dominates as long as gas in the shock front is optically thin. It is only in this regime that approximately isothermal conditions are maintained. Once the gas becomes optically thick, the radiation is trapped in the gas slab.

Equation (4.17) also shows that the post shock temperature changes by very little in case of weak shocks. They are however, not strictly adiabatic as there is increase in entropy across the shock front. In such cases, the EOS spans only the regions 2 and 3 shown in Figure (4.6).

4.2.2 Setting up the initial conditions :

We have already described the scheme for assembling the MCs in §4.1. The box of ICM particles is set up in a manner similar to the envelope of P_{ext} particles for the isothermal spheres. The box dimensions are so set that each cloud has an envelope of thickness, ηh_B.

Figure (4.7) shows a schematic diagram of the initial set up. This is a two dimensional picture showing MCs barely touching each other prior to their collision. The circles drawn by continuous lines represent the individual

clouds before collision. Each one of these circles is circumscribed by respective dashed circles. These latter circles show the extent of the ICM envelope for each cloud.

Since we have opted to have physically identical clouds, each of them has the same mass (M_{cld}), radius (R_{cld}) and an envelope of the ICM particles of thickness, ηh_B. The length of the ICM box along the axis of collision (the x axis in Figure (4.7)) is

$$x = 4(R + \eta h_B),$$

while that along the y and z axes respectively, is

$$y = z = 2(R + \eta h_B).$$

In the present case we have chosen $\eta = 3$. As has been mentioned previously, a short coming of the SPH code DRAGON is that it requires a cubic periodic box.

Each side of the cubic box therefore has length x pc, as obtained from the first of the two expressions above. Let N_{SPH1} and N_{SPH2} be the maximum number of gas particles in each cloud. Then following the procedure described above for setting up the envelope of ICM particles around a cloud; we calculate the the respective number of particles to be assembled in individual ICM envelopes, N_{env1}&N_{env2}. If N_{Box} is the total number of particles (ICM + GAS) in the box then,

$$N_{Box} = (N_{SPH1} + N_{SPH2} + N_{env1} + N_{env2}) + N_{empty}, \tag{4.18}$$

where N_{empty} is the number of ICM particles in the empty region of the box, marked by stripes in Figure (4.7). The volume of each cloud - envelope combine is

$$V_{SPH1+env1} = \frac{4}{3}\pi(R + \eta h_B)^3 = V_{SPH2+env2}. \tag{4.19}$$

The volume of this cubic box is

$$V_{Box} = 64(R + \eta h_B)^3. \tag{4.20}$$

Thus, the volume of the empty region is,

$$V_{empty} = V_{Box} - (V_{SPH1+env1} + V_{SPH2+env2}).$$

We know the required number density, $\hat{n}_B$, of particles across the boundary between the gas and ICM particles. Thus,

$$N_{empty} = V_{empty} \cdot \hat{n}_B. \tag{4.21}$$

From Equation (4.29) we obtain the total number of particles to be assembled in the box. Once this number is known, the particles are assembled in a hexagonal closed packed (HCP) lattice, since it provides the highest packing fraction.

After assembling particles in the box, it is suitably evolved to form a glass. Particles within the desired cloud radius are then scooped out and replaced with corresponding gas particles. This process is then repeated for the other cloud. With this, the process of setting up the initial conditions is completed.

4.2.3 Experiments with colliding clouds :

Various cloud collision experiments performed here have been listed in Table (4.1). Column 1 is the serial number of an experiment. Column 2 provides various physical details of individual clouds used in a particular simulation. We choose the mass of a cloud (M_{cld}) arbitrarily while the corresponding cloud radius (R_{cld}) is determined using Larson's scaling relation between the mass and radius of a cloud,

$$R_{cld}(\mathrm{pc}) = 0.1\mathrm{pc}\Big(\frac{M_{cld}}{\mathrm{M}_{\odot}}\Big)^{0.5}. \tag{4.22}$$

The temperature within the cloud is determined using Equations (4.2) and (4.5). The third column indicates whether, in a particular simulation, external pressure (P_{ext}) i.e. ICM particles are used. The fourth column gives the pre - collision Mach number of each cloud. The fifth column indicates separately, the total number of particles (ICM+GAS) used and the number of gas particles. The sixth column indicates whether the clouds were incident head - on or at a non - zero impact parameter. Finally, the seventh column indicates the choice of EOS used in a particular numerical experiment.

The discussion of the results of these simulations is deferred to the next chapter. Before that, I would like to briefly dwell on sink particles in SPH.

4.2.4 Sink particles :

Candidate protostellar objects in SPH simulations are treated by using a special type of particle called sink. However, sinks are not unique to SPH only and have been employed in finite difference codes as well (Boss & Black, 1982). They were first introduced in SPH by Bate *et al* (1995).

Table 4.1: Details of simulations performed.

Serial No.	Experimental details	P_{ext}	Precollision Mach number	Number of particles	Head on	EOS used
1	$M_{cld1} = M_{cld2} = 100M_{\odot}$ $R_{cld1} = R_{cld2} = 1$ pc T = 84K	Yes	10	$N_{tot} = 34893$ $N_{gas} = 3516$	Yes	EOS-B
2	$M_{cld1} = M_{cld2} = 50M_{\odot}$ $R_{cld1} = R_{cld2} = 0.8$ pc T = 54K	Yes	1	$N_{tot} = 34893$ $N_{gas} = 3516$	Yes	EOS-B
3	$M_{cld1} = M_{cld2} = 150M_{\odot}$ $R_{cld1} = R_{cld2} = 1.22$ pc T = 104K	Yes	35	$N_{tot} = 401569$ $N_{gas} = 40000$	Yes	EOS-MOD
4	$M_{cld1} = M_{cld2} = 50M_{\odot}$ $R_{cld1} = R_{cld2} = 0.8$ pc T = 54K	Yes	12	$N_{tot} = 129427$ $N_{gas} = 16000$	Yes	EOS-MOD
5	$M_{cld1} = M_{cld2} = 50M_{\odot}$ $R_{cld1} = R_{cld2} = 0.8$ pc T = 54K	No	12	$N_{gas} = 40000$	No	EOS-MOD
6	$M_{cld1} = M_{cld2} = 50M_{\odot}$ $R_{cld1} = R_{cld2} = 0.8$ pc T = 54K	No	12	$N_{gas} = 100000$	Yes	EOS-MOD
7	$M_{cld1} = M_{cld2} = 400M_{\odot}$ $R_{cld1} = R_{cld2} = 2.0$ pc T = 170K	No	13	$N_{gas} = 100000$	Yes	EOS-MOD
8	$M_{cld1} = M_{cld2} = 50M_{\odot}$ $R_{cld1} = R_{cld2} = 0.8$ pc T = 54K	No	03	$N_{gas} = 100000$	Yes	EOS-MOD

As discussed in §3.4.1, when the density in a certain region of the computational domain starts increasing, then as a direct consequence of the time stepping equations, the time step becomes progressively smaller. The problem becomes chronic when condensations proceed towards stellar densities. This is also one of the reasons for the unsatisfactory nature of the global time stepping scheme. This situation is unacceptable since the exercise then becomes computationally unfeasible. Hence an alternative is required to tackle these high density particles and track their further evolution. Apart from the use of sinks, there are two alternatives. The first is to use a fixed minimum smoothing length and the second is to use a polytropic EOS above a certain density threshold.

In using a fixed smoothing length, the idea is to essentially replace the prevalent EOS by one where particles with the highest densities are treated as incompressible gas. Their separations are not allowed to decrease below a certain limit (Bonnell *et al*, 1991). The second option, that of using the polytropic EOS at such high densities is the same as invoking Equation (4.20). It permits us to follow the collapse further, since temperature increases rapidly with rising density and the resulting thermal support inhibits further collapse of high density condensations. Thus the smoothing length is allowed to decrease, only for the highest density particles, while the change remains invisible for other particles. However, either of the two schemes are unsatisfactory due to the computational expense they incur and the calculations become slower as more and more particles attain high densities.

To overcome such problems, the idea of replacing an extremely dense agglomeration of particles by a sink particle was proposed by Bate *et al* (1995). The sink interacts with the remaining SPH particles only through gravity. Since SPH is a Lagrangian scheme, such replacement can be easily implemented. However, particles being accreted by a sink need to pass certain criteria. Sinks are characterised by two parameters viz. the sink density (ρ_{sink}) and the sink radius (R_{sink}). These are predefined quantities in a simulation. Only the particles within this radius are accreted. In the current work, protostellar objects are modelled using sink particles.

However, R_{sink} cannot be chosen arbitrarily since, with too small a sink radius the neighbourhood of a sink particle will be hardly cleared and the advantage associated with the inception of such a particle may not materialise. On the other hand, too large a choice of R_{sink} will just increase the accretion radius leading to rapid loss of gas particles. It is therefore essential to make an optimal choice of R_{sink}. In all our simulations, the sink density

is held fixed at $\rho_{sink} = 10^{-12}$g cm^{-3}. R_{sink} is then so chosen that the initial sink mass, M_{sink}, is comparable to the minimum resolvable mass, M_{min}, in the simulation. Thus,

$$M_{min} = N_{neibs} \cdot m_i,$$

where

$$m_i = \frac{M_{cld}}{N_{SPH1}}.$$

Then, the requirement that $M_{min} \sim M_{sink}$,

$$\Rightarrow R_{sink} \sim \left(\frac{M_{min}}{4\rho_{sink}}\right)^{\frac{1}{3}}$$

$$= \left(\frac{N_{neibs} M_{cld}}{4 N_{SPH1} \rho_{sink}}\right)^{\frac{1}{3}}. \tag{4.23}$$

Once this parameter is set in a simulation, it remains fixed.

As mentioned previously, particles being accreted by the sink particle need to satisfy certain criteria. Firstly, these particles need to be gravitationally bound to the sink particle. In other words, the velocity of that particle, about the sink particle must be less than that required for an orbit of radius, R_{sink}, about the sink. Secondly, in case two sinks are located in very close vicinity of each other as in the case of tight binaries, particles are accreted by the one to which they are more tightly bound. However, if the two sinks have unequal masses then the gas particles may pass through the region between the two sinks, and eventually be accreted by the heavier one.

To avoid catastrophic acceleration of infalling particles, the sink may be characterised by a second accretion radius, much smaller than R_{sink}. Conventionally it is selected ten to a hundred times smaller than R_{sink} and particles coming within this radius are directly accreted without investigation into any criteria laid above. Alternatively, the sink potential can be softened . Our SFC employs this later technique. In our SFC there is also an additional criterion to avoid formation of two sinks in close proximity i.e. within $2h$ of one another.

Finally, let us see how a sink particle is introduced in SPH simulations. When collapsing clumps reach sufficiently high densities then, as soon as the density of a particle exceeds ρ_{sink}, it is replaced by a sink particle. The prospective sink particle must satisfy the following conditions -

(1) The candidate sink particle must have at least fifty neighbours (fifty is considered a reasonable choice for the number of neighbours of a SPH

particle). This is generally ensured by checking that the smoothing length of this particle is half R_{sink}.

(2) The clump is actually collapsing. In other words, the ratio of thermal to gravitational energy (see Equation (2.49)) is less than/equal to 0.5. The sum of this ratio with the ratio of rotational to gravitational energy, must be less than/equal to unity. Note that we take only the magnitudes of the respective ratios.

(3) The particles being accreted by the prospective sink must be gravitationally bound to it.

(4) Finally, it is also essential to check that the neighbours of the candidate sink particle do not have net accelerations away from each other, in which case the candidate sink particle will be tidally disrupted (Price *et al*, 1995; Bate *et al*, 1995).

Apart from these qualifying criteria, Bate *et al* (1995) also suggest some boundary conditions for sink particles and some correction terms to the sink potential. These latter corrections are meant to compensate for the replacement of the actual sink potential by the potential of a point mass. The contribution of these correction terms to the actual potential, is usually very small. Our SFC accounts for these corrections. Forces acting on a sink particle also require correction since a sink particle may not be able to find enough neighbours. This is very similar to the problem discussed in §3.1.3, where it was pointed out that deficiency of neighbours could lead to underestimation of SPH density. This is critical in case of sinks since the resulting imbalance in forces could lead spurious effects due to large pressure gradients, and particles may rain in on the sink with incredibly high velocities.

Our SFC does not include the BCs mentioned above due to which, an explicit discussion about them is avoided here. The simulations therefore, to some extent, are corrupted on this account. However, no catastrophic behaviour is witnessed in any of those recorded here.

Chapter 5

Fragmentation Of Approximately Isothermal Shocked Gas Slab

In the previous chapter I described the procedure for setting up the initial conditions for the colliding clouds experiment and listed the models tested, see Table (4.1). Below, I start with a brief review of the history of this problem, which will prepare the necessary background to discuss the findings of our numerical experiments. The models tested here, can be broadly classified into two types viz. the highly supersonic and moderately supersonic cloud collisions, with individual clouds having precollision Mach numbers greater than ten and of order unity, respectively. It is essential to distinguish between the two velocity regimes since the post - collision evolution of the resulting gas slab is remarkably different, from each other.

5.1 Setting up the background :

We reviewed the physical properties of GMCs in §2.1 above, where it was noted that GMCs exhibit random motion apart from their systematic orbital motion in the galactic arms. The mean free path for collision of GMCs is of order a few tens of parsecs and with a velocity dispersion of a few km s^{-1}, there must be a collision between GMCs on the scale of a few million years. This is about an order of magnitude smaller than the galactic timescale so that on average, a GMC will suffer a few tens of collisions during a single

galactic rotation. The problem of cloud collision therefore, is significantly important and demands investigation. Here we seek to know the influence of these events on structure formation in the ICM.

GMC collision is a violent phenomenon which might spawn star formation in the resulting composite object. Magnetic fields threading galactic arms modulate cloud velocities, which in turn reduce the post - collision energy dissipation. Cloud collisions are more violent and dissipative in the presence of a weak ambient magnetic field, and less dissipative when the magnetic field is strong and roughly parallel to the spiral galactic arm. Pikelner (1957) used the shock jump conditions to calculate the change in entropy across the shock front and showed that the energy dissipated in the latter case (strong ambient magnetic field) is $\sim 3^{\frac{3}{2}}$ times smaller than that in the former. See Spitzer (1968) for a more thorough discussion of the ICM.

Cloud collision and structure formation :

Spiral shock waves sweep up matter in galactic arms and produce large scale structure and dust lanes (Roberts, 1969; Fleck, 1992; Heitsch *et al*, 2006; Elmegreen, 2007). Often MCs themselves are filamentary and such clouds, presumably form out of gravitationally unstable gas sheets (Nagai, Inutsuka & Koyama, 1998).

Schneider & Elmegreen (1979) performed one of the first studies of large scale filamentary structures in the local neighbourhood. Now with improved observational technology it is possible to map MCs in greater detail. For instance, dense filamentary structures have been observed in the Perseus region where there is evidence for ongoing star formation (Hatchell *et al*, 2005). The Orion Integral Filament (OIF) in the Orion A region has been studied in detail and a number of Young Stellar Objects (YSOs) have been reported to be embedded in it (Chini *et al*, 1997; Johnstone & Bally, 1999).

Structure within MCs appears to be hierarchical and the densest regions are gravitationally bound, see for instance (Larson, 1981; Elmegreen, 2007). Turbulence within MCs decays rather quickly, on a timescale equal to the dynamical period of evolution of the cloud. Internal turbulence leads to dynamic interaction between fluid flows. This is one possible mechanism for structure formation in MCs (Klessen & Burkert, 2000; McLow & Klessen, 2004). Gas slabs resulting from collision of stellar winds from early type binary systems expanding at supersonic speeds become thermally unstable due to rapid cooling, also turbulent motion within shells makes them unstable to shearing instabilities (Stevens *et al*, 1992).

Similarly, powerful ionising radiation emitted by young OB associations or supernova remnants sweeps up gas and forms a dense shell that is gravitationally and thermally unstable (e.g. Strickland & Blondin, 1995; Dale, Clark & Bonnell, 2007; Dale, Bonnell & Whitworth, 2007). Low velocity MC collision on the other hand, produces a gravitationally unstable gas slab (Chapman *et al*, 1992; Bhattal *et al*, 1998). The gas bodies resulting from dynamically interacting fluid masses already contain the necessary seeds of instabilities. Sufficiently dense regions in the density structures collapse under self gravity.

It is an observationally established fact that stars form in clusters and N-body dynamics of clusters have enabled us to estimate various physical properties of multiple systems like orbital eccentricities and stability, multiplicity of stellar systems and stellar masses. Star clusters have reasonably homogeneous environs and constant metallicity. Thus, they are useful regions for star formation studies (Clark, Bonnell, Hillenbrand, 2000). However, in regions like the Orion Integral Filament (OIF) the sub mm sources detected, do not seem to exhibit multiplicity (e.g. Chini *et al*, 1997).

Star clusters however, show a wide variation in stellar density. For instance, Meyer & Lada (1999) discuss this difference in case of the Orion Molecular Cloud. They claim that $\sim$96 percent of the IR sources in the Orion B region are located in clusters, while in the Orion A region, only about 50 to 80 percent of the stellar population is formed in clusters. These regions were also recently studied by Nutter & Ward-Thompson (2007), who revisit the point about high stellar densities in these regions. They refer to the possible effect of stellar density on the slope of the IMF and the star formation efficiency (SFE). Further, they suggest a three part power law for these regions with a much lower turnover mass, $\sim$0.08 $M_{\odot}$. A high stellar density suggests a higher SFE compared to regions devoid of stars.

It is essential to investigate the various physical processes leading to clump formation. The gravitational fragmentation of clumps leading to the formation of protostellar cores, is the next step in the star formation history. Stars condense out of the protostellar cores so formed (e.g. Hoyle, 1953; Whitworth *et al*, 1996). Various possible mechanisms for clump formation have been suggested. The dynamical turbulence model is a possible mechanism to explain the clump formation within molecular clouds (Klessen, Burkert & Bate, 1998; Klessen & Burkert, 2000). The other model suggested is that of gravitational fragmentation of an external pressure confined slab, a subject that has been under sustained debate. See for e.g. Elmegreen & Elmegreen

(1978); Clark (1999); Whitworth *et al* (1994) and Boyd & Whitworth (2005). In particular, Chapman *et al* (1992) examined off-centre cloud collisions and showed that the resulting pressure compressed slab underwent gravitational fragmentation. These collapsing fragments then produced binary and higher multiple systems.

In the present investigation, we attempt to distinguish between the evolution of an isothermal slab confined by external shock and isotropic, external pressure. We examine the relative importance of shearing instabilities in comparison to gravitational instability, in both type of slabs.

Previous numerical investigations :

The problem of colliding clouds has been studied numerically in the past by Stone (1970, a & b), Hausman (1981), Lattanzio *et al* (1985), Hunter & Klein (1986), more recently by Stevens *et al* (1992) who studied colliding winds in early type binary systems, Whitworth *et al* (1994), Whitworth *et al* (1995) and Klien & Woods (1998) among others. Stone (1970, a) studied the problem in one dimension by simulating clouds as planes having infinite extent and found that post-collision, the clouds coalesced. The resultant composite object then re-expanded. This experiment was repeated in two dimensions and the same observation was made (Stone, 1970 b). Hausman (1981) performed particle simulations of head-on and off-centre cloud collisions. However, their results were corrupted due to particle penetration during collision.

Later Hunter & Klein (1986), in their grid simulation of colliding flows found that such collisions produced slabs that were unstable to Rayleigh-Taylor (RT) like instability, however they could not establish the exact nature of the instability observed in their simulation. A similar conclusion was drawn by Stevens *et al* (1992) and Klein & Woods (1998). They also found evidence for non linear growth of instabilities starting in thin shells. Klein & Woods (1998) further found that, as the non-linear instability evolved and went into saturation, the slab collapsed and formed a thin, long filament along the axis of collision.

The plan of the chapter is as follows. In §5.2, I will review a few previous studies of the cold, isothermal gas slab followed by a discussion of the NTSI. Next, in §5.2.1, I shall discuss the observations from our simulations in §5.3 and then conclude in §5.4. I discuss the gravitational instability separately, in context of each simulation.

5.2 The cold isothermal slab :

Historically the problem of gravitational fragmentation of a uniform gas slab of infinite extent was first studied by Jeans. His pioneering work showed that, in the absence of gravitational forces perturbations in the density field propagate like sound waves. He pointed out that self gravity reduces the elasticity of the medium and the gravitational instability grows exponentially.

If k and ω are respectively, the wave number and angular frequency of the gravitational instability, then the dispersion relation connecting the two, is

$$\omega^2 = k^2 a_0^2 - 4\pi G\rho_0, \tag{5.1}$$

where a_0 is the local sound speed, $a = \left(\frac{dp}{d\rho}\right)_0^{\frac{1}{2}}$ and ρ_0 is the initial unperturbed density.

When $k > k_J = \left(\frac{4\pi G\rho_0}{a^2}\right)^{\frac{1}{2}}$, the perturbation propagates as gravitationally modified sound waves. On the other hand for $k < k_J$, ω becomes imaginary and the perturbation grows on the time scale,

$$\frac{1}{\omega} = \frac{(4\pi G\rho_0)^{\frac{-1}{2}}}{[1 - \left(\frac{k}{k_J}\right)^2]^{\frac{1}{2}}}. \tag{5.2}$$

Equation (5.2) gives the time scale for amplification of the perturbation and in the limit $k \to k_J$, the timescale becomes infinite while in the limit $k \to 0$, it reduces to $(4\pi G\rho_0)^{\frac{-1}{2}}$. Thus, we can define the minimum wavelength called the Jean's length as,

$$\lambda_J = \frac{\pi}{k_J} = \left(\frac{\pi a^2}{4G\rho_0}\right)^{\frac{1}{2}}. \tag{5.3}$$

See Mestel (1965) for a detailed review of this problem. The growth of unstable modes in cold isothermal slabs has been studied by Ledoux (1951), Chandrasekar (1953), Chandrasekar (1962) and Simon (1965) among others. Ledoux (1951), in his study of a self gravitating, stratified isothermal gas slab found the existence of a marginal mode ($\omega^2 = 0$) and the slab became unstable to perturbations travelling in the plane of the slab with wavelengths greater than a finite critical length, of order the effective slab height. This wavelength is comparable with the Jeans length calculated for the prevailing physical conditions of the slab.

Simon (1965) confirmed these findings and additionally found another unstable mode at k^2 = 0.20 and ω^2 = -0.44. All of these studies however, were confined to gas slabs without any external forces on them . Elmegreen & Elmegreen (1978) performed a perturbative analysis to study the growth of gravitational instability in a shock compressed isothermal slab. However, they did not employ explicit jump conditions and approximated non-isotropic ram pressure simply as external pressure. Their study showed that the minimum mass of a fragment condensing out of such a slab increased with the age of the shock. They also showed that the size of this fragment was proportional to the wavelength, λ, of the fastest growing unstable mode,

$$\lambda \sim \frac{2\pi H}{\nu},$$

where H is the scale height defined as, $H = a_0(2\pi G\rho_0)^{-1/2}$ and $\nu = kH$. Objects of this size were thought to collapse under self gravity and form spherical objects i.e. Bonnor-Ebert spheres. Later Whitworth *et al* (1994), with a similar analysis, obtained expressions for order of magnitude estimates of the separation between the fragments and the time scale for this condensation process.

Vishniac (1983) analysed the problem by invoking full shock conditions and found evidence for the bending modes of the slab. His linear analysis of the growth of these bending instabilities suggested that the instability leads to the disintegration of the shock compressed slab, only after which gravitational clustering commences. This investigation was further extended by Vishniac (1994) to the non-linear regime, to study bending as well as breathing modes of the shock compressed slab.

This latter analysis, showed that such slabs become unstable to the non linear growth of shearing instabilities. Since this instability commences in thin shells (i.e. between layers of the slab), it is called the Non-linear Thin Shell Instability (NTSI). The NTSI grows rapidly and eventually saturates. It causes strong mixing between slab layers and eventually, the slab forms a sieve like structure and collapses under self gravity to form a filament with a large aspect ratio. Gravitational clustering can then occur in this filament.

5.2.1 The NTSI :

The problem under investigation here is that of the evolution of a viscous fluid slab, confined by accretion shocks on either sides. The physical condition under which the NTSI is observed has been discussed above. Let us

now look at the mechanism responsible for this instability. Consider a slab of infinite extent, parallel to the y axis, x being the collision axis, $(x_1, 0)$, and $(x_2, 0)$ being the coordinates of its edges and a_0 is the isothermal sound speed within the slab.

Let $\hat{\mathbf{i}}$ and $\hat{\mathbf{j}}$ be the unit vectors along the x and y axes respectively and ρ_{ext} be the density of the external gas streaming in at supersonic speed towards this slab. To put this in context with our cloud collision experiments, the slab corresponds to the initial contact discontinuity formed between the colliding clouds, immediately after they touch each other. Subsequently this layer accretes material from the individual collapsing clouds.

Let $\pm V_{ext}\hat{\mathbf{i}}$ be the velocity of the gas streaming in towards the slab. The $(\pm)$ corresponds to the material flowing upstream/downstream, relative to the shocked slab. The shock travels at speed V_s relative to the gas streaming in with speed $-V_{ext}$. The two are related by the following expression,[1]

$$V_{ext} = V_s - \frac{a_0^2}{V_s}.$$

The schematic diagram of the shocked slab is shown in Figure (5.1) below. It shows gas with density ρ_{ext} and velocity V_{ext} streaming in towards the slab along the $(\pm)\hat{\mathbf{i}}$ directions. The bending mode of the slab due to the initial perturbation is also shown. From the conservation of mass $(\rho_s(V_s - V_{ext}) = \rho_{ext}V_s)$, it follows that the post shock density, $\rho_s = \rho_{ext}\frac{V_s^2}{a_0^2}$. The incoming gas at the point P moves up the slab while that coming in at the point Q moves down the slab, as indicated by the arrows. There is no net flow of material across the slab, but a net transport of momentum from the normal, $\hat{\mathbf{i}}$, to the transverse, $\hat{\mathbf{j}}$, direction.

Material moving up the slab deposits a net positive momentum and that moving down the slab deposits a net negative momentum in the perturbed regions of the slab. The resulting effects are non-linear leading to amplification of the transverse bending modes of the slab. Eventually these modes

[1]The Rankine-Hugoniot jump conditions for a shock are,

$$[\rho v^2 + p]_S = 0$$

and

$$[\rho v]_S = 0.$$

(The energy jump condition has not been quoted here as it is not required at this point.) Combining the two expressions we get, $V_{ext} = V_s - \frac{a_0^2}{V_s}$.

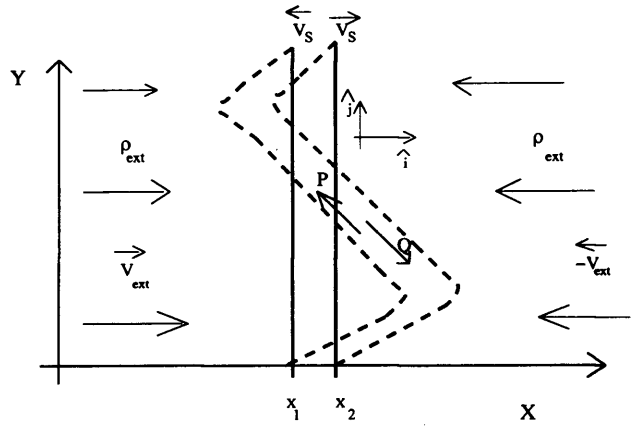

Figure 5.1: Shock compressed slab in the xy plane. The sinusoidal displacement of the slab i.e. its bending mode, and material having density ρ_{ext} and speed V_{ext}, being accreted by this slab has also been shown.

become greater than the thickness of the slab. An important point to be noted is that the internal pressure of the slab is thermal and isotropic while the external one is ram pressure. In the unperturbed state the distinction between the nature of the two forces is irrelevant.

Once there is a ripple (perturbation) on the slab, the internal pressure pushes the slab in the direction of the displacement (i.e along the x axis in Figure (5.1)). The external pressure, to first order, has no component in this direction and the slab experiences a unbalanced tangential force which is proportional to the bending angle of the slab and, tends to suppress slab oscillations. At the same time, there is net convergence of the accreted material in the convex regions of the slab, and divergence in the concave regions.

Strong shear causes turbulent mixing of the layers within the slab. That, indeed there exists strong shear between the post-collision slab layers, will be shown to be true in the discussion of individual simulations in the following section. τ, the dynamical timescale of this slab is the period over which the dynamical properties of the slab evolve. If τ is much smaller than the time available for the next similar layer to be generated at a distance greater than the wavelength and having wave number, k, then turbulent mixing is expected. For a slab of thickness L and age t, this condition is then given

by,

$$\tau \ll \frac{t}{kL}, \tag{5.4}$$

(Vishniac, 1994).

The turbulent mixing in the shocked slab is marginal if $t \gg \tau$. However, this large scale turbulent motion within the shocked slab gives rise to eddies on the scale of slab thickness. In the limit of a small bending angle, linear treatment is sufficient to predict the growth of the instability (Vishniac, 1983). The linear theory breaks down when the slab velocities are comparable to the local sound speed and the fluctuations in the column densities are of order unity. Further evolution of the instability becomes non-linear and the dynamic growth rate of the instability is then given by,

$$\tau^{-1} \sim a_0 k (k x_m)^{1/2} \cdot C_d^{-1/2}, \tag{5.5}$$

(Vishniac, 1994). Here x_m denotes the mid plane of the slab and C_d is a constant of order unity and describes the extent of dissipation resulting from mixing layers. Klein & Woods (1998) estimate $2 \lesssim C_d \lesssim 4$.

Once the NTSI sets in, it grows rapidly and saturates at a rate greater than $a_0 k (kL)^{1/2}$. Linear analysis by Vishniac (1983) suggested that, in the linear regime the thin shell instability leads to the fragmentation of the shock front. The resulting fragments are gradually eroded due to the RT instability. However, as the instability evolves towards saturation, it dissipates thermal energy. As a result the shocked slab loses its thermal support and collapses under gravity forming a thin filament.

5.3 An overview of the simulations :

We had set out by hypothesising that the isothermal, pressure compressed slab evolves in a remarkably different manner as compared to the isothermal, shocked slab. To establish our hypothesis set above, we start by discussing a simulation from each regime. We shall first discuss a high velocity head-on cloud collision model, specifically model 4. Next, we discuss a high velocity off-centre cloud collision case (model 5) and finally, a low velocity head-on cloud collision case (model 8). The reader is referred to Table (4.1) above (p. 85) for the relevant physical details of the respective models.

For ease of referencing, I shall hereafter refer models 4, 5, and 8 as cases **I**, **II**, and **III** respectively. All the column density plots presented in this

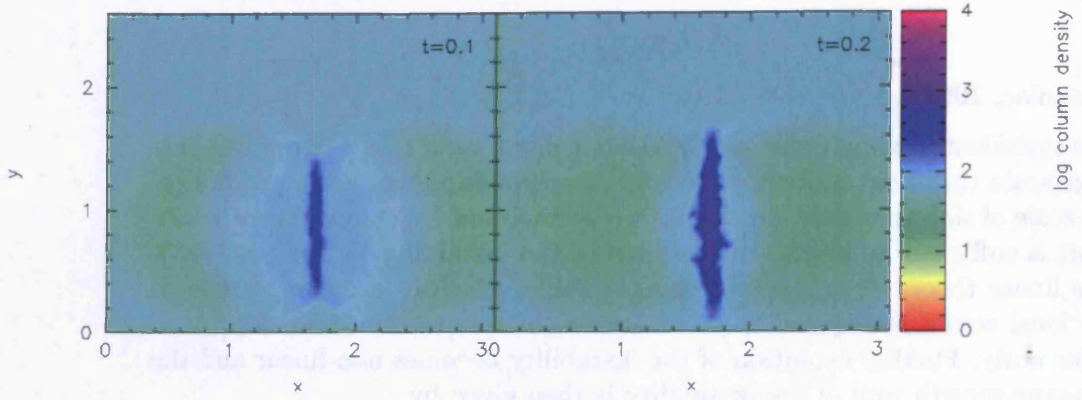

Figure 5.2: Sequence in time (Myrs) of colliding clouds in Model 4. See text for description.

work are plotted in the x-y plane, x being the axis of collision. The distance is measured in parsecs and a logarithmic scale has been adopted for the column density as it spans a wide range of magnitudes.

5.3.1 Case I (High velocity head-on collision):

When the colliding clouds first touch each other, they form a contact discontinuity. Subsequently, individual clouds collapse and form a shock compressed slab. The time required for the collapse of a cloud is called the cloud crushing time, t_{cr} (Klein & Woods, 1998).

After the formation of the initial shock front, the shock wave propagates through the cloud and reaches the far edge, in a time $t_{cr} \sim \frac{2R_{cld}}{v_s}$, where R_{cld} is the cloud radius and v_s is the velocity of the shock wave. The preshock velocity and density are known, using which the post - shock density can be estimated using Equation (4.16).

Snapshots in Fig. (5.2) show the collision between clouds and the formation of a shocked slab. The slab then develops a kink on it (the bending of the slab). This can be seen in the picture on the right hand side of Fig. (5.2) (t = 0.2 Myr). Soon after the formation of the shocked slab, we observe structure formation on its surface as can be seen in Fig. (5.3). Structure formation is the result of various breathing modes of the slab. With the

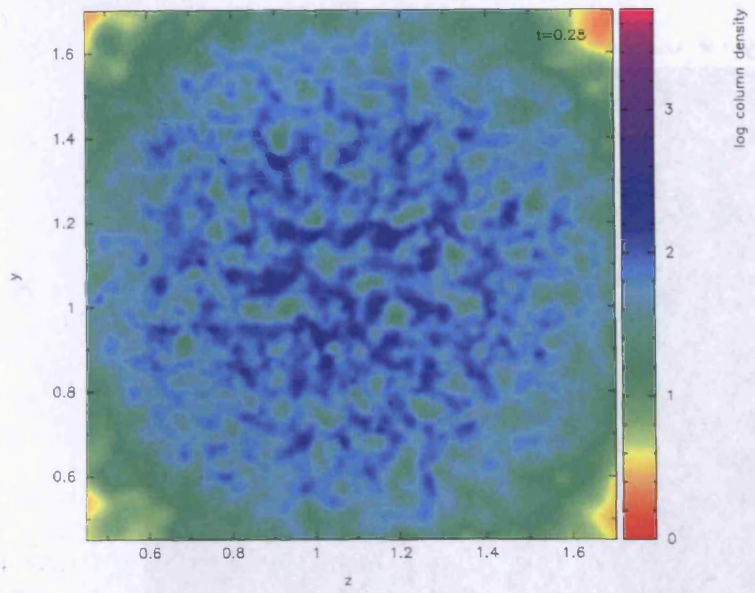

Figure 5.3: A close view of the shocked slab shortly after its formation, in model 4. It shows a network of filaments and denser regions where filaments intersect.

help of linear perturbation analysis, it can also be shown that shearing fluid layers develop surface gravity waves, which give it a rippled appearance. These are the breathing modes of that surface. An analogous situation is the formation of ripples on the surface of water due to breeze blowing over its surface (Raichaudhari, 1999).

Dense clumps form in regions where the filaments merge. The clumps have an average density of $\sim 10^{-18}$ g cm^{-3} but do not undergo gravitational collapse as they either suffer tidal rupture or merge with other clumps to form larger clumps. Fig. (5.4) shows the velocity field within the shocked slab. We defer the discussion of the effect of the turbulent velocity field and shearing instabilities on the evolution of the shocked slab, to the following subsection.

As the slab grows older, it disintegrates and collapses under self gravity to form a thin filament with a large aspect ratio, along the axis of collision. The pictures at time t=0.5 Myr, 0.75 Myr, and 1.0 Myr respectively show the collapsing slab, while formation of the filament can be seen in the bottom panel of Fig. (5.5). Gravitational clustering occurs in the filament so formed

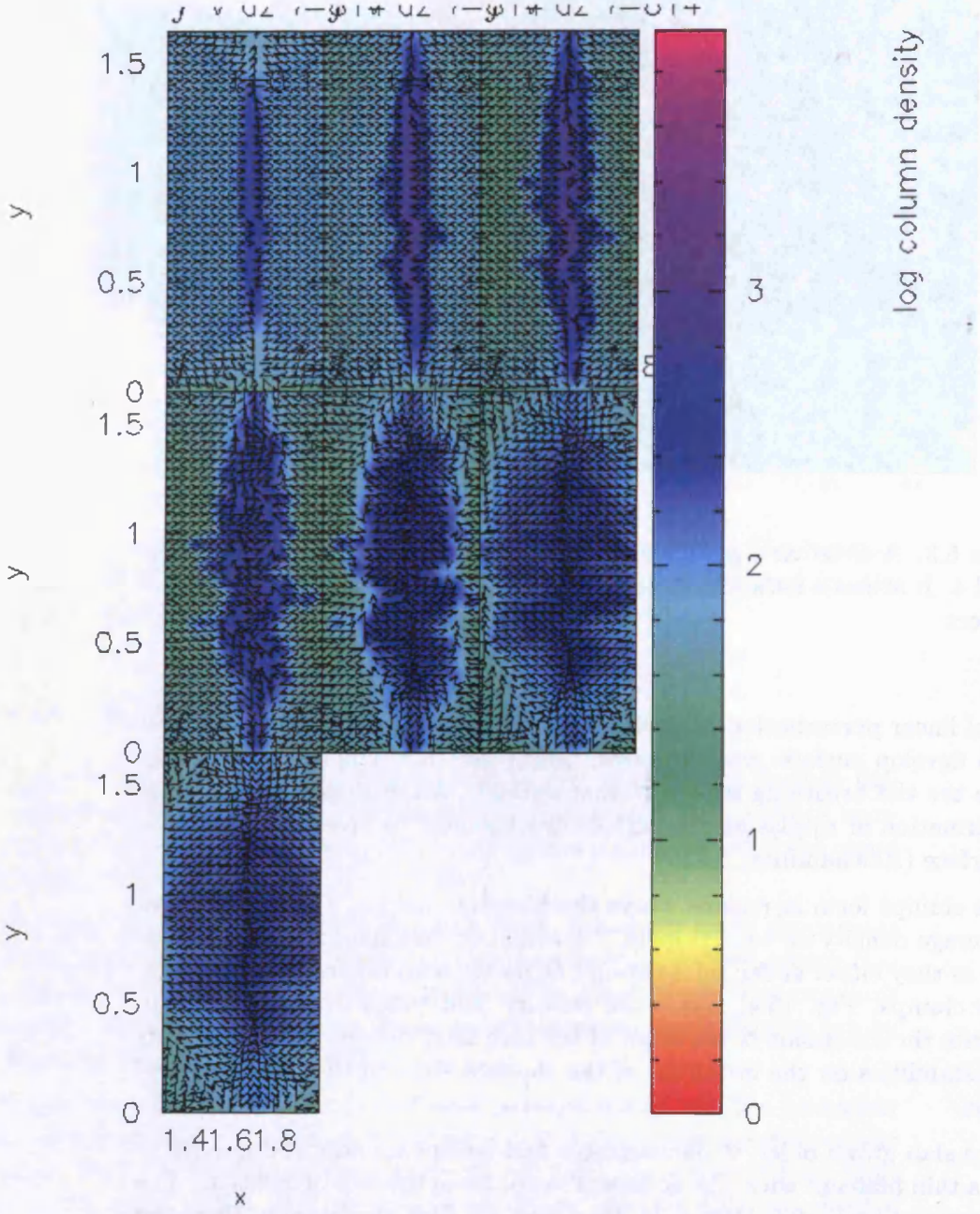

Figure 5.4: The shocked slab in model 4. The initial perturbation of the shocked slab is evident from the pictures in the top panel. Pictures in the second panel show the bending and breathing modes of the slab, as it continues to accrete matter. In the fourth frame we can also see, the development of a circular velocity field within the slab due to turbulent mixing between layers. The instability then saturates as can be seen in the bottom panel.

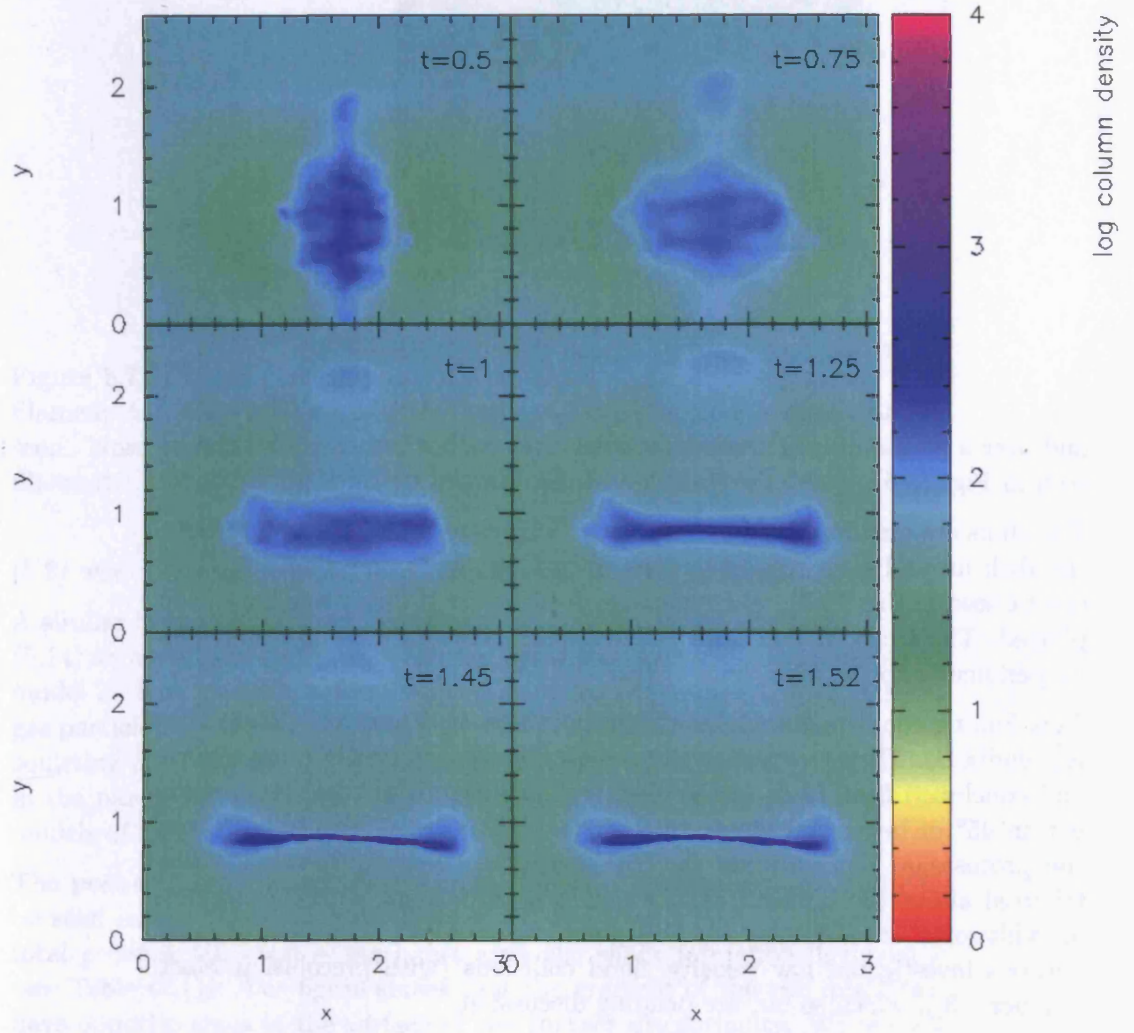

Figure 5.5: Snapshots of various stages of collapse of the shocked slab in model 4. The NTSI goes into saturation and consequently the slab collapses to form a thin, long filament along the x axis. Sinks then form in this filament, as seen in the bottom panel. See also Fig. (5.5) below.

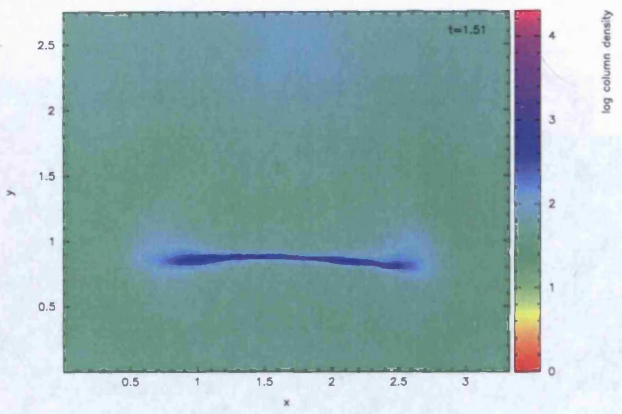

Figure 5.6: Continued from Fig. (5.4) above.

and over a period of $\sim 10^5$ yrs, eight sinks form in the filament. This can be seen in Fig. (5.6), where the sinks have been marked by thick purple dots.

The sinks are circumscribed by respective accretion disks and we note that, the disk around each respective sink is orthogonal to the filament. This can be seen in Fig. (5.7), where particle positions in the xy plane have been plotted. The arched filament with eight sinks, each with its protostellar disk perpendicular to the filament is evident.

This finding conflicts with that of Anathpindika & Whitworth (2008) (See Appendix B). They surveyed five low mass filamentary star forming regions and concluded that 72 % of the observed outflows from these regions are within 45° of being orthogonal to their natal filaments. This implies that the protostellar disks around the YSOs driving these outflows must distributed about the filament axis, which is in agreement with the findings of Whitworth *et al* (1995). At this point, we stress that these latter simulations investigated low velocity cloud collisions (with precollision Mach number ~3), which so far, are pending discussion.

Other high velocity head-on cloud collision models :

The remaining models belonging to this category also show a behaviour similar to that observed in Case **I**. Fig. (5.8) for instance, shows the time sequence of cloud collision in model 3. The velocity field over the shocked region has been overlayed on the column density plots to show the turbulent velocity field within the slab. We can see the subsequent mixing between the slab layers. This sequence of column density plots is continued into Fig.

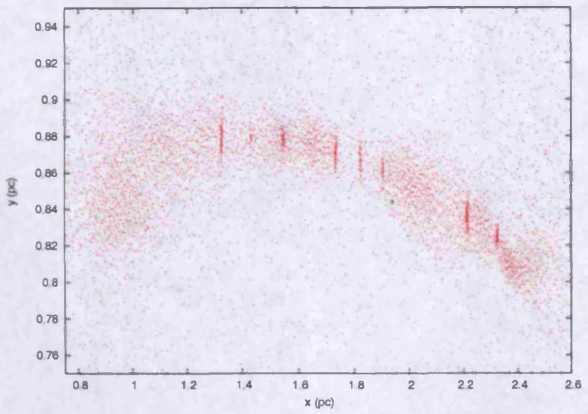

Figure 5.7: Plot of particle positions in model 4, in the x - y plane. The filament and the eight sinks with their respective accretion disks can be seen. Note that the accretion disks around sinks are perpendicular to the filament.

(5.9) where we can now see, that the slab has become bloated.

A similar behaviour of the shocked slab is observed in models 6 and 7. Fig. (5.14) shows a time sequence of column density snapshots, corresponding to model 7. This model is better resolved as compared to case **I**, with 100,000 gas particles. There is no ICM in this case. The slab oscillations and the gas squirting out from the upper and lower end of the shocked slab, are visible in the panels of this figure. This latter phenomenon is observed in all the models of highly supersonic head-on cloud collision presented here

The post-collision contact discontinuity indeed becomes unstable and can be seen in the following way. Figure (5.11) shows a plot of density and total pressure (thermal + ram) just after the shock formation in model 7 (see Table (4.1)). The figure shows that the gradient of the two quantities have opposite signs at the surface of the contact discontinuity. We remind the reader that, this model employs the modified equation of state given by Equation (4.15).

The sudden drop in the total pressure across the discontinuity is the result of a transition from being isotropic, thermal pressure (at the contact discontinuity), to being ram pressure on the outer surface of the discontinuity. As a result, the interface between the slab surface and material being freshly accreted may become unstable. Unlike Hunter *et al* (1986), we are however,

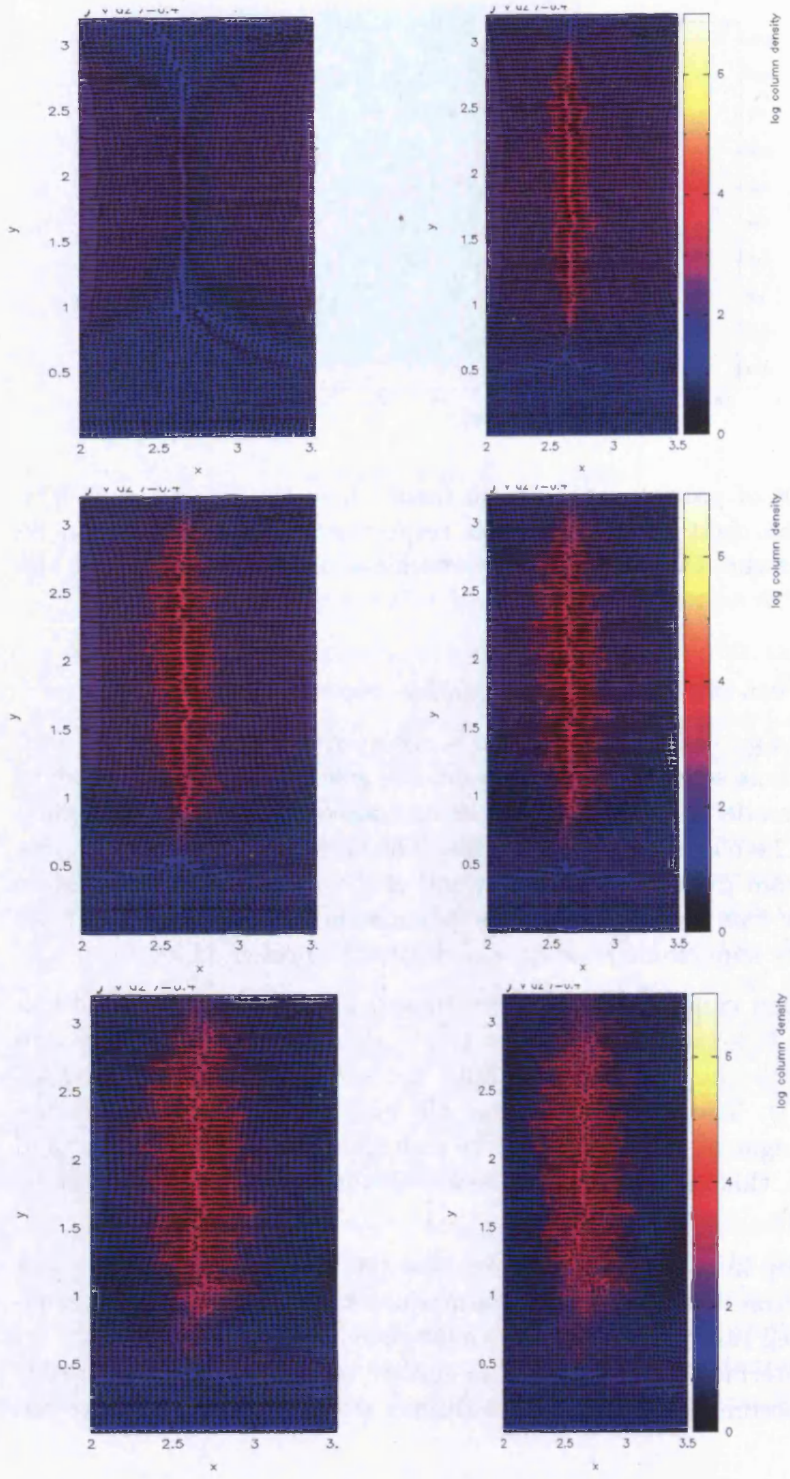

Figure 5.8: The evolution of the shocked slab in model 3 due to growth of the NTSI. See also Fig. (5.9).

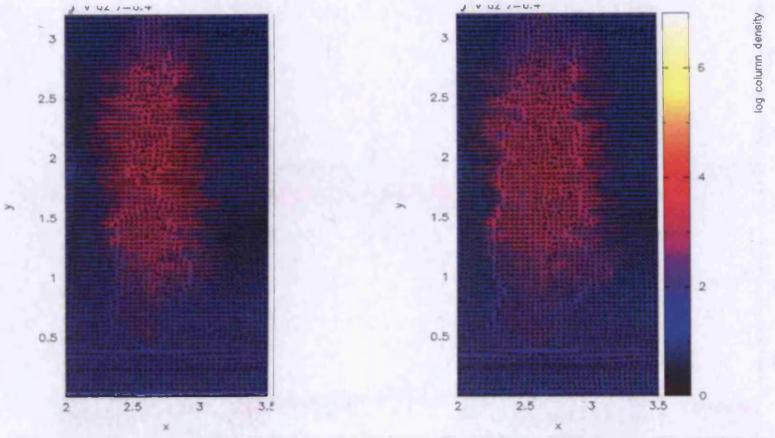

Figure 5.9: Continuation of Fig. (5.8).

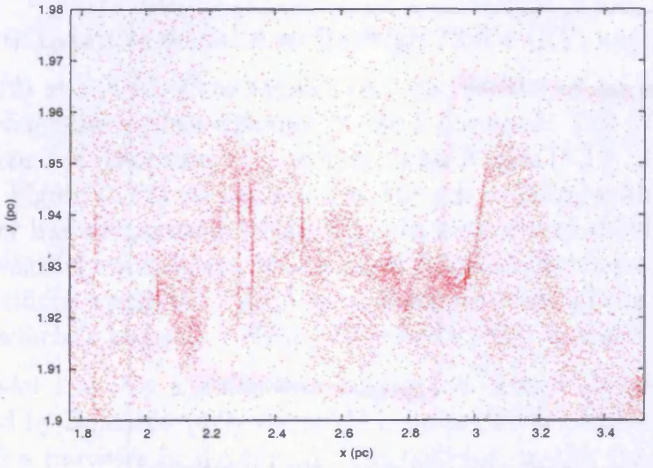

Figure 5.10: Plot of particle positions in the x - y plane in model 3. A section of the filament has been shown, with seven sinks and their respective accretion disks. Once again, notice that the disks are perpendicular to the filament.

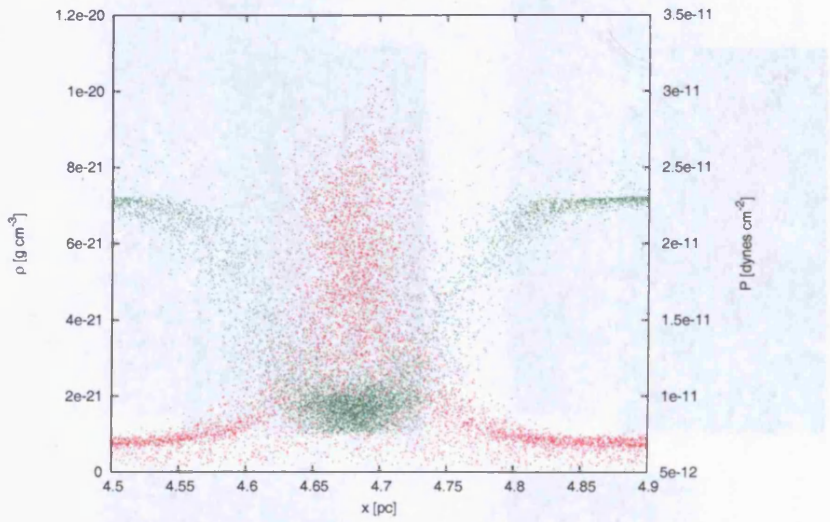

Figure 5.11: Plot of ρ (red dots) and P (green dots) against distance in the x direction for model 7. See Table (4.1) for physical details of model 7.

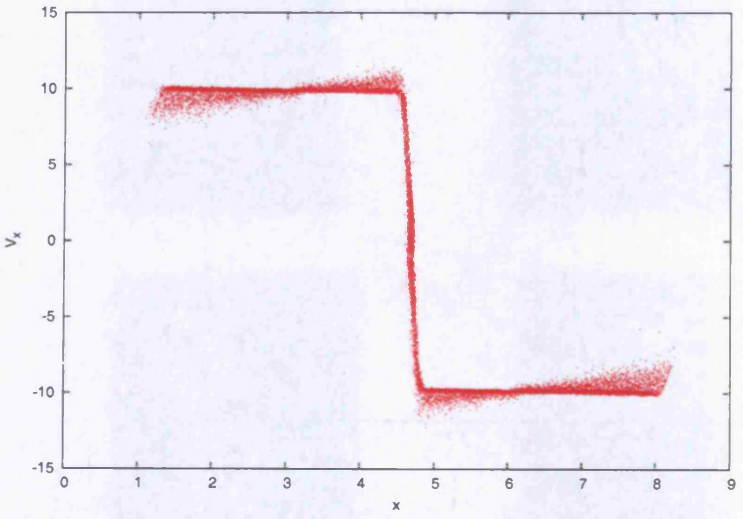

Figure 5.12: Plot of the post shock jump in the x component of velocity against the distance in x direction for model 7. The epoch for this plot is the same as that for Fig. (5.11).

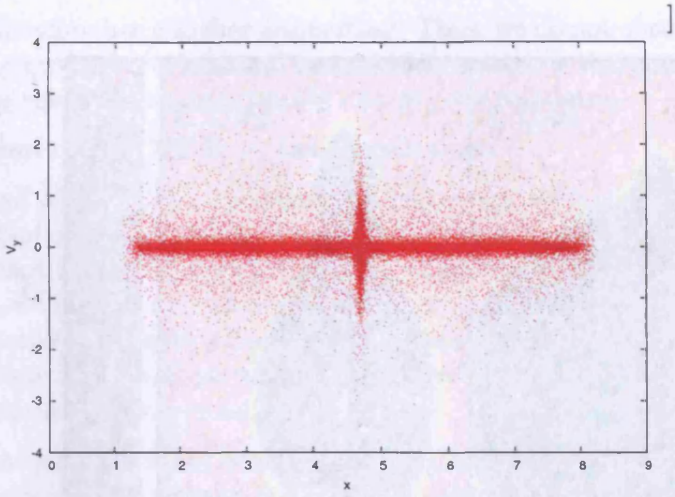

Figure 5.13: Plot of the post shock y component of velocity against the distance in x direction for model 7. The epoch for this plot is the same as that for Figs. (5.11) and (5.12). We can see that post collision, there is supersonic transverse velocity component.

disinclined to term this situation as Rayleigh-Taylor (RT) unstable.

Figures (5.12) and (5.13) show respectively, the profiles of the x and y components of velocities against distance in the x direction. The formation of a stationary contact discontinuity is evident from Figure (5.12). On the other hand, from Figure (5.13) we can see that the gas colliding with the contact discontinuity has a supersonic (relative to the local sound speed in the slab) transverse velocity component. The contact discontinuity is smeared due to the SPH artificial viscosity. Thus, there is strong shear within the slab, as a result of which it becomes Kelvin - Helmholtz (KH) unstable.

Finally, model 1 is only a crude test, performed using a simple barotropic EOS defined by Equation (4.9) above. It is quite poorly resolved due to the use of too few particles in the clouds. The collision, in this case resulted in a shock compressed slab, which eventually shattered and the material in it simply re-expanded. It is therefore a disappointing test from the perspective of studying dynamical instabilities.

In this model, AV is the only dissipative mechanism, but insufficient to counter the rapid post - shock heating. Consequently the slab simply re-expands. From equation (4.9), it follows that this object does not radiate

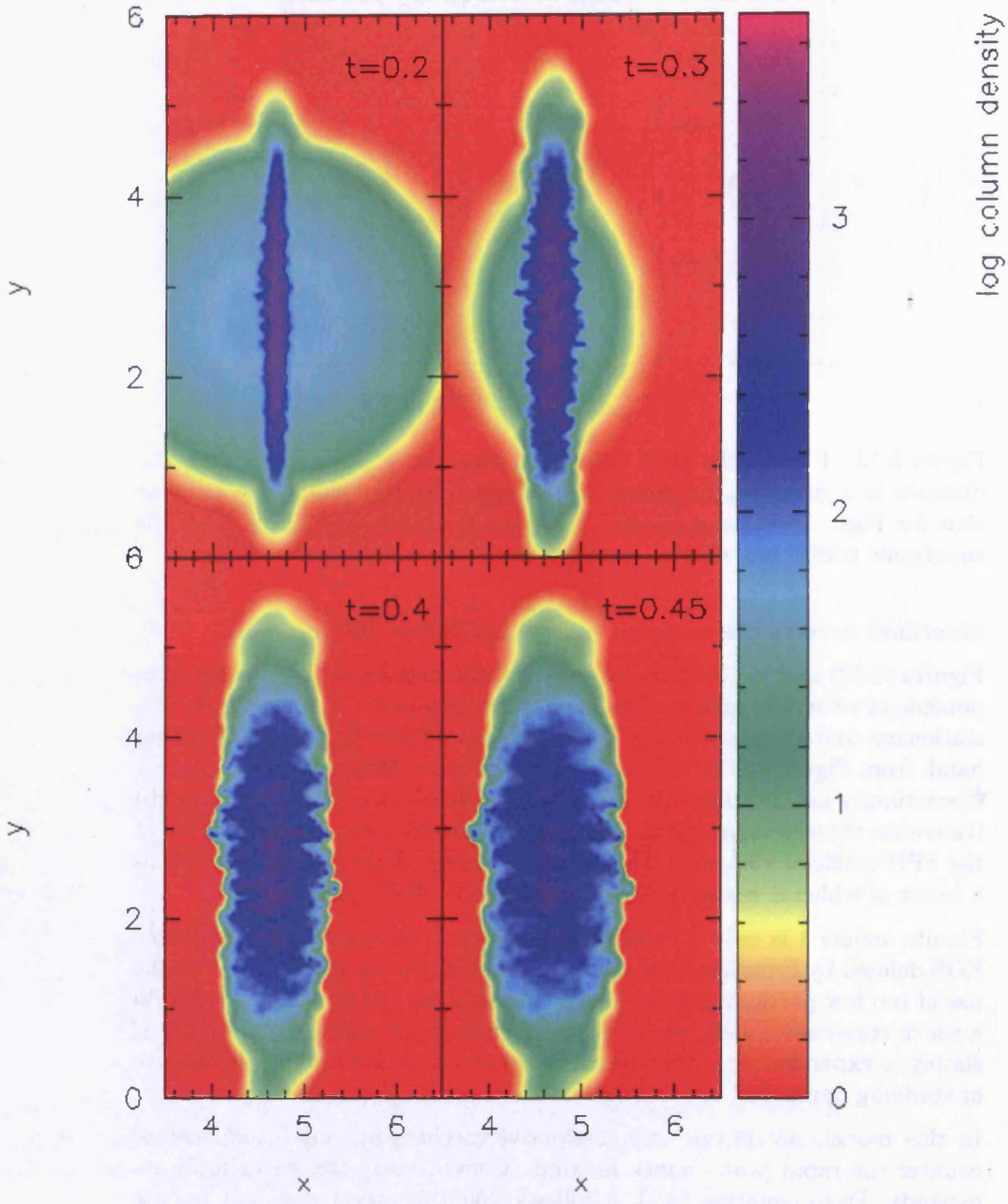

Figure 5.14: Sequence in time of column density plots of the colliding clouds in model 7. The general postcollision features are similar to those observed in earlier models.

heat and therefore has a higher Jeans mass. Thus, we do not observe any evidence for growth of gravitational instabilities, neither is there any evidence for shearing instabilities, presumably due to poor resolution.

Observation of the NTSI in the simulations :

The features of the NTSI discussed previously, are evident in all the high velocity cloud collision models. Figure (5.4) above shows the velocity field in the shocked region, for case **I** discussed above. In the uppermost panel of this figure, we can see a small perturbation on the contact layer. This layer accretes matter and forms a dense stratified slab confined by ram pressure, by which time the initial perturbation also grows. This can be seen in the next two pictures of this panel.

At the subsequent epochs of evolution, mixing between slab layers is evident from the velocity field, plotted on top of the column density plots. Shearing motion between slab layers is responsible for the KH instability. As the slab becomes older, a few breakaway blobs near the slab surface can be seen. This is apparently due to the segregation of particles in regions having a steep density contrast. A gap between the two regions creates artificial boundaries and therefore discontinuities in the SPH interpolation. The usual differential formulation of the SPH equations fails to handle this situation (Agertz *et al*, 2007).

This problem can be fixed by including some additional correction terms to account for thermal energy dissipation across the said boundaries (Price, 2007). Our SFC does not include these corrections, however discounting them does not seem to have any adverse bearing on the results of the simulations, neither is it our aim here to model the KH instabilities in their minute details. Turbulent mixing of fluid layers leads to the formation of vortices, which effectively dissipate thermal energy. By measuring the amplitude of the growing perturbation and the slab thickness, we estimate the growth rate of the NTSI. In model 4 the observed growth rate of the NTSI is

$$\tau^{-1} \sim 0.5(kL)^{0.81}, \tag{5.6}$$

where all symbols have their usual meanings.

Figure (5.15) below shows the growth rate of the NTSI in this particular experiment (model 4). The red curve corresponds to the actual, observed rate in the simulation while the smooth, green curve corresponds to the power law given by Equation (5.6) above. The growth rate given by Equation (5.6) is in excellent agreement with that observed by Blondin & Marks

(1996) and Klein & Woods (1998). Their suggested growth rate is, $\tau^{-1} \sim 0.4(kL)^{0.7}$. These growth rates however, do not match with that suggested by Vishniac (1994), given by Equation (5.5) above. This later equation predicts a much faster growth of the instability ($k^{1.5}$).

The other three models viz. 3, 6 & 7 also exhibit a similar behaviour. The snapshots in Figs. (5.8) and (5.9) show a time sequence of evolution of the shock compressed slab in model 3. The velocity field overlayed on these plots show the direction of flow of material on the slab and the subsequent mixing between the slab layers. This sequence of column density plots is continued into Fig. (5.9) where we can now see, that the slab has become bloated.

The bloated slab collapses and forms a filament parallel to the collision axis, with a large aspect ratio. Fig. (5.10) shows only a section of the entire filament. The sink formation commences rather early in this model as compared to that in case **I** and the first sink forms at $t \sim 0.77$ Myr. With an increase in the column density, the wavelength of gravitational instability becomes shorter and its growth rate increases. Hence gravitational clustering is seen earlier in this model as compared to case **I**.

Once again, we observe a similar sequence in the evolution of the shocked slab in model 7, as is evident from Fig. (5.14). This model is better resolved as compared to those described above, with 100,000 gas particles. There is no ICM in this case. The slab oscillations and the gas squirting out from the upper and lower end of the shocked slab, are visible in the panels of this figure. This latter phenomenon is observed in all the models of highly supersonic head-on cloud collision presented here.

In Fig. (5.9) and the bottom panel of Fig. (5.14) respectively, the NTSI appears to be at a fairly advanced stage of its evolution. Evidence of this instability has also been observed in recent simulations of colliding turbulent fluid flows, performed by employing the finite difference scheme (Heitsch *et al*, 2008). At this point, we note that similar breakaway blobs, having densities at least two orders of magnitude less than those observed in our simulations, have been reported by these authors. They interpret this observation as evidence for core formation. Contrary to their conclusion, we are inclined to discount the blobs as numerical artifacts despite their reasonably high densities ($\sim 10^{-18}$ g cm^{-3}). The calculations in models 6 and 7 were terminated immediately after the filament formation.

However, we do observe structure formation in the shocked slab fairly soon

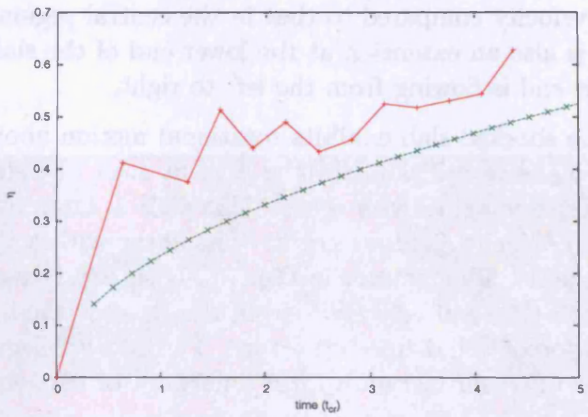

Figure 5.15: The growth rate of the NTSI in model 4. The red curve corresponds to the actual growth rate of NTSI in the simulation while the green curve is a power law fit to the observed growth rate ($\eta \equiv kL$ in Eqn. (5.6)). Time on the x axis is measured in units of the cloud crushing time t_{cr} defined above in §5.3.1.

after its formation, as can be seen in Fig. (5.2). If we relax our scepticism about these blobs, then it implies that core formation can occur even when the NTSI dominates the slab behaviour. However, these cores are too turbulent and do not collapse under self gravity.

5.3.2 Case II (High velocity off-centre collision):

We have tested only one off-centre cloud collision model here. In model 5, the clouds are allowed to collide at a finite impact parameter, $b = \frac{R_{cld}}{4}$. This collision produces an oblique shock compressed layer. The snapshots in Fig. (5.16) show the sequence of evolution of the oblique shocked slab in model 5. The high velocity off-centre collision of clouds produces an oblique shock compressed slab. Unlike the plane parallel slabs formed in the head-on collision, in this case we observe that the slab apparently has three distinct regions. The central planar region and the two arched extensions at the top and bottom ends of the slab.

The oblique shocked slab has these extended features due to the fact that the initial shock front effectively blocks the fluid flow from either sides in the central regions, while at the top end where the fluid flows from the right to

left, has higher transverse velocity compared to that in the central regions. For the same reason there is also an extension at the lower end of the slab, except that the fluid at this end is flowing from the left to right.

We observe that the oblique shocked slab exhibits rotational motion about an axis orthogonal to the plane of collision. In the present case, the slab rotates about the z axis in an anticlockwise sense. The slab is internally stressed by the non-uniform velocity field within it. The shear within the slab layers makes it KH unstable. The pictures in Fig. (5.17) show a face-on view of the shocked slab with the local velocity field in the slab. In the top panel, we can see the formation of well defined structure. The slab breaks up to form several blobs, a few of which merge to form a network of filaments and larger clumps.

The lower panel in Fig. (5.17) shows a close-in view of clumps undergoing merger. The slab dissipates thermal support through internal shearing motion. Usami, Hanawa & Fujimoto (1995) provide a detailed analytic account of such oblique shock compressed slabs. They conclude that gravitational instabilities are suppressed in slabs dominated by shearing motion. Shearing motion increases the effective sound speed and therefore damps the growth rate of the gravitational instability.

They further predict that the end product of such slabs is an elongated object, similar to the one we observe at the end of this calculation. We terminated this calculation after a sink was formed in the filament. We note that the sink formation is delayed in this case as compared to the high velocity, head-on cloud collisions discussed in case **I** above. This is presumably due to the additional support provided by the angular momentum associated with rotation of the slab. The sink formation in this model is delayed and the first sink is formed after $t \sim 1.92$ Myrs.

In particular we note that there is no evidence for the NTSI, which dominated the evolution of the shock compressed slab produced by the high velocity head-on cloud collision. The Coriolis force acting on the rotating slab in the present case tends to suppress perturbations normal to the slab surface, in other words the bending modes of the slab. Without perturbations on the slab surface, the NTSI cannot grow.

This is however, contrary to the findings of Whitworth *et al* (1995) where they simulated low velocity ($\sim$1.6 km s^{-1}), off-centre cloud collisions. They found that sufficiently dense regions in the filament collapsed under self gravity and the collapsing region was fed with material channelled by the

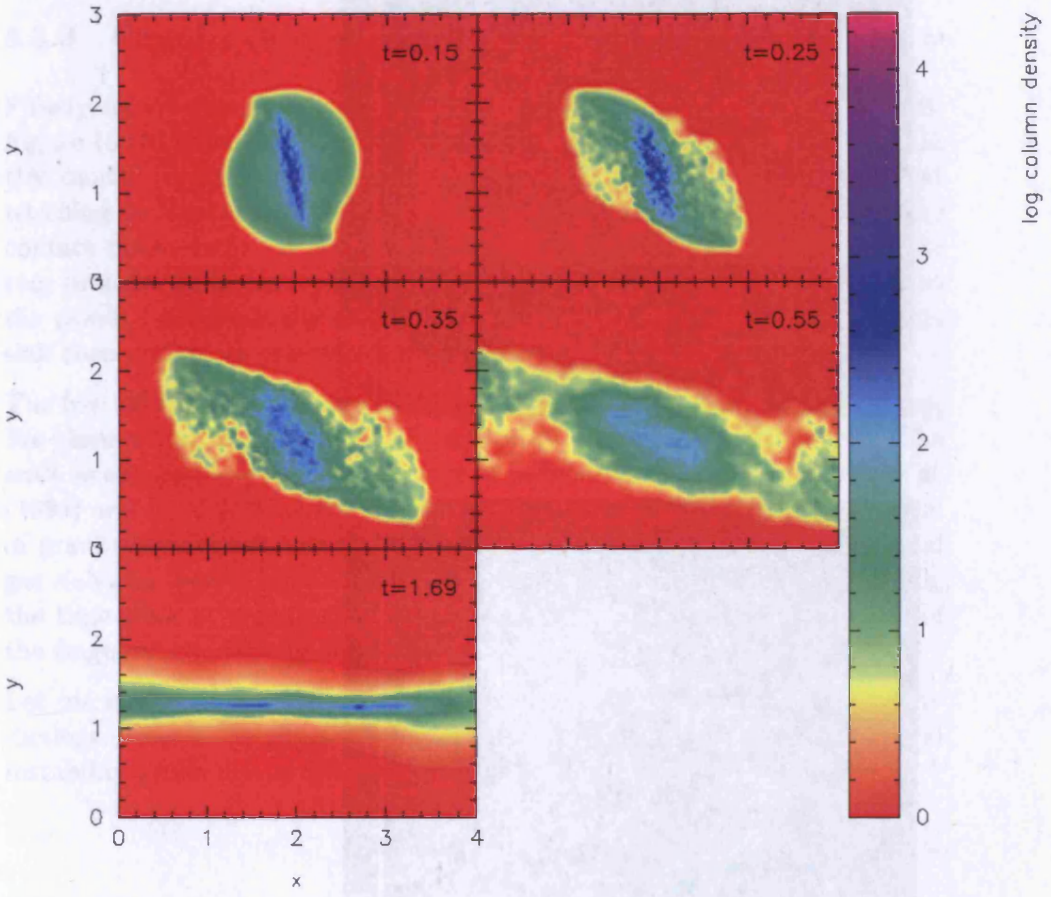

Figure 5.16: The collision of clouds in model 5. The off centre cloud collision leads to the formation of an oblique shocked slab as can be seen in the top panel. The shocked slab then breaks into three parts and the outer two lobes of the slab move away from the central region of the slab. The slab continues to tumble about the z axis (also its angular momentum axis) and finally forms a filament parallel to the x axis.

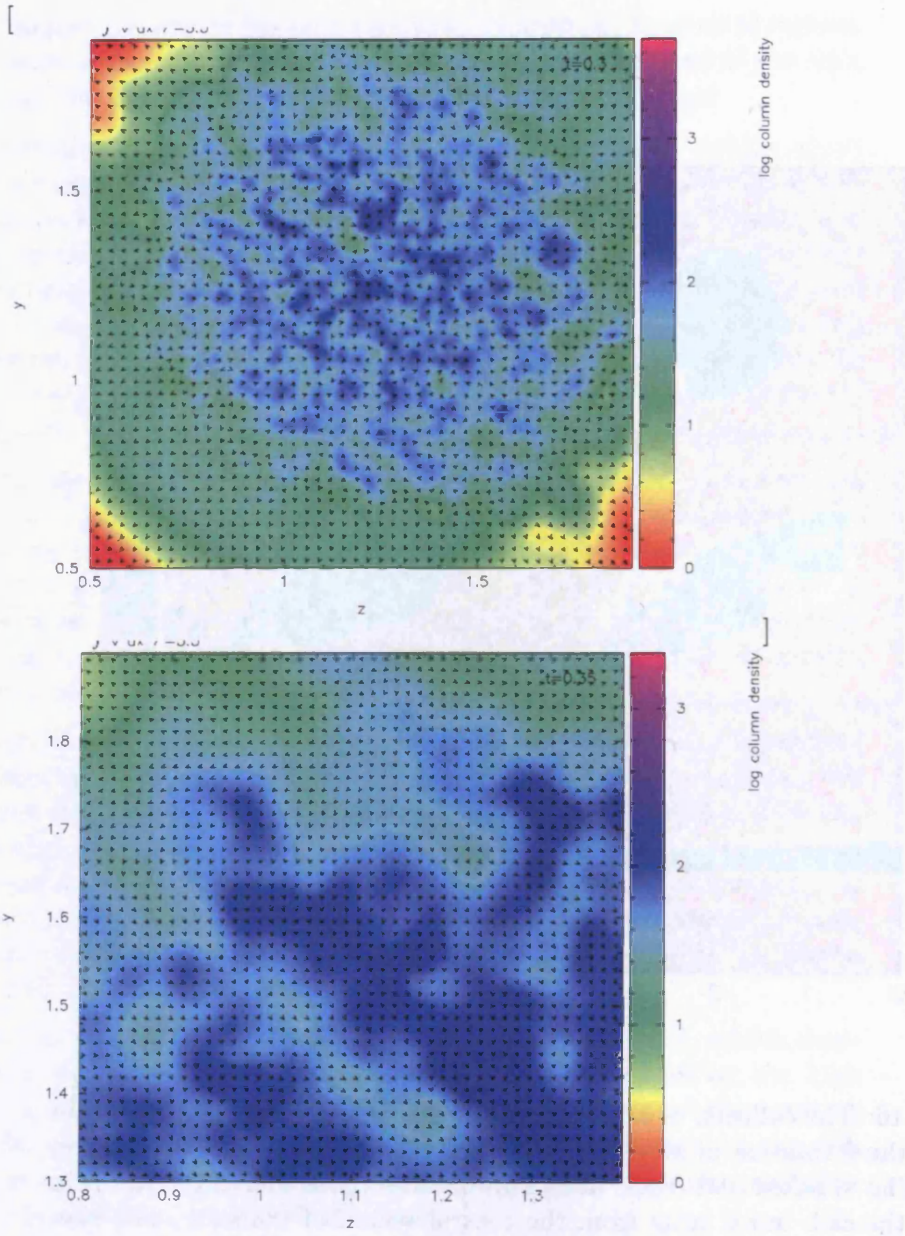

Figure 5.17: The face-on view of the oblique shocked slab formed in model 5. In the top panel, initial structure formation is clearly visible. It shows well defined filamentary regions and clumps. The velocity field overlayed on this plot shows the turbulent motion within the slab. Smaller clumps merge to form larger clumps. The picture in the lower panel shows formation of larger clumps through merger of smaller clumps.

filament that resulted from cloud collision. The protostellar object continued to accrete matter through an accretion disk oriented orthogonal to the direction of angular momentum vector of the filament.

5.3.3 Case III (low velocity head-on cloud collision) :

Finally, let me discuss model 8, pertaining to the low velocity cloud collision. Figure (5.16) shows six column density snapshots of the colliding clouds in this model. In the topmost panel of this figure we can see the clouds just touching each other and then forming the initial contact discontinuity. The contact discontinuity is acted upon by isotropic, external pressure, unlike ram pressure as in Cases **I** and **II**. In the next two panels we can see that the clouds have gradually collapsed on the pressure compressed slab. This slab then undergoes gravitational fragmentation.

The free fall time of individual clouds in model 8, is $\sim (G\rho_{cld})^{-1/2} \sim 3$ Myrs. We observe that the gravitational instability grows on a much shorter time scale as compared to the free fall time of individual clouds. Whitworth *et al*, (1994) and Boyd & Whitworth (2005) semi analytically treated the problem of gravitational fragmentation of an external pressure confined isothermal gas slab and derived expressions for the length of the fastest growing mode, the time scale of growth of this mode, $t_{fastest}$, and the minimum mass of the fragment condensing out of this slab.

Let me now compare the observations made in this model with their predictions. This is the timescale over which the fastest mode of gravitational instability grows and is defined as,

$$t_{fastest} \sim \frac{2a_{layer}}{G\Sigma_{layer}}, \tag{5.7}$$

Whitworth *et al* (1994). For the present case $t_{fastest}$ is of order a fraction of a Myr, which again, is in agreement with the epoch at which the slab starts fragmenting ($\sim$0.2 Myr).

The time required for the growth of gravitational instability, (t_{growth}), and then condensation of a clump is given as,

$$t_{growth} \sim \Big(\frac{L}{G\sigma_{layer} - a_{layer}^2 L^{-1}}\Big)^{\frac{1}{2}}. \tag{5.8}$$

Here L is the size of the clump, σ_{layer} is the average surface density of the slab and a_{layer} the average sound speed in the slab; $t_{growth} = 0.6$ Myr for the

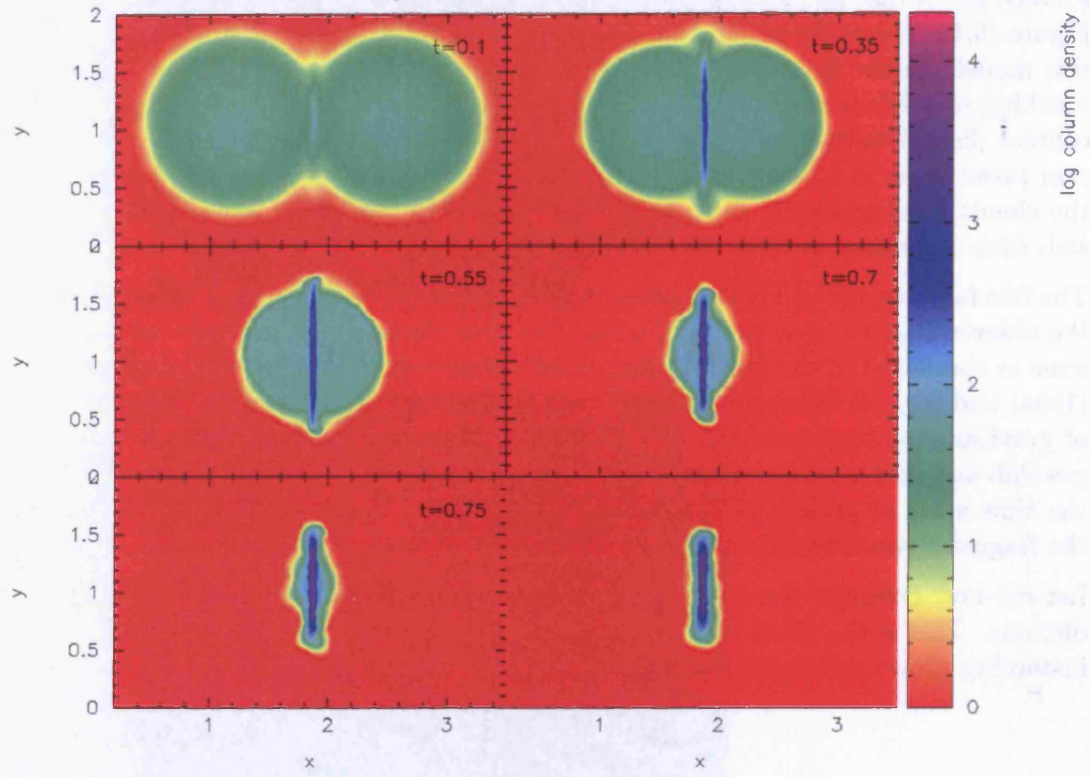

Figure 5.18: Sequence in time (Myrs) of colliding clouds in Model 8. The collision in this case results in the formation of a pressure confined slab. See text for further description.

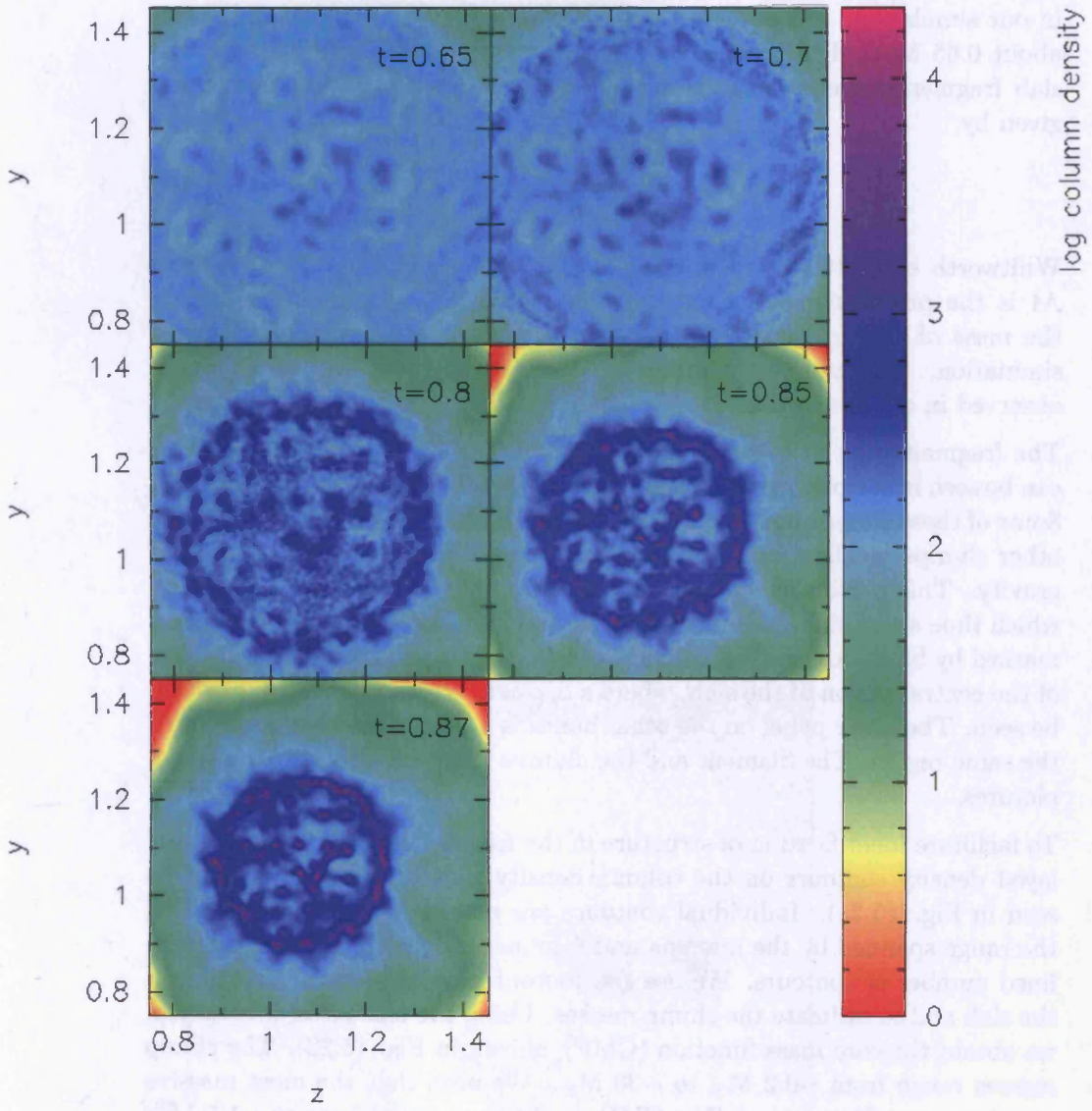

Figure 5.19: Gravitational fragmentation of the pressure compressed slab in model 8. These pictures provide the face on view of the slab in the y - z plane. We can clearly see the formation of clumps in the pictures in the top panel. These clumps then merge with each other and form filamentary structures as seen in pictures in the second panel. Sufficiently dense regions in these structures undergo gravitational collapse. Sinks (bright purple dots) can be seen in pictures in the bottom panel.

model under investigation, which is in agreement with the epoch observed in our simulation. We observe that the clump formation commences after about 0.65 Myr. The gravitational instability then grows quickly and the slab fragments into several clumps. The minimum mass of a fragment is given by

$$M_{frag} = \mathcal{M}^{\frac{1}{2}} \frac{a_{layer}^3}{(G^3 \bar{\rho}_{layer})^{\frac{1}{2}}}, \tag{5.9}$$

Whitworth *et al* (1994), where $\bar{\rho}_{layer}$ is the average density of the layer and $\mathcal{M}$ is the precollision Mach number. Using Equation (5.9), we calculate the mass of this fragment, M_{frag}, as 0.32 $M_\odot$ (0.22 $M_\odot$) for the present simulation. The number in brackets is the minimum mass of a fragment observed in our simulation. It is reasonably close to the expected value.

The fragmentation of this slab results in the formation of 36 clumps. This can be seen in the pictures shown in the second and third panel of Fig. (5.19). Some of these clumps undergo merger and form filamentary structures, while other clumps oscillate for a few thousand years before collapsing under self gravity. This particular simulation was terminated after $t \sim 0.87$ Myr by which time seven sinks had formed in the fragmented slab. These have been marked by black dots in the top panel of Fig. (5.20). It shows a close in view of the central region of the slab, where a filament with five small clumps can be seen. The lower panel on the other hand, is a plot of particle positions in the same region. The filament and the clumps in it, are also visible in these pictures.

To facilitate identification of structure in the fragmented slab, we have overlayed density contours on the column density plot of this slab, as can be seen in Fig. (5.21). Individual contours are placed by uniformly dividing the range spanned by the maxima and minima in density, between a predefined number of contours. We use the contour plot to identify structure in the slab and to estimate the clump masses. Using the masses so determined, we obtain the core mass function (CMF), shown in Fig. (5.22). The clump masses range from $\sim$0.2 $M_\odot$ to $\sim$30 $M_\odot$. We note that the most massive structures are filamentary. The CMF so obtained has a knee at $\sim$1.5 $M_\odot$. We fit a powerlaw to the high mass regime $\left(\frac{M}{M_\odot} > 1.5\right)$ of this CMF, with a slope -1.7 which according to the χ^2 test, has about 30% significance level. This slope is in reasonable agreement with that suggested by, for e.g. Clark, Klessen & Bonnell (2007); Nutter & Ward-Thompson (2007), for example.

The slab as seen in Fig. (5.21), is at a fairly advanced stage of its evo-

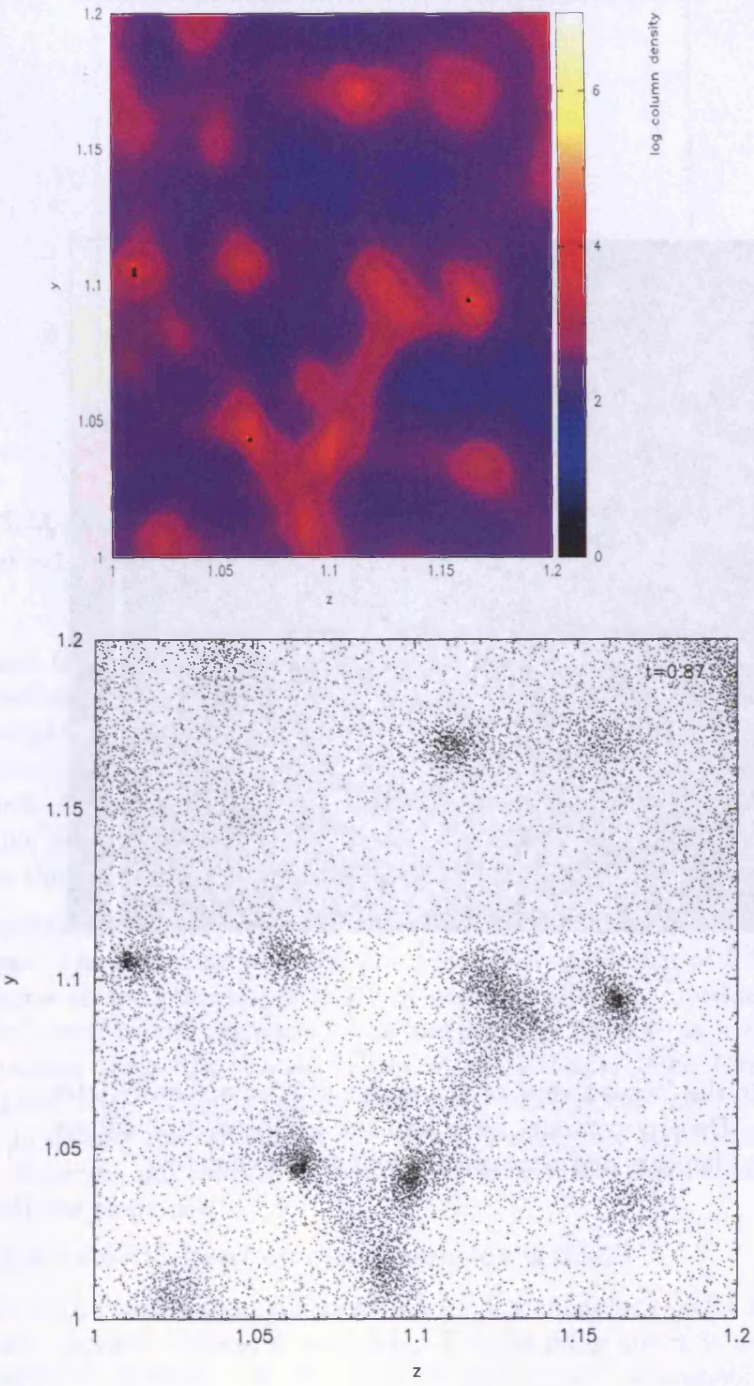

Figure 5.20: The picture in the upper panel shows a close up view of a filamentary region in the slab. In the lower picture, particle positions are plotted for the same region. Three sinks, in the upper picture have been marked as black dots.

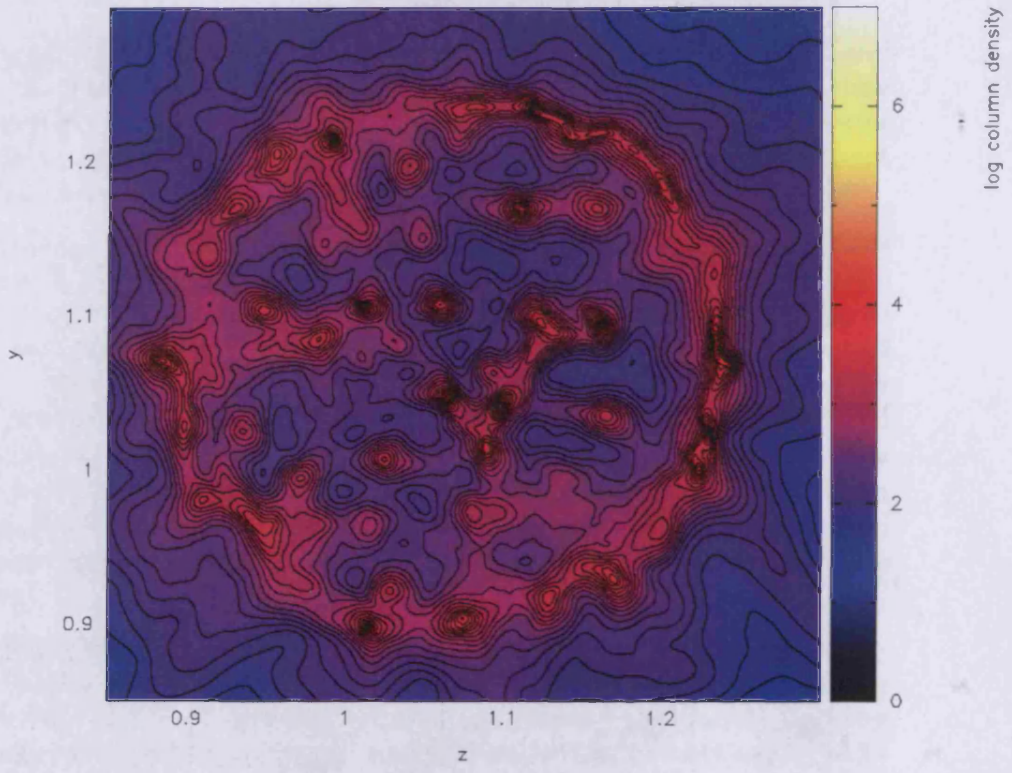

Figure 5.21: This is the face on view of the entire slab at a slightly later time, t ~0.85 Myr. Density contours have also been plotted, to facilitate identification of the filaments and clumps. See text for more detail.

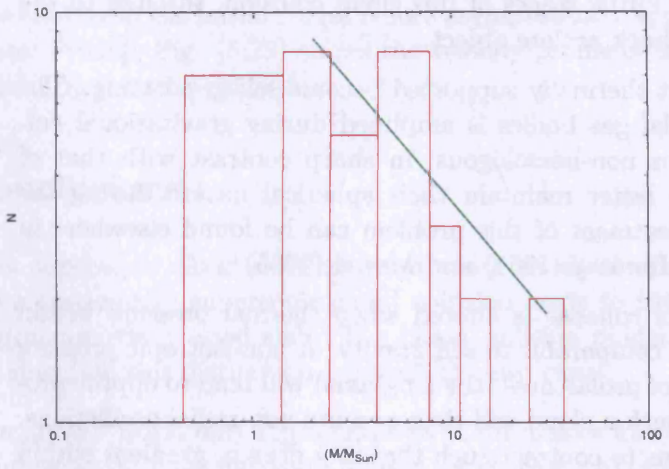

Figure 5.22: The CMF for 36 cores identified in model 8. The turnover occurs at ~1.5 $M_\odot$. The slope for $\left(\frac{M}{M_\odot}\right) > 1.5\ M_\odot$ is -1.7 .

lution and the densest clumps have already commenced gravitational collapse leading to sink formation. By this time the gravitational instability has already saturated, by which it is meant that there is no more structure formation. The corresponding timescale is called the saturation time, $t_{sat} \sim 0.25(G\rho_{cld})^{\frac{-1}{2}}$ (Elmegreen, 1989). For the present case, $t_{sat} \sim 0.8$ Myr. This is very close to the epoch (0.85 Myr) at which we observe saturation in the simulation.

We suggest such fragmentation as one of the mechanisms for star cluster formation. The commencement of sink formation at the tip of a filament is analogous to the observation made in case of a cluster embedded in an elongated cloud in the region IC 546, purportedly formed as a result of some dynamic triggering process (Lada, Alves & Lada, 1999; Elmegreen, 2002). From Fig. (5.21) it can be seen that, most of the gas in the slab ends up in density structures and the region between the structures is well cleared. However, this calculation was forced to be halted due to inadequate computational resources.

Other low velocity head-on cloud collision model :

In model 2 the two clouds collide at a very low velocity (~0.53 km s^{-1}) and form a prolate composite gas body. The resulting shock is weak due to the small precollision velocity. The column density snapshots in Fig.

(5.23) below, show the initial stages of this cloud collision, through to the formation of the post shock prolate object.

Gas bodies that are not thermally supported become self gravitating. The eccentricity of spheroidal gas bodies is amplified during gravitational collapse. Their collapse is non-homologous, in sharp contrast with that of spherical bodies. The latter maintain their spherical nature during the collapse. Analytical treatment of this problem can be found elsewhere in literature, for instance Ramsay (1961) and Mestel (1965).

However, the picture of collapse is altered when thermal pressure within the the prolate cloud is comparable to self gravity. A non-isotropic pressure gradient along the axis of prolateness (the long-axis) will tend to oppose prolateness of the cloud. Such a cloud will then execute non-radial oscillations. The prolate cloud begins to contract such that any density gradient within it becomes less pronounced and the collapse during this phase is more or less homologous. But once it has sufficiently flattened such that the pressure gradient along the long axis becomes comparable to the self gravity, the collapse becomes non-homologous. The length scale of the spheroid is $\sim \left(\frac{a_0^2}{2\pi G\bar{\rho}}\right)^{\frac{1}{2}}$, where $\bar{\rho}$ is the equatorial density (Mestel, 1961). The collapse finally terminates in a cylinder.

The postcollision prolate object formed in this simulation undergoes such a collapse, as can be seen in the panel of pictures in Fig. (5.24). The collapse terminates in a cylinder oriented orthogonal to the plane of collision. This collapse is not arrested at any stage as, there is not a sufficient build up of thermal pressure to provide support against self gravity. The collapse continues unarrested if $\sigma > \frac{2a_0^2}{G}$, where σ is the mass per unit length (McCrea, 1961).

We do not observe any secondary fragmentation of this cylinder. This can be attributed to - (a) poor resolution of the model leading to suppression of the gravitational instability (b) thermal heating dictated by the EOS as defined by equation (4.9). A single gravitationally unstable mode though, leads to the formation of a sink, which then continues to accrete gas by forming an accretion disk circumscribing it, see Fig.(5.25) below.

Figure (5.26) shows the time evolution of the density of the densest particle in the simulation. Additionally, the density profiles for the 30^{th} and the 50^{th} most dense particles are also plotted. The three profiles have been shown respectively in red, green and blue colours. Figure (5.27) shows the plot of the mass accreted by the sink particle. It can be seen that accretion

occurs more rapidly in the initial stages before asymptotically approaching a constant rate. Finally, Fig. (5.28) shows the velocity profile of the material being accreted by the sink particle.

5.4 Conclusions :

1. Highly supersonic cloud collision produces a shock compressed slab, while a moderately supersonic cloud collision leads to the formation of a pressure compressed slab. The cloud collision models presented here, elucidate this distinction between the two cases.

2. In the present work, only representative cloud masses have been used. We intend to increase the cloud masses by at least two orders of magnitude by further increasing the number of gas particles with greater computational resources.

3. We observe remarkably different natures of evolution of the two types of post-collision slab. While the shock compressed slab fragments due to the rapid growth of the NTSI, the pressure compressed slab fragments due to the fastest growing mode of the gravitational instability. It then undergoes rapid gravitational fragmentation.

4. Strong shearing instabilities dominate the evolution of the shock compressed slab. In particular we observe evidence for the NTSI in our models discussed under case **I**.

5. Strong shear between slab layers causes turbulent mixing between them. The formation of vortices effectively dissipates thermal energy and fragments. The fragmented slab collapses and forms a filament with a large aspect ratio, along the axis of collision. Gravitational clustering then takes place in this filament .

6. The collapsing clumps in the filament lead to sink formation, and accretion disks circumscribing respective sinks are orthogonal to the natal filaments.

7. Additional support from the angular momentum delays gravitational clumping in the oblique shocked slab.

8. These experiments are highly simplified and therefore too many qualitative details cannot be derived from them. Further, the role of AV in

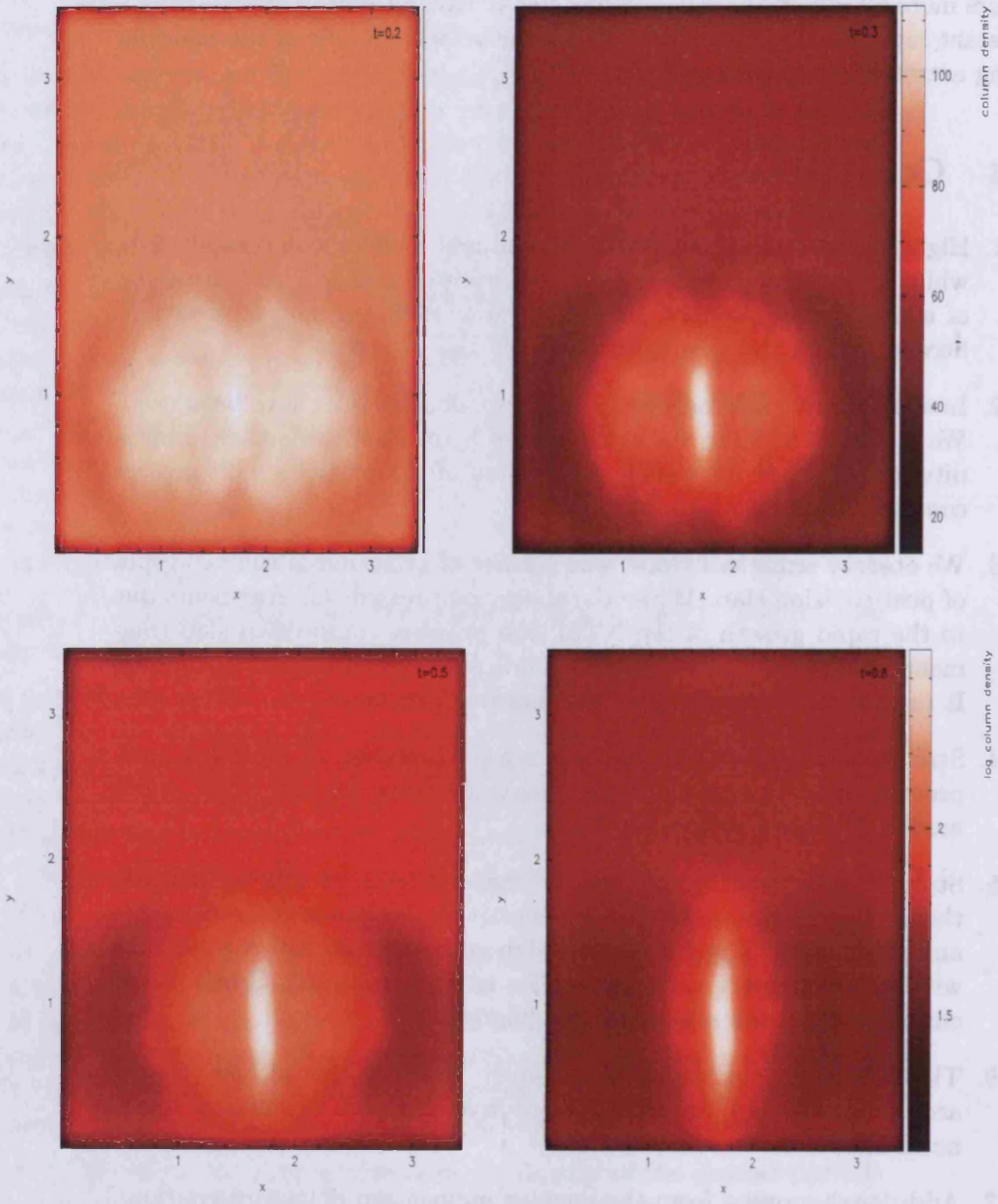

Figure 5.23: Column density plots showing the post collision collapse of the composite object in model 2. Continued in Fig. (5.24).

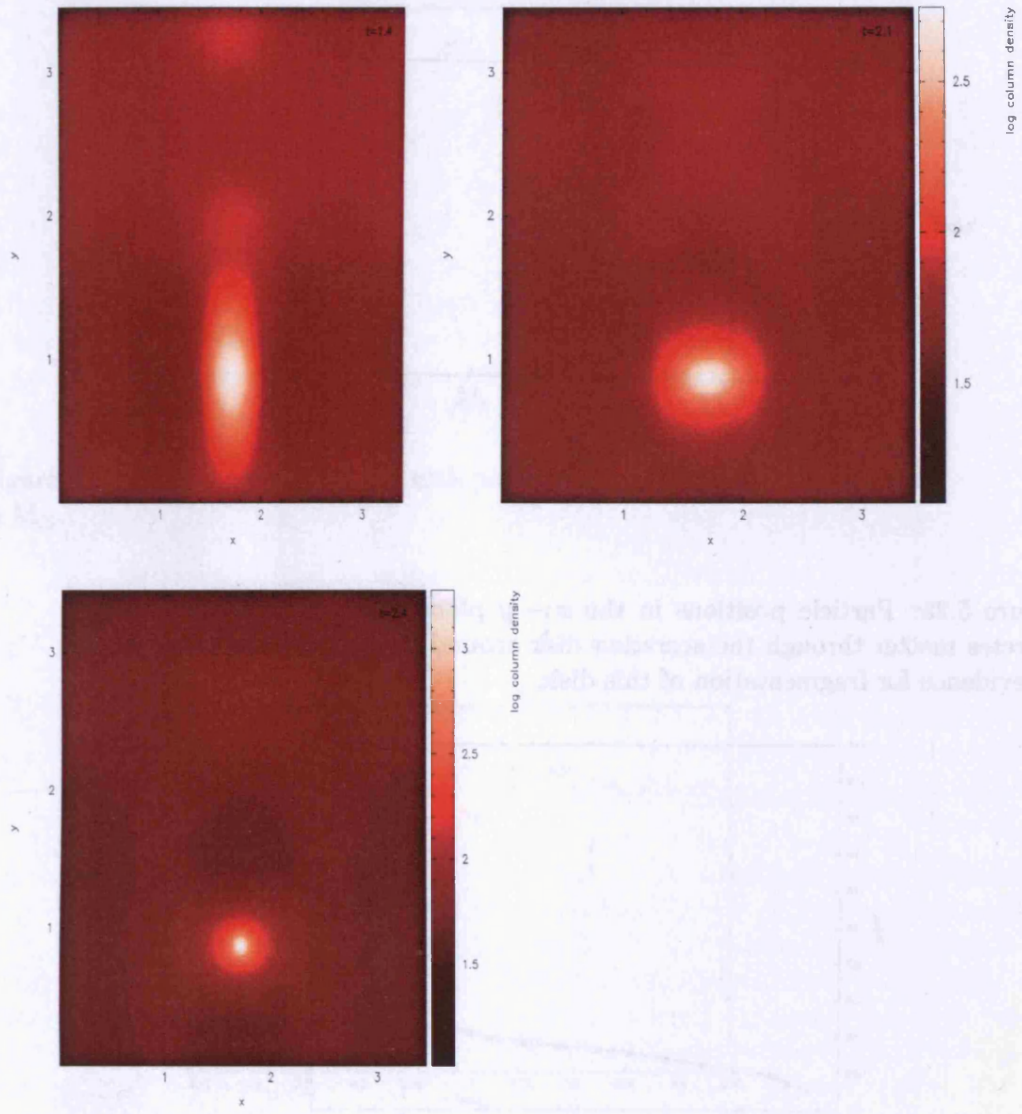

Figure 5.24: Column density plots showing the post collision collapse of the composite object in model 2.

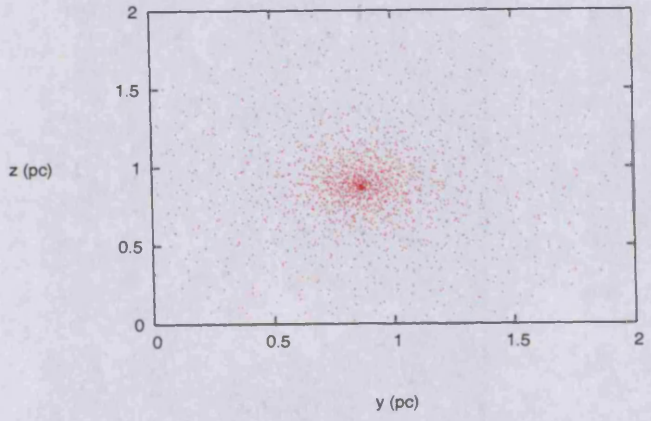

Figure 5.25: Particle positions in the $x - y$ plane in model 2. The sink accretes matter through the accretion disk around itself. However, there is no evidence for fragmentation of this disk.

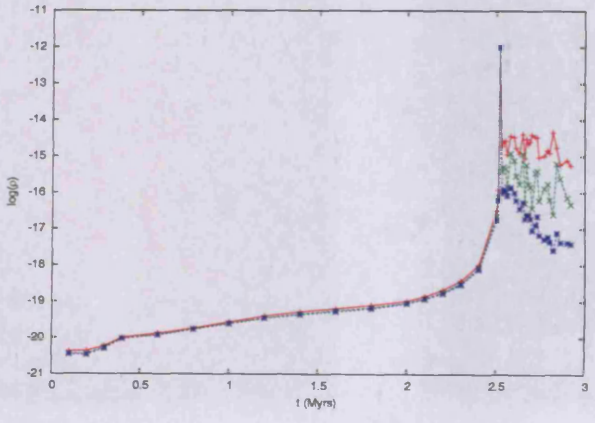

Figure 5.26: Density evolution of the densest particle, 30^{th} most dense and the 50^{th} most dense particle in model 2. The peak is visible at $\rho = \rho_{sink}$ as expected.

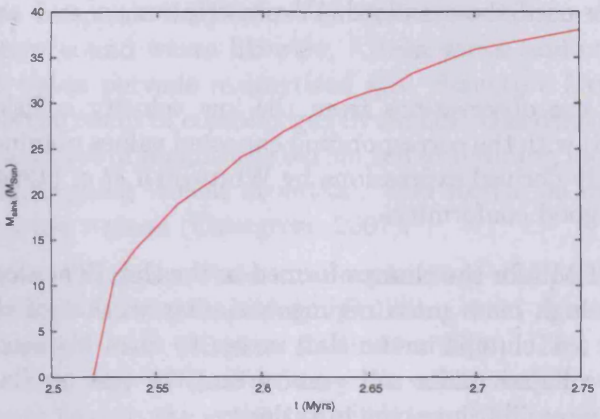

Figure 5.27: Mass accreted by the sink particle in model 2. Mass measured in $M_{\odot}$.

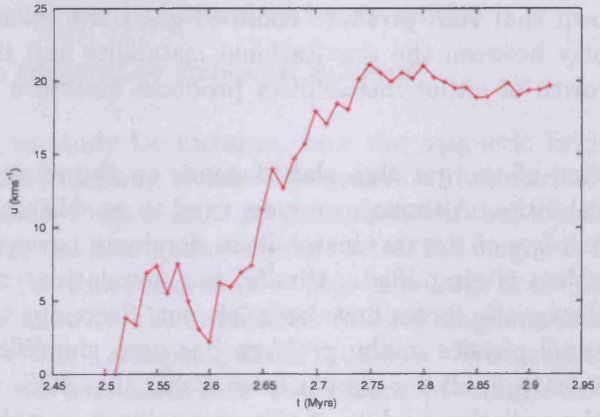

Figure 5.28: Velocity of material being acceretd by the sink in model 2. The profile shows the existence of accretion shocks. The velocity is measured in km s^{-1}.

thermal energy dissipation resulting from strong mixing between the slab layers, needs to be investigated in greater detail. In all the models tested here, we have used the standard AV prescription, $\alpha = 1$ and $\beta = 2$.

9. We have compared the observations from the low velocity collision experiment (model 8) with the corresponding expected values obtained from semi analytically derived expressions by Whitworth *et al* (1994), and find the two in good conformity.

10. We have obtained a CMF for the clumps formed in the slab. The slope of this CMF in the high mass mass regime is similar to that of the observed DCMF. A few clumps in the slab merge to form filaments, while a few others collapse under self gravity and the rest oscillate about their respective equilibrium configurations.

5.4.1 Possible extension of the present work :

In the present work we intended to study the growth of instabilities and the evolution of the post-collision composite gas body. The key findings of this research and some of its limitations have been recorded in §5.4 above. Below I discuss an outline of a more complete treatment of the problem. Our simulations have shown that ram pressure confined gas slabs, evolve through a complex interplay between the gravitational instability and the shearing instabilities. Growth of either instabilities produces structure in the gas slab.

The nature of fragmentation of the gas slab slab depends on the relative dominance of the two instabilities. Although we have tried to establish the conditions under which each one of the two instabilities dominate however, our treatment of the problem is simplified. Firstly, our simulations are purely hydrodynamical as magnetic forces have been left out. Secondly, the treatment of relevant thermal physics in the problem has been simplified. We have used a barotropic EOS in all our simulations. Using this EOS, we have attempted to treat the radiative cooling of the post collision gas slab instead of using a detailed scheme attempting to model cooling through molecular or atomic transitions. We need to improve our simulations on both accounts.

Relative importance of the magnetic field : The Virial analysis of equilibrium structures has shown that along with internal turbulence, the mag-

netic field also plays an important role in supporting against self gravity (Chandrasekhar & Fermi 1953). Gas clouds in galactic arms are threaded by the ambient magnetic field. Just as turbulent motion under thermal pressure produces sound waves likewise, Alfvèn waves and other magneto-hydrodynamic waves pervade magnetised gas. Structure formation in the local universe is the result of complex gas dynamics. Gas density is enhanced through several orders of magnitude within self gravitating molecular clouds or in regions undergoing violent evolution. Star formation may commence in sufficiently dense regions (Elmegreen 2007).

Turbulent motion within the cloud interiors leads to dissipation of mechanical energy through internal shocking. Colliding fluid flows produce ram pressure confined gas slabs (Klessen & Burkert 2000). This type of a slab evolves in the same way as that produced in a cloud-cloud collision. The effect of magnetic field on the growth of these instabilities needs to be studied. We can also follow the changes in orientation of the ambient magnetic field as the underlying density structure evolves. **This will enable us to study the role of magnetic field on further evolution of the density structure.**

Two models have been proposed to explain how gravitational collapse is triggered in equilibrium clouds

1. Collapse induced by internal turbulent motion.
2. Collapse triggered by ambipolar diffusion.

It is essential to study for instance, how the magnetic field configuration evolves within a collapsing cloud. Theoretical and numerical investigations (e.g. Larson 1985; Price & Bate 2007) have shown that a collapsing magnetised cloud forms an hour glass structure when the magnetic field is parallel to the axis of the collapsing cloud. This is a large scale picture about a global collapse however, the orientation of local magnetic field with density sub structure within a collapsing cloud is unclear. **We need to investigate this so that we can ascertain the effect of magnetic field on the further evolution of this substructure.**

Observations in this regard have been inconclusive. For instance, the magnetic field is oriented orthogonal to the Pipe nebula (Alves *et al* 2008) while it is parallel to the Orion Integral Filament (OIF) (Matthews & Wilson 2000). It might be possible to explain these seemingly conflicting observations with the help of numerical simulations. **It is therefore my primary**

interest to include magnetic field in these simulations. This will enable us to study two related issues :

1. The effect of magnetic field on the growth of instabilities in either type of gas slabs mentioned above. In particular, I would like to see if the magnetic field has any influence on the growth of instabilities.
2. The relative orientation of local magnetic field with the underlying density structure, especially the elongated structure.

Numerical investigation will also cast some light on clump formation within the filament (*c.f.* Banerjee, Pudritz & Anderson 2006; Anathpindika 2008; Lefloch, Cernicharo & Pardo 2008). There have been other related studies in this direction but do not seem to suggest a strong correlation, apart from the fact that fragmentation of gas slabs produced structure (Passot, Vàzquez-Semadeni & Pouquet 1995; Basu, Ciolek & Wurster 2008). However, the nature of instabilities leading to fragmentation and the influence of magnetic field upon them seems to have been neglected.

A full SPMHD simulation might permit us to follow the magnetic field orientation up to the clump formation stage. In two of our cloud collision simulations, we could follow the fragmentation of the pressure compressed gas slab till the clumps (fragments) became self gravitating and formed protostellar cores in them (*modelled by sink particles, sink density* $= 10^{-12}$ $g\ cm^{-3}$). By implementing a radiative transfer scheme these self gravitating clumps can be allowed to evolve further, when they might contain several cores. Formation of multiple cores precludes the birth of a star cluster.

The following is an outline of the proposed investigation :

1. Repeat the high velocity head-on and off-centre cloud collision experiments (Anathpindika 2008, I) starting with magnetised individual clouds. We would like to determine the preferential orientation of the magnetic field relative to the underlying density structures. Also we will study the effect of magnetic field on development of various shearing instabilities within the shocked slab, notably the non-linear thin shell instability (NTSI). In particular, we would like to see if the magnetic field acts so as to damp the NTSI, through the suppression of perturbations on the post-collision shocked slab.
2. Repeat the low velocity head-on and off-centre cloud collision experiments (Chapman *et al* 1992; Anathpindika 2008, II), starting with

magnetised individual clouds. The aim is similar to that in the case above (see point 1). In the present case however, we would like to see the effect of magnetic field on the growth of gravitational instability.

3. Structure formation within magnetised GMCs through collision between turbulent fluid flows (Klessen & Burkert 2000).

4. We propose a simple model of a non-rotating isothermal cylinder for a filament, with a density falling off as r^{-2}, r being the radial distance measured from the axis of the cylinder. We then would like to study the gravo-thermal fragmentation of this filament with the magnetic field first, parallel to the cylinder axis and then perpendicular to the cylinder axis. The calculations to be then repeated for rotating filaments. We would then compare the results of fragmentation with analytical predictions e.g. Chandrasekhar & Fermi (1953); Ostriker (1964). We would like to compare the star formation efficiency of the two cases.

5. To study separately, the global collapse of magnetised cores with the magnetic field oriented parallel and orthogonal respectively, to the cloud axis. These respective cases will then be repeated for rotating and non-rotating clouds (*c.f.* Attwood *et al* 2008; Dobbs, Bonnell & Clark 2005; Crutcher & Hakobian 2008).

6. To study the alignment of circumstellar disks with filamentary regions. The findings of a statistical survey of nearby star forming regions by Anathpindika & Whitworth (2008) are in agreement with the findings of Chapman *et al* (1992). These findings however, are in contradiction with those of the present work (Anathpindika 2008 II). We would like to further investigate the subject and also try to ascertain the effect of magnetic field. This is in conjunction with points 1, 2 and 3 above.

Appendix A

The General Lane-Emden Equation

Let us now obtain the general form of Lane - Emden equation. As before, let $\phi(r)$ be the gravitational potential. It satisfies the Poisson's equation, so that we have

$$\nabla^2\phi(r) = -4\pi G\rho(r). \tag{A.1}$$

Since there is azimuthal and poloidal symmetry, it is sufficient to consider the radial component alone of Equation (A.1). Thus we have

$$\frac{1}{r^2}\frac{d}{dr}\Big(r^2\frac{d\phi}{dr}\Big) = 4\pi G\rho. \tag{A.2}$$

Equation (2.12) above, is the condition for a cloud to be in hydrostatic equilibrium. The pressure and density are related by the general barotropic equation of state,

$$P = K\rho^{\gamma}, \tag{A.3}$$

where all symbols have their usual meanings. Using Equation (A.3) in (2.12) we get,

$$\frac{d\phi(r)}{dr} = -K\gamma\rho^{\gamma-2}\frac{d\rho(r)}{dr} \tag{A.4}$$

Integrating this equation with respect to r we get,

$$\Rightarrow \phi(r) = \frac{-\gamma K\rho^{\gamma-1}}{(\gamma-1)}. \tag{A.5}$$

$$\Rightarrow \rho(r) = \Big[-\frac{\phi(r)}{(n+1)K}\Big]^n. \tag{A.6}$$

Equation (A.6) is obtained by a simple rearrangement of Equation (A.5) and by using the fact that $\gamma = 1 + \frac{1}{n}$, n being the polytropic index. Now, substituting Equation (A.6) in to Equation (A.2) above and simplifying it further we get,

$$\frac{d^2\phi(r)}{dr^2} + \frac{2}{r}\frac{d\phi(r)}{dr} = -4\pi G\Big(-\frac{\phi(r)}{(n+1)K}\Big)^n. \tag{A.7}$$

This above equation can be recast in terms of the dimensionless radius ξ, defined as $\xi = \frac{r}{R_0}$; R_0 is a physical distance scaling variable defined by Equation (A.8) below,

$$R_0^{-2} = \frac{4\pi G}{(n+1)^n K^n} \cdot (-\phi_c)^{n-1} = \frac{4\pi G}{(n+1)K} \cdot \rho_c^{\frac{n-1}{n}} \tag{A.8}$$

Where, in general $\phi(0) = \phi_c$, the central potential, correspondingly, $\rho = \rho_c$ at the centre. The Lane - Emden function, $\psi = \frac{\phi}{\phi_c} = \left(\frac{\rho}{\rho_c}\right)^{\frac{1}{n}}$. Substituting it in Equation (A.7) above and simplifying it further we get,

$$\frac{d^2\psi}{d\xi^2} + \frac{2}{\xi}\frac{d\psi}{d\xi} + \psi^n = 0. \tag{A.9}$$

This equation can then be recast as,

$$\frac{1}{\xi^2}\frac{d}{d\xi}\Big(\xi^2\frac{d\psi}{d\xi}\Big) + \psi^n = 0. \tag{A.10}$$

This is the general form of the Lane - Emden equation for an arbitrary polytropic index n.

Appendix B

Outflows And Their Association With Filamentary Star Forming Regions

B.1 Introduction :

Matter within GMCs is highly unevenly distributed. Some regions are much more dense than others and substructure within MCs often appears filamentary. Usually protostars form in these filamentary structures, see for instance Schneider & Elmegreen (1979), Hatchell *et al* (2005), Johnstone & Bally (2006). The implication is that a collapsing protostellar core is fed with material flowing along a filament. This highly anisotropic inflow may then have consequences for the dynamics of core collapse and fragmentation. In particular, the net angular momentum of the inflowing matter will strongly influence the orientation of binary orbits and circumstellar disks in the small-N subcluster of protostars forming in a prestellar core.

The orientations of protostellar disks around YSOs, in their early stages of evolution (class 0 & class I), can be inferred from the directions of the outflows which they drive (Ward-Thompson *et al.*, 2007). An outflow is presumed to be driven by the magnetohydrodynamic forces acting on circumstellar material. The outflow therefore, should be approximately parallel

to the rotation axis of the protostellar disk which is also the direction of the angular momentum vector of the material accreted from the natal prestellar core.

It therefore goes without saying that, the orientation of an outflow relative to the filament which feeds the birth of the driving YSO, may cast some light on the dynamics of core formation. In particular, (under the assumption that the inflow feeding the collapsing protostellar core) this constrains the relationship between the inflow feeding the protostellar core and the angular momentum transported by this material. This latter statement is made under the assumption that the outflow is driven along the direction of the angular momentum vector. Using this information we can discriminate between various core formation mechanisms (e.g. Whitworth *et al.* 1995, Banerjee, Pudritz & Anderson 2006, Banerjee & Pudritz 2007).

We note two possible core forming mechanisms viz. (a) gravitational fragmentation of a pressure compressed layer (Whitworth *et al.* 1995) and (b) gravoturbulent fragmentation of a magnetised medium (Banerjee, Pudritz & Anderson 2006, Banerjee & Pudritz 2007). To investigate into these possibilities, we surveyed five filamentary star forming regions. The findings of our survey suggest that the first mechanism is more likely to produce the observed distribution.

B.2 Distribution of the observed angle between the filaments & Outflows :

Let γ be the observed projected angle between the filament and an outflow, originating from a YSO embedded in it. In the current survey, we identified 45 YSOs lying in filaments. In Fig. (C.1) above, we present the histogram of measurements of this projected angle γ. The sources of raw data, the coordinates of YSOs and the HH objects corresponding to outflows driven by their respective sources and the recorded values of the orientation of filaments and outflows relative to local north, are tabulated in Table (C.2) below.

The snapshots of regions surveyed have been shown in Figs. (C.3) and (C.4). The observed filamentary regions have been marked by thick lines while the outflows from respective YSOs with rays in direction of the corresponding HH objects. The YSOs have been marked by circles. The top panel in Fig. (C.3) shows portions of the Orion Integral Filament (OIF). The second

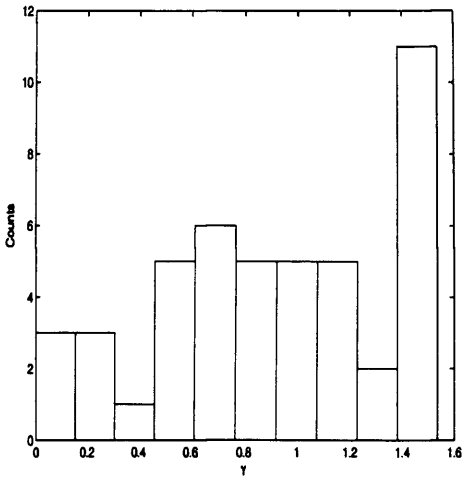

SS

Figure B.1: Histogram of the angle γ (in degrees). The bins on the γ axis are equispaced.

panel in Fig. (C.3) shows portion of the cloud L1688 in ρ - Ophiuchus (left hand) and the Serpens MC (right hand). The bottom panel in Fig. (C.3) shows the region L1524 (left hand) and portion of the region B18w in Taurus (right hand).

The top panel in Fig. (C.4) shows the other half of the region B18w in Taurus (left hand) and the region L1521 in Taurus (right hand). The second panel in Fig. (C.4) shows the Taurus Molecular Ring (left hand). The next three pictures after this one, show outflows from three sources in the nebula NGC 1333. They have been separately shown due to large multiplicity of outflows in the region.

B.2.1 Statistical Analysis :

A simple histogram of the angle γ shows that 28 out of 45 ($\sim$67 %) outflows are distributed within $\sim$45° of being orthogonal to filaments. The remaining 17 ($\sim$33 %) outflows are distributed within $\sim$ 45° of being parallel to filaments. To further interpret this observation, we allowed a truncated Gaussian distribution for the outflows about a direction orthogonal to the filament.

Let ψ be the intrinsic angle between the outflow & the normal to the filament and σ_ψ be the standard deviation of this truncated distribution. Note that $0 \leqq |\psi| \leqq \frac{\pi}{2}$. Next, we also assume that observed systems are randomly oriented along the observer's line of sight. Fig. (C.5) shows a schematic representation of this system. Under the assumptions set above, we performed 22,000 independent Monte Carlo realisations to generate random samples of the angle γ, each of size $N_s = 45$. If p_{γ_i} is the probability of the i^{th} measurement of the angle γ (γ_i), then the discrete cumulative distribution F_γ is defined as,

$$F_\gamma = \sum_{\gamma_i' < \gamma} p_{\gamma_i'}, \tag{B.1}$$

where $p_{\gamma_i'} = \frac{1}{N_s}, \forall \gamma_i'$ and $N_s = 45$, our sample size here.

We calculate F_γ for each randomly generated sample and then produce a smooth cumulative distribution (G_γ) by coaddition of these discrete distributions. We repeat this procedure for six different choices of σ_ψ viz. 0.1, 0.3, 0.5, 0.8, 1.5 and 5.0 (effectively means uniform distribution of outflows about the normal to the filament). We also try a distribution of outflows about the z axis with $\sigma_{\psi'} = 0.5$ (distribution of outflows about the filament). The respective cumulative distribution functions (G_γ) have been shown in Fig. (C.2). The discrete distribution function F_γ is plotted using red steps and for purpose of comparison, the distribution function, H_γ, for outflows strictly orthogonal to the filament ($\sigma_\psi = 0$) has also been plotted (green curve) in Fig. (C.2). The derivations for the distribution functions G_γ and H_γ are presented towards the end of this appendix.

We then performed the Kolgomorov - Smirnov (KS) test and the χ^2 test to determine the *goodness of fit* of the continuous distribution, G_γ, to the discrete distribution F_γ. In other words, we would like to determine the probability that F_γ belongs to the population generated by Monte - Carlo realisations for a specific choice of σ_ψ. This is called the significance level of a *goodness of fit* test.

At 5% significance level the distribution corresponding to $\sigma_\psi = 0.8$ is acceptable. Smaller values of σ_ψ like 0.1 or 0.2 yield a significance level <1% and hence, are rejected. The choice of the number of bins used in the χ^2 test for the present sample, does not seem to have any significant effect on the result of the test. On the other hand, the KS test on G_γ for $\sigma_\psi = 0.8$ yields a significance level between 5 & 10% while that for $\sigma_\psi = 0.5$ is just about 5 %. The KS test also rejects distributions for further smaller σ_ψ on grounds of poorer significance levels.

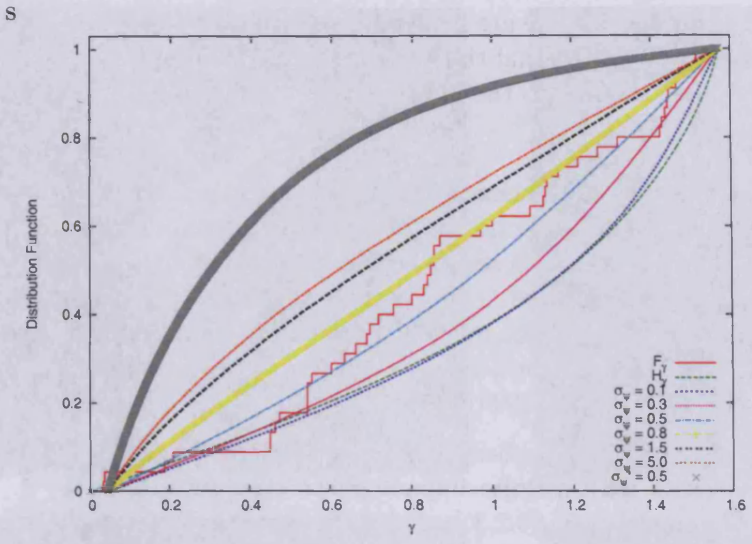

Figure B.2: Cumulative distribution function of the angle γ. Different curves here correspond to respective distribution of outflows about the y axis in Fig. (C.5). See text for more detail.

B.3 Discussion :

Our conclusion that outflows may be distributed about a direction orthogonal to the filament may suffer on two accounts. Firstly, the number of systems (filament - YSO - outflow) observed is too small and therefore statistically insignificant. Moreover they are located in only a few star forming regions. There is a possibility that outflows from a particular region are correlated due to for instance, common ambient environment like preferential confinement of the filament by external ram pressure and the large scale background magnetic field.

In this eventuality, our assumption that the observer's line of sight is randomly oriented, breaks down. It is therefore essential to expand the scope of the present survey to many more filamentary regions. Second, it is possible that the outflows oriented orthogonally to their filaments are easily detected than those which are parallel to the filament. It could be the case that outflows propagating parallel to the filament are inhibited by the density of matter within the filament, but on the other hand, this material could enhance visibility of the outflow by providing the necessary dissipative medium

(i.e. formation of the bow shock). We are inclined to accept this latter reasoning, in which case our conclusion that the outflows are distributed within $\sim 45°$ about a direction orthogonal to the filament is re emphasised.

Implications for core formation :

We have noted above two possible mechanisms of core formation and have been discussed in §5.2.3 above in connection with model 5 of our simulations. In light of our findings in this survey, it seems quite unlikely that these outflows are generated from YSOs located in filaments resulting from shocked slabs dominated by shearing flows. The more likely scenario is that of protostellar condensation in filaments formed in oblique pressure compressed slabs as shown by Whitworth *et al.* (1995).

Model 5 in our set of simulations, where MCs are allowed to collide at highly supersonic velocities with a finite impact parameter, resulted in a shock compressed oblique slab. In §5.2.3 and §5.2.4 we argued that such a slab is dominated by shearing instabilities and turbulent mixing between slab layers. As a result, growth of gravitational instability is suppressed and protostellar condensation is observed only after turbulence within the filament has sufficiently dissipated.

The resulting accretion disks are observed to be orthogonal to the filament. Similar conclusions were drawn by Banerjee, Pudritz & Anderson (2006) and Banerjee & Pudritz (2007). This scenario of protostellar core formation does not explain the inferences drawn from this survey over filamentary regions.

B.4 Data collation :

The systems analysed here are all nearby star forming regions. Firstly, we identified coordinates of the HH objects from the electronic catalogue compiled by Reipurth (1999). The coordinates of the YSOs driving the corresponding outflows were identified through a literature survey. In Table (C.1) we note the region surveyed in column 2 and the corresponding references in column 3.

We used sub mm continuum maps of the regions surveyed to locate YSOs and the HH objects. This enabled us to determine whether a YSO belonged to a filamentary region and the direction of the outflow relative to the local north (τ_{OF}). For this purpose we inherited SCUBA 850 μm sub mm continuum maps for the OIF from Nutter & Ward-Thompson (2007), the SCUBA

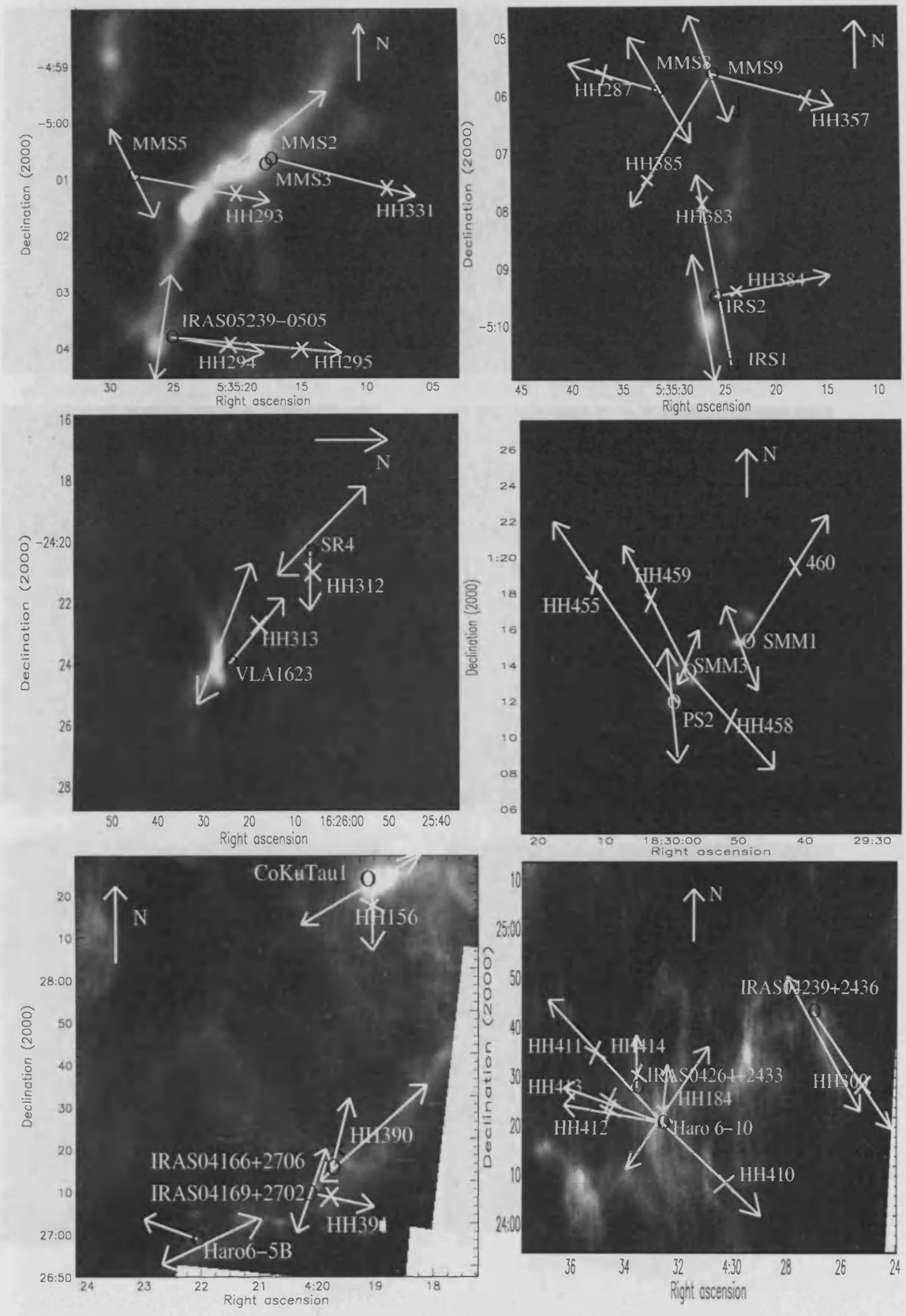
N
MMS5
MMS2
MMS3
HH293
HH331
IRAS05239−0505
HH294
HH295
Declination (2000)
Right ascension
MMS8
MMS9
HH287
HH357
HH385
HH383
HH384
IRS2
IRS1
SR4
HH312
HH313
VLA1623
HH459
HH455
460
SMM1
SMM3
PS2
HH458
CoKuTau1
HH156
HH390
IRAS04166+2706
IRAS04169+2702
HH391
Haro6−5B
IRAS04239+2436
HH411
HH414
IRAS04264+2433
HH184
HH412
Haro 6−10
HH410

Figure B.3:

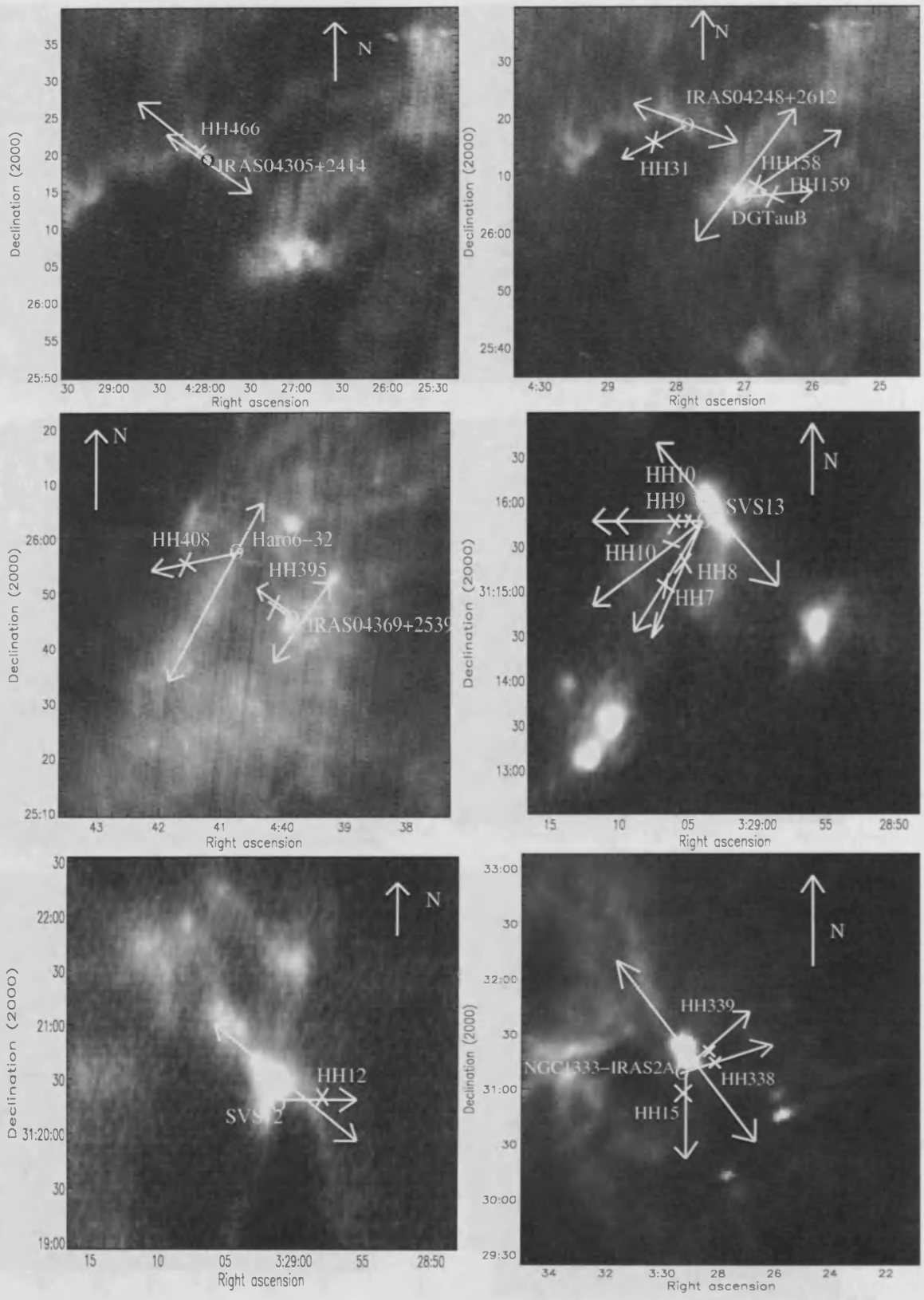
N
HH466
IRAS04305+2414
Declination (2000)
Right ascension
N
IRAS04248+2612
HH31
HH158
HH159
DGTauB
Declination (2000)
Right ascension
N
HH408
Haro6-32
HH395
IRAS04369+2539
Declination (2000)
Right ascension
N
HH10
HH9
SVS13
HH10
HH8
HH7
Declination (2000)
Right ascension
N
HH12
SVS12
Declination (2000)
Right ascension
N
HH339
NGC1333-IRAS2A
HH338
HH15
Declination (2000)
Right ascension

Figure B.4:

Table B.1: References for sub mm sources.

Serial number	Regions surveyed for sub mm sources	References
(i)	The OIF	Chini *et al* (1997); Yu *et al* (1997)
(ii)	ρ- Ophiuchus	Allen *et al* (2002)
(iii)	Serpens	Davis *et al* (1999)
(iv)	Taurus	Mundt & Freid (1983); Strom *et al* (1986); Strom & Strom (1994)
(v)	NGC 1333	Strom, Vrba & Strom (1976); Davis *et al.* (2008)

850 μm sub mm continuum maps from SCUBA archives for Serpens and ρ - Ophiuchus, SCUBA 450 μm sub mm continuum maps also from the SCUBA archives for NGC1333 (Di Francesco *et al.* 2008) and SPITZER 160 μm sub mm continuum maps for Taurus from Nutter *et al.* (2008).

We then employed the S(ource)extractor clump finding algorithm in the STARLINK software package to identify filamentary regions. This package requires two user defined parameters viz. the detection threshold and the isophotal radius. For a typical detection threshold (say 6σ), pixels in the continuum maps holding intensities greater than this threshold are detected. The isophotal radius (say 2) specifies the number of pixels to be grouped together for smoothing intensity magnitudes held by individual pixels of the map. Maxima in the map are fitted by elliptical isophots.

The inclination of the semi major axis of this ellipse with respect to the local north is the direction of the filament. Let τ_{Fil} be the angle made by the filament relative to the local north. The package works reasonably well since the identified regions are indeed filamentary as suggested by subjective viewing (by eye). However, if the detection threshold is made too small with the intention of identifying finer details in the filamentary structure, there is a possibility of it becoming smaller than the signal to noise ratio and the objects so detected are not those that are sought. In spite of the fact that the package fulfills our immediate requirements here, there could be discrepancies in it but attending to them should not dramatically alter our findings.

The projected angle between the outflow and the filament (γ) is then defined as,

$$\gamma = \min(|\tau_{OF} - \tau_{Fil}|, \pi - |\tau_{OF} - \tau_{Fil}|). \quad \text{(B.2)}$$

In the Table (C.2) we list the HH objects and their right ascension & de-

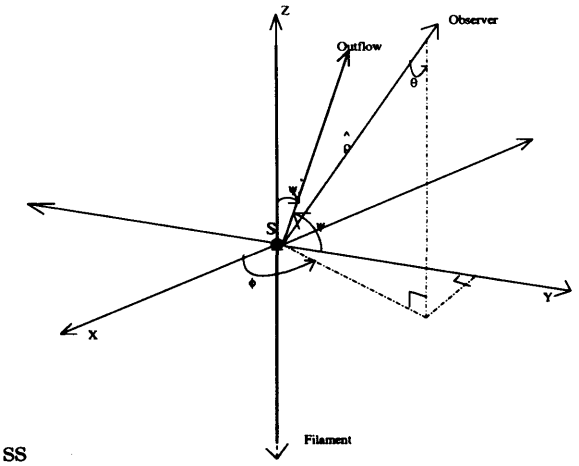

Figure B.5: Representation of the filament - outflow system in a cartesian coordinate frame, which here after, we refer to as the **system** frame. The angles $\theta, \phi \& \psi$ are defined in the text. The position of the observer is specified by the polar coordinates (ρ, θ, ϕ).

clinations in columns through 1 to 3, the YSOs and their right ascension & declinations in columns through 4 to 6, the respective references for YSO coordinates in column 7 and the angles τ_{OF}, τ_{Fil} & γ in columns through 8 to 10.

B.5 Derivation of the cumulative distribution Function :

In order to model the observed distribution of the projected angle γ, we consider a simplified system. We keep the direction of the filament fixed, let us say along the z axis and the outflows emerge along the normal to the z axis. Fig. (C.4) shows a schematic diagram of a single outflow - filament system. The outflow from a YSO (marked by a bark blob) is directed along the y axis. Additionally, polar coordinates (ρ, θ, ϕ) have been overlayed on this schematic diagram.

$\hat{\rho}$ is the unit vector in the direction of an observer located at a very large distance and (θ, ϕ) are the usual polar angles. ψ is the intrinsic angle between outflow and the normal to the filament, as has already been defined above.

Table B.2: Observational data (see text for details).

HH Obj			YSO				Angles		
Name	α_{2000}	δ_{2000}	Name	α_{2000}	δ_{2000}	Ref.	η_{OUT}	η_{FIL}	γ
Orion Integral Filament (SCUBA 850μm [1])									
HH287	05:35:41.55	-05:05:15.69	MMS8	05:35:38.36	-05:05:42.46	[2]	-60.8	-13.3	47.5
HH293	05:35:21.43	-05:01:15.09	MMS5	05:35:26.43	-05:01:14.45	[2]	90.5	-39.8	49.7
HH294	05:35:22.97	-05:04:02.20	IRAS 05329-0505	05:35:26.38	-05:03:53.45	[3]	99.7	12.8	86.9
HH295	05:35:16.07	-05:04:19.70	IRAS 05329-0505	05:35:26.38	-05:03:53.45	[3]	99.6	12.8	86.8
HH331	05:35:08.24	-05:00:48.13	MMS2	05:35:18.24	-05:00:34.86	[2]	95.1	46.6	48.5
HH357	05:35:16.04	-05:06:09.70	MMS9	05:35:25.95	-05:05:42.42	[2]	100.4	-53.0	26.6
HH383	05:35:26.40	-05:07:52.46	IRS1	05:35:24.55	-05:10:28.62	[4]	-5.6	-16.4	10.8
HH384	05:35:25.37	-05:09:23.38	IRS2	05:35:26.37	-05:09:25.75	[4]	81.0	-17.1	81.9
HH385	05:35:34.69	-05:07:20.19	MMS9	05:35:26.64	-05:05:42.27	[2]	-141.0	-52.9	88.1
ρ **Ophiuchus** (SCUBA 850μm [5])									
HH312	16:25:55.95	-24:20:46.97	SR4	16:25:56.48	-24:20:02.42	[6]	90.0	-32.7	57.3
HH313	16:26:18.82	-24:23:06.44	VLA1623	16:26:26.36	-24:24:30.94	[6]	27.0	64.9	37.9
Serpens (SCUBA 850μm [5])									
HH455	18:30:22.73	01:16:18.97	PS2	18:29:59.42	01:11:59.28	[7]	-55.5	-7.4	48.1
HH458	18:29:57.98	01:13:43.18	SMM3	18:29:59.18	01:13:58.26	[7]	132.5	15.2	62.7
HH459	18:30:02.56	01:14:44.51	SMM3	18:29:59.18	01:13:58.26	[7]	-49.4	15.2	64.6
HH460	18:29:38.59	01:18:23.78	SMM1	18:29:49.75	01:15:18.58	[7]	42.3	-41.7	84.0
ρ **L1524 (Taurus)** (SPITZER 160μm [8])									
HH156	04:18:51.54	28:20:28.14	CoKu Tau 1	04:18:51.60	28:20:28.14	[9]	180.0	25.9	25.9
HH157	04:22:00.89	26:57:37.61	Haro 6-5B	04:22:02.09	26:57:32.53	[10]	-76.1	76.7	27.2
HH390	04:19:40.85	27:15:52.86	IRAS04166+2706	04:19:43.00	27:13:34.00	[3]	02.6	43.7	41.1
HH391	04:19:56.32	27:09:25.84	IRAS04169+2702	04:19:59.20	27:09:59.00	[3]	95.0	39.4	55.6
B18w(Taurus) (SPITZER 160μm [8])									
HH184	04:29:23.66	24:33:01.44	Haro 6-10	04:29:23.86	24:32:57.03	[10]	02.6	45.8	43.2
HH300	04:25:23.04	24:23:20.11	IRAS04239+2436	04:26:57.10	24:43:36.00	[3]	139.4	-42.5	01.9
HH410	04:28:12.99	24:19:01.77	Haro 6-10	04:29:23.86	24:32:57.03	[10]	130.3	45.8	84.5
HH411	04:30:16.91	24:42:42.48	Haro 6-10	04:29:23.86	24:32:57.03	[3]	-51.8	45.8	82.4
HH412	04:29:52.97	24:37:10.08	Haro 6-10	04:29:23.86	24:32:57.03	[10]	-52.5	45.8	81.7
HH413	04:29:52.99	24:38:12.08	IRAS04264+2433	04:29:29.90	24:39:55.00	[3]	-51.5	45.8	82.7
HH414	04:29:30.31	24:39:53.60	IRAS04264+2433	04:29:29.90	24:39:55.00	[3]	0.0	45.8	45.8
HH466	04:33:35.42	24:21:32.09	IRAS04305+2414	04:33:33.80	24:21:09.00	[3]	-64.0	-66.1	02.1
L1521(Taurus) (SPITZER 160μm [8])									
HH158	04:27:04.65	26:06:16.40	DG Tau B	04:27:04.70	26:06:16.20	[11]	61.2	49.2	12.0
HH159	04:27:02.05	26:05:41.58	DG Tau B	04:27:04.70	26:06:16.20	[11]	85.6	49.2	36.4
HH31	04:28:18.39	26:17:40.49	IRAS04248+2612	04:27:57.12	26:19:17.00	[3]	-125.4	-85.8	39.6
TMC(Taurus) (SPITZER 160μm [8])									
HH395	04:40:08.73	25:46:44.44	IRAS04369+2539	04:39:58.48	25:45:06.13	[3]	-50.2	46.9	82.9
HH408	04:41:38.92	25:56:26.27	IRAS04385+2550	04:41:04.23	25:57:56.85	[3]	-103.8	-143.8	40.0
NGC1333 (SCUBA 450μm [5])									
HH7	03:29:07.99	31:15:28.47	SVS13	03:29:03.59	31:15:51.72	[12]	-113.7	-41.1	72.6
HH8	03:29:06.40	31:15:53.56	SVS13	03:29:03.59	31:15:51.72	[12]	-116.6	-41.1	75.5
HH9	03:29:06.19	31:15:37.57	SVS13	03:29:03.59	31:15:51.72	[12]	-89.9	-41.1	48.8
HH10	03:29:05.29	31:15:46.63	SVS13	03:29:03.59	31:15:51.72	[12]	-106.3	-41.1	65.2
HH11	03:29:04.49	31:15:53.67	SVS13	03:29:03.59	31:15:51.72	[12]	-89.9	-41.1	48.8
HH12	03:28:57.60	31:20:10.07	SVS12	03:29:01.67	31:20:06.84	[12]	90.0	-20.3	69.7
HH15	03:28:58.86	31:08:01.99	IRAS03255+3103	03:28:37.11	31:13:28.30	[12]	180.0	-58.8	58.8
HH338	03:28:12.82	31:19:43.63	IRAS03255+3103	03:28:37.11	31:13:28.30	[13]	56.3	-58.8	64.9
HH339	03:28:31.05	31:19:43.63	IRAS03255+3103	03:28:37.11	31:13:28.30	[13]	54.4	-58.8	66.8
HH340	03:28:44.94	31:05:38.79	IRAS03256+3055	03:28:45.31	31:05:41.90	[13]	180.0	-58.8	58.8
HH341	03:28:49.60	31:01:15.52	NGC1333-IRAS2A	03:28:55.59	31:14:37.50	[13]	180.0	-58.8	58.8
HH342	03:28:51.91	31:10:48.39	IRAS03256+3055	03:28:45.31	31:05:41.90	[13]	155.8	-58.8	34.6
HH343	03:28:54.40	31:05:21.25	IRAS03256+3055	03:28:45.31	31:05:41.90	[13]	180.0	-58.8	58.8

References. — [1] Nutter & Ward-Thompson (2007) [2] Chini *et al* (1997) [3] http://vizier.u-strasbg.fr/viz-bin/VizieR?-source=II/125 [4] Yu *et al* (1997) [5] Di Francesco *et al* (2008) [6] Allen *et al* (2002) [7] Davis *et al* (1999) [8] Nutter *et al* (2008) [9] Strom *et al* (1986) 10]Strom & Strom (1994) [11]Mundt & Fried (1983) [12]Strom *et al* (1976) [13]Davis *et al* (2008)

We assume that observers are isotropically distributed in space. The unit vector in direction of the supposed observer is,

$$\hat{\rho} = \sin\theta\cos\phi\hat{\mathbf{i}} + \sin\theta\sin\phi\hat{\mathbf{j}} + \cos\theta\hat{\mathbf{k}}. \tag{B.3}$$

The outflows essentially have only one degree of freedom. The unit vectors in direction of the filament and the outflow respectively, are

$$\hat{\mathbf{f}} = \hat{\mathbf{k}} \tag{B.4}$$

$$\hat{\mathbf{h}} = \cos\psi\hat{\mathbf{j}} + \sin\psi\hat{\mathbf{k}}, \tag{B.5}$$

To calculate the projected angle between the filament and outflow in the plane of the sky, we must employ a transformation from the system frame to the observer's frame of reference. For the purpose, we apply successive rotations, where the first rotation is about the z axis through angle ϕ and the second rotation is about the new y axis through angle θ. Let $(\mathbf{i}'', \mathbf{j}'', \mathbf{k}'')$ be the corresponding unit vectors in this transformed frame of reference. The transformed unit vectors of the filament and the outflow respectively are,

$$\hat{\mathbf{f}} = -\sin\theta\hat{\mathbf{i}}'' + \cos\theta\hat{\mathbf{k}}'' \tag{B.6}$$

$$\hat{\mathbf{h}} = \hat{\mathbf{i}}''(\cos\psi\cos\theta\sin\phi - \sin\psi\sin\theta) + \hat{\mathbf{j}}''(\cos\psi\cos\phi) + \hat{\mathbf{k}}''(\cos\psi\sin\theta\sin\phi + \sin\psi\cos\theta). \tag{B.7}$$

The respective unit vectors of the filament and the outflow on the observer's sky are then,

$$\hat{\mathbf{f}}^{Obs} = \frac{(\mathbf{f}\cdot\mathbf{i}'' + \mathbf{f}\cdot\mathbf{j}'')}{|\mathbf{f}\cdot\mathbf{i}'' + \mathbf{f}\cdot\mathbf{j}''|} = -\hat{\mathbf{i}}'' \tag{B.8}$$

and

$$\hat{\mathbf{h}}^{Obs} = \frac{(\mathbf{h}\cdot\mathbf{i}'' + \mathbf{h}\cdot\mathbf{j}'')}{|(\mathbf{h}\cdot\mathbf{i}'' + \mathbf{h}\cdot\mathbf{j}'')|}$$

$$= \frac{\hat{\mathbf{i}}''(\cos\psi\cos\theta\sin\phi - \sin\psi\sin\theta) + \hat{\mathbf{j}}''(\cos\psi\cos\phi)}{[\cos^2\psi(\cos^2\theta\sin^2\phi + \cos^2\phi) + \sin^2\theta\sin^2\psi - \frac{1}{2}\sin 2\theta\sin 2\psi\sin\phi]^{\frac{1}{2}}}. \tag{B.9}$$

The cosine of the projected angle between the filament and outflow is obtained from the usual definition of the scalar product as,

$$\cos\gamma = \frac{(\cos\psi\cos\theta\sin\phi - \sin\psi\sin\theta)}{[\cos^2\psi(\cos^2\theta\sin^2\phi + \cos^2\phi) + \sin^2\psi\sin^2\theta - \frac{1}{2}\sin 2\psi\sin 2\theta\sin\phi]^{\frac{1}{2}}}. \tag{B.10}$$

Due to the inherent symmetry of the problem, it is sufficient to consider θ and $\phi \in [0, \frac{\pi}{2}]$. The probability that θ and ϕ lie in the range $(\theta, \theta + d\theta)$ and $(\phi, \phi + d\phi)$ respectively, is $p_{\theta\phi}$ and,

$$p_{\theta\phi} d\theta d\phi = \sin\theta d\theta \cdot \frac{2d\phi}{\pi}, \tag{B.11}$$

where $d\theta$ and $d\phi$ are infinitesimally small intervals. We assume that the angle ψ is distributed according to the truncated Gaussian distribution about the y axis as,

$$p_\psi d\psi = \frac{C}{\sqrt{2\pi}\sigma_\psi} e^{\frac{-\psi^2}{2\sigma_\psi^2}} d\psi \tag{B.12}$$

and C is a normalisation constant defined as,

$$C = \frac{1}{\frac{1}{(2\pi)^{\frac{1}{2}}\sigma_\psi} \int_{\psi=-\frac{\pi}{2}}^{\psi=\frac{\pi}{2}} e^{\frac{-\psi^2}{2\sigma_\psi^2}} d\psi},$$

where all symbols have usual meanings.

The cumulative distribution of the projected angle γ is then obtained by the Monte - Carlo integration of the total probability $p_{\theta\phi} \cdot p_\psi$, for a particular choice of σ_ψ. The result of this integration is shown in Fig. (C.2) for various choices of σ_ψ. The angle $\psi' = \frac{\pi}{2} - \psi$, is the intrinsic angle between the filament and the outflow and $\sigma_{\psi'}$ is the standard deviation of the outflows about the filament. The curve plotted using silver crosses in Fig. (C.2) corresponds to $\sigma_{\psi'} = 0.5$ i.e. within $\sim 30°$ of being parallel to the filament. Clearly, it is a very bad fit to the cumulative distribution of the observed projected angle γ.

The special case :

As a special case we now set $\sigma_\psi = 0$ so that the outflow is always orthogonal to the filament. The unit vector $\hat{\mathbf{h}}$ of the outflow, is simply

$$\hat{\mathbf{h}} = \hat{\mathbf{j}}, \tag{B.13}$$

while of the filament is the same as defined by equation (C.4) above. After application of the rotational transformations described above, the unit vector $\hat{\mathbf{h}}$ becomes,

$$\hat{\mathbf{h}} = \cos\theta \sin\phi \hat{\mathbf{i}}'' + \cos\theta \hat{\mathbf{j}}'' + \sin\theta \sin\phi \hat{\mathbf{k}}'' \tag{B.14}$$

and that of the filament, $\hat{\mathbf{f}}$, is as that given by equation (C.6). The unit vector of the outflow on the observer's sky, $\hat{\mathbf{h}}^{Obs}$, can then be obtained as before so that,

$$\hat{\mathbf{h}}^{Obs} = \frac{\sin\phi\cos\theta\hat{\mathbf{i}}'' + \cos\phi\hat{\mathbf{j}}''}{[1-\sin^2\phi\sin^2\theta]^{\frac{1}{2}}} \tag{B.15}$$

and $\hat{\mathbf{f}}^{Obs}$, the unit vector of the filament on the observer's sky, is given by equation (C.8). The projected angle γ, between the filament and outflow is obtained from the usual scalar product of $\hat{\mathbf{h}}^{Obs}$ and $\hat{\mathbf{f}}^{Obs}$, so that

$$\cos\gamma = \frac{\sin\phi\cos\theta}{[1-\sin^2\phi\sin^2\theta]^{\frac{1}{2}}}. \tag{B.16}$$

Let us now define a function $\Gamma(\theta,\phi)$ as,

$$\Gamma(\theta,\phi) \equiv \cos\gamma = \frac{\sin\phi\cos\theta}{[1-\sin^2\phi\sin^2\theta]^{\frac{1}{2}}}. \tag{B.17}$$

Note that Eqn. (C.10) reduces to Eqn. (C.17) in the limit $\psi \rightarrow 0$.

The distribution function H_γ is obtained by integrating the probability density $p_{\theta\phi}$ defined by equation (C.11). We now obtain the limits for this integration. A simple rearrangement of equation (C.17) gives,

$$\cos\theta = \frac{\Gamma\cot\phi}{(1-\Gamma^2)^{\frac{1}{2}}}. \tag{B.18}$$

Observe that, when $\theta = 0$, $\Gamma = \sin\phi$, while when $\theta = \frac{\pi}{2}$, $\Gamma = 0$. Next, when $\phi = 0$, $\Gamma = 0$ and $\phi = \frac{\pi}{2}$, $\Gamma = 1$. Thus

$$\phi_{min} = \sin^{-1}(\Gamma)$$

and

$$\theta_{max} = \cos^{-1}\left[\frac{\Gamma\cot\phi}{(1-\Gamma^2)^{\frac{1}{2}}}\right].$$

Thus, the integration is now done over the intervals $(0,\theta_{max})$ and $(\phi_{min},\frac{\pi}{2})$,

$$H_\gamma = \int_{\phi_{min}}^{\frac{\pi}{2}}\int_0^{\theta_{max}} \sin\theta d\theta\frac{2d\phi}{\pi} \tag{B.19}$$

$$= \frac{2}{\pi}\int_{\theta_{min}}^{\frac{\pi}{2}}\left[1-\frac{\Gamma\cot\phi}{(1-\Gamma^2)^{\frac{1}{2}}}\right]d\phi$$

$$= \frac{2}{\pi}\left[\phi - \frac{\Gamma \ln|\sin\phi|}{(1-\Gamma^2)^{\frac{1}{2}}}\right]_{\phi_{min}}^{\frac{\pi}{2}}$$

$$= 1 - \frac{2}{\pi}\left[\sin^{-1}(\Gamma) - \frac{\Gamma \ln(\Gamma)}{(1-\Gamma^2)^{\frac{1}{2}}}\right],$$

where the limiting value $\Gamma = \sin\phi$, for $\theta = 0$ has been used. From Eqn. (C.17) it follows that $\sin^{-1}\Gamma = \frac{\pi}{2} - \gamma$. The expression for H_γ can then be simplified to

$$H_\gamma = \frac{2}{\pi}\Big[\gamma + \cot\gamma \cdot \ln(\cos\gamma)\Big]. \tag{B.20}$$

The cumulative distribution, H_γ, has been plotted using the green dashed curve in Fig. (C.2), which obviously, is in poor agreement with the observed cumulative distribution.

Bibliography

[1] Agertz *et al* : *Fundamental Differences Between SPH And Grid Methods*; MNRAS 380 : 963 - 78 (2007)

[2] Allen *et al* : *Physical Properties Of Molecular Clouds In The Disk Of M31*; ApJ 444 : 157 - 64 (1995)

[3] Alves *et al* : *Correlation Between Gas And Dust In Molecular Clouds: L977*; ApJ 515 : 265 - 274 (1999)

[4] Alves, J., Lombardi, M., & Lada, C. : *The Mass Function Of Dense Molecular Cores & Origin Of The IMF*; AA 462 : L17 - L21 (2007)

[5] Alves, J., Franco, G. & Girart, J : *Optical Polarimetry Toward The Pipe Nebula : Revealing The Importance Magnetic Field* AA 487 : 605 (2008)

[6] Anathpindika, S & Whitworth, A. : *Outflows and Their Association With Filamentary ...*; AA 487 : 605 - 10 (2008)

[7] Anathpindika, S. : *Supersonic Cloud Collision - I* arxiv 0810.5011 (2008) (MNRAS submitted)

[8] Anathpindika, S. : *Supersonic Cloud Collision - II* under preparation

[9] Andrè, P., Ward-Thompson, D. & Barsony, M. : *Sub mm continuum observations of ρ Oph: ...*; ApJ 406 : 122 - 41 (1993)

[10] Attwood, R., Goodwin, S. & Whitworth, A. : *Adaptive Smoothing Lengths In SPH*; AA 464 : 447 - 50 (2007)

[11] Balsara. D. : *von Neumann Stability Analysis of SPH ...*; Jour. comp. Phy. 121: 357 - 372 (1995)

[12] Banerjee, R., Pudritz, R. E., Anderson, D. W. : *Supersonic Turbulence, Filamentary Accretion And The Rapid Assembly Of Stars & Disks*; MNRAS 373 : 1091 - 1106 (2006)

[13] Barnes, J & Hut, P. : *A Hierarchical O(N log N) Force-Calculation Algorithm*; Nature 324 : 446 - 49 (1986)

[14] Barnes, J & Hut, P. : *Error Analysis Of A Tree Code* ; ApJSS 70 : 389 - 417 (1989)

[15] Bash, F., Hausman, M & Papaloizou, J. : *A Turbulent Model For GMCs*; ApJ 245 : 92 - 98 (1981)

[16] Basu, S., Ciolek, G & Wurster, J. : *Magnetically-Regulated Fragmentation Induced by Nonlinear Flows and Ambipolar Diffusion* arXiv 0806.2482 (2008)

[17] Bate, M., Bonell, I. & Price, N. : *Modelling Accretion In Protobinary Systems*; MNRAS 277 : 362 - 76 (1995)

[18] Bhattal, A., Francis, N., Watkins, S & Whitworth, A. : *Dynamically triggered star formation in giant molecular clouds* MNRAS 297: 435 - 48 (1998)

[19] Binney, J & Tremaine, S. : *Galactic Dynamics* ; Princeton series in Astrophysics, edn. 3 (1994)

[20] Binney, J., Dehnen, W & Bertelli, G. : *The Age Of Solar Neighbourhood* ; MNRAS 318 : 3, 658 - 64 (2000)

[21] Blitz. L. : *The Physics Of Star Formation And Stellar Evolution*; Kluwer Pub.(1990)

[22] Blondin, J & Marks, B. : *Eolution Of Cold Shock Bounded Slabs*; New Astronomy 1(3): 235 - 44 (1996)

[23] Bonnor. W. : *Boyle's Law And Gravitational Instability*; MNRAS 116: 351- 59 (1956)

[24] Bonnor. W. : *Stability Of Polytropic Gas Spheres*; MNRAS 118: 523- 27 (1958)

[25] Bonnell *et al* : *Fragmentation Of Cylindrical Elongated Clouds III - Formation Of Binary & Multiple Systems*; ApJ 377: 553 - 58 (1991)

[26] Bonnell, I., Bate, M., Clarke, C & Pringle, J. : *Accretion And Stellar Mass Spectrum In Small Clusters*; MNRAS 285: 201 - 08 (1997)

[27] Bonnell, I., Bate, M., Clarke, C & Pringle, J. : *Competative Accretion In Embedded Stellar Clusters*; MNRAS 323: 785 - 94 (2001 a)

[28] Bonnell, I., Bate, M., Clarke, C & Pringle, J. : *Accretion In Stellar Clusters & The IMF*; MNRAS 324: 573 - 79 (2001 b)

[29] Bonnell, I., Vine, S & Bate, M.: *Massive Star Formation: Nurture, Not Nature*; MNRAS 349: 735 - 49 (2004)

[30] Bonnell, I., Clarke, C & Bate, M. : *The Jeans Mass & The Origin Of The Knee In The IMF*; MNRAS 368: 1296 - 1300 (2006)

[31] Bonnell, I & Bate, M. : *Star Formation Through ravitational Collapse And Competative Accretion*; MNRAS 370: 488 - 94 (2006)

[32] Bok, B. : In Centinnial symposia, Harvard Observatory Monographs. (Cambridge: Harvard)

[33] Boss, A & Black, D. : *Collapse Of Accreting, Rotating, Isothermal Interstellar Clouds*; ApJ 258: 270 - 79 (1982)

[34] Boyd, D & Whitworth, A. : *The Minimum Mass For Opacity-limited Fragmentation In Turbulent Cloud Cores*; A & A 430: 1059 - 66 (2005)

[35] Broderick, T., Keto, E., Lada, C & Narayan, R. : *Oscillating Starless Cores: Nonlinear ...*; ApJ 671: 1832 - 38 (2007)

[36] Carr. J. : *Study Of Clumping In The Cepheus OB3 Molecular Cloud*; ApJ 323: 170 - 78 (1987)

[37] Clark, C., Bonnell, I & Hillenbrand, L. : *The Formation of Stellar Clusters*; Protostars and Planets IV, University of Arizona Press; eds. Mannings, V., Boss, A., Russell, S., p. 151 (2000)

[38] Clark, P., Klessen, R. & Bonnell, I. : *Clump Lifetimes And The Initial Mass Function*; MNRAS 379: 57 - 62 (2007)

[39] Chabrier. G. : *Galactic Stellar & Substellar IMF*; PASP 115: 763 - 95 (2003)

[40] Chabrier. G. : *Galactic Mass Function: ...*; ApJ 586: L133 - L136 (2003)

[41] Chandrasekar. S. : *An Introduction To The Study Of Stellar Structure*; Dover Pub. (1939)

[42] Chandrasekar, S & Fermi, E. : *Problems Of Gravitational Stability In The Presence Of Magnetic Field*; ApJ 118: 116 - 41 (1953)

[43] Chandrasekhar. S. : *Problems Of Stability In Hydrodynamics And Hydromagnetics*; MNRAS 113: 667 - 78 (1953)

[44] Chandrasekhar. S. : *Hydrodynamic and Hydromagnetic Stability*; Oxford Clarendon Press (1962)

[45] Chapman *et al* : *The Formation Of Binary And Multiple Star Systems*; Nature 359: 207 - 210 (1992)

[46] Chini *et al* : *Dust Filaments And Star Formation In OMC2 And OMC3*; ApJ 474: L135 - 38 (1997)

[47] Clark, C. : *The Fragmentation Of Cold slabs: Application To The Formation Of Clusters* MNRAS 307, 328 - 36 (1999)

[48] Clark, P., Klessen, R & Bonnell, I.: *Clump Life Time & The IMF*; MNRAS 379: 57 - 62 (2007)

[49] Courant, R & Friedrichs, K.: *Supersonic Flow And Shock Waves*; Springer- Verlag Pub.

[50] Commercon *et al*: *Protostellar Collapse: A Comparison Between Smoothed Particle Hydrodynamics And Adaptative Mesh Refinement Calculations*; A & A 482: 371 - 85 (2008)

[51] Crutcher, R & Hakobian, N. : *Testing Magnetic Star Formation Theory*; arXiv 0807.2862v2 (2008)

[52] Dale, J., Bonnell, I. & Whitworth, A. : emphIonization-induced Star Formation - I. The Collect-and-collapse Model; MNRAS 375: 1291 - 98 (2007)

[53] Dale, J., Clark, P & Bonnell, I. : *Ionization-induced star formation - II. External irradiation of a turbulent molecular cloud* MNRAS 377: 535 - 44

[54] Dehnen. W. : *Towards Optimal Softening In N- Body Codes- I. Minimising The Force Error*; MNRAS 324:273 - 91 (2001)

[55] Dickey, J & Garwood, R. : *The mass spectrum of interstellar clouds*; ApJ 319: 201 - 07 (1989)

[56] Disney, M. : *Boundary And Initial Conditions In Protostar Calculations*; MNRAS 175: 323 - 33 (1976)

[57] Dobbs, C., Bonnell, I & Clark, P.: *Centrally Condensed Massive Cores: Massive Stars Or Fragmentation*; MNRAS, 360, 2 - 8 (2005)

[58] Elmegreen, B & Elmegreen, D. : *Star Formation In Shock Compressed Layers*; ApJ 220: 1051 - 62 (1978)

[59] Elmegreen. B.. : *A Pressure And Metallicity Dependence For Molecular Cloud Correlations And The Caliberations Of Mass*; ApJ 338; 178 - 96 (1989)

[60] Elmegreen, B. : *On The Gravitational Collapse Of Decelarated Shocked Layers In Young OB Associations*; ApJ 340; 786 - 811 (1989)

[61] Elmegreen, B. : *Fragmentation Of Molecular Clouds And Star Formation*; 147th IAU Proceedings (1991)

[62] Elmegreen. B. : *The H To H_2 Transition In Galaxies: Totally Molecular Galxies*; ApJ 411: 170 - 177 (1993)

[63] Elmegreen, B & Flagrone, E. : *A Fractal Origin For The Mass Spectrum Of Interstellar Clouds*; ApJ 471: 816 - 21 (1996)

[64] Elmegreen. B. : *Intercloud Structure In A Turbulent Fractal ISM*; ApJ 477: 196- 203 (1997)

[65] Elmegreen. B. : *Phase And Structures Of Interstellar Gas*; The Physics and Chemistry of the ISM, GCA- Verlag Herdecke 1999, 77- 91

[66] Elmegreen, B. : IAU Symposium Series, *Extragalactic Star Clusters*, Vol. 207, Eds. Geisler, D., Grebel, E & Minniti, D. (2002)

[67] Elmegreen, B. : *On The Rapid Collapse And Evolution Of Molecular Clouds*; ApJ 668: 1064 - 82 (2007)

[68] Field, G., Blackman, E & Keto, E.: *A Model Of Cloud Fragmentation*; MNRAS 385: 181 - 88 (2008)

[69] Fleck. R. (Jr): *Interstellar Cloud Shapes : A Minimum Hypothesis Account Involving Purely Gravitational Effect*; ApJ 401: 146 - 49 (1992)

[70] Fleck. R. (Jr): *Scaling Relations For Turbulent, Non Self Gravitating, Neutral Component Of The ISM* ; ApJ 458: 739 - 41 (1996)

[71] Falconer. K. : *Fractal Geometry: Mathematical Foundations And Applications* ; John Wiley Pub. Inc, chapter 1 (1997)

[72] Fletcher. C. : *Computational Techniques For Fluid Dynamics 1*; Springer- Verlag Pub.

[73] Gingold, R & Monaghan, J. : *Smoothed Particle Hydrodynamics: Theory And Application To Non Spherical Stars* ; MNRAS 181: 375 - 89 (1977)

[74] Goodwin. S. : *Simulating Star Formation In Molecular Cloud Cores 1*; AA 414: 633 - 50 (2004)

[75] Goodwin. S. : *The Rleationship Between The Prestellar CMF & The Stellar IMF*; AA 477: 823 - 27 (2008)

[76] Hatchell *et al* : *Star Formation In Persues. Clusters, Filaments and Initial Conditions For Star Formation*; AA 440: 151 - 61 (2005)

[77] Han, Z & Zhang, F. : *The Galactic Distribution Of Magnetic Fields In Molecular Clouds And HII Regions*; AA 464: 609 - 14 (2007)

[78] Hausman. M. : *Collisional Mergers & Fragmentation Of Interstellar Clouds*; ApJ 245: 72 (1981)

[79] Heitsch *et al* : *The Birth Of Molecular Clouds : Formation Of Atomic Precursors In Colliding Flows*; ApJ 648: 1052 - 65 (2006)

[80] Heitsch *et al* : *Cooling, Gravity, and Geometry: Flow-driven Massive Core Formation*; ApJ 674: 316 - 28 (2008)

[81] Henrici. P. : *Discrete Variable Methods In ODEs*; John Wiley Inc. (1962)

[82] Hernquist. L. : *Performance Charecteristics Of Tree Codes* ; ApJSS 64: 715 - 34 (1987)

[83] Hernquist, L & Katz, N. : *Tree SPH- A Unification Of SPH With Hierarchal Tree Method*; APJ 70: 419 - 46 (1989)

[84] Hernquist, L & Barnes, J. : *Are Some N- body Algorithms Intrinsically Less Collisional Than Others* ; ApJ 349: 562 - 69 (1990)

[85] Hockney, R & Eastwood, J. : *Computer Simulations Using Particles*; IOP pub. (1988).

[86] Hollenbach, D., Takahashi, T & Tielens, A.: *Low - Density Photodissociation Regions* ; ApJ 377: 192 - 209 (1991)

[87] Hoyle, F. : *On the Fragmentation of Gas Clouds Into Galaxies and Stars*; ApJ 118, 513 - 28

[88] Hubber, D., Goodwin, S & Whitworth, A. : *Resolution Requirements For Simulating Gravitational Fragments Using SPH*; AA 4100 (2006).

[89] Hunt-Cunningham, M., Whiteoak, J & Priestly, P. : *Massive Star Formation From Colliding Molecular Clouds*; Astronomical Soc. Of Japan, 145 (2002)

[90] Hunter. C. : *The Instability Of The Collapse Of A Self Gravitating Gas Cloud*; ApJ 136: 594 - 608, (1962)

[91] Hunter. C. : *The Development Of Gravitational Instability In A Self Gravitating Gas Cloud*; ApJ 139: 570 - 86 (1964)

[92] Hunter (Jr), J & Fleck (Jr), R.: *Star Formation: The Influence Of Velocity Fields And Turbulence*; ApJ 256: 505 - 13 (1982).

[93] Hunter(Jr), J & Klien, R. : *Star Formation In Colliding Gas Flows*; ApJ 305: 309 - 32 (1986)

[94] Johnstone, D & Bally, J. : *JCMT/SCUBA Submm Wavelength Imaging Of The Integral Shaped Filament In Orion*; ApJ 510: L49 - L53 (1999)

[95] Kaplan. S. : *Interstellar Gas Dynamics* 2^{nd} edition. Oxford Pergamon Press, chapter 3 (1966)

[96] Keto, E., Broderick, A., Lada, C & Narayan, R. : *Oscillations Of Starless Cores*; ApJ 652: 1366 - 73 (2006)

[97] Kippenhahn, R & Weigert, A. : *Stellar Structure And Evolution*; Springer- Verlag Pub chapter 26 (1991)

[98] Kittel. C. : *Fundamentals Of Solid State Physics*; John Wiley Inc, chapter 1 (2005)

[99] Klein, R & Woods, D. : *Bending mode instabilities and fragmentation of interstellar cloud collisions*; ApJ 497: 777 - 799 (1998)

[100] Klessen, R., Burkert, A & Bate, M. : *Fragmentation of Molecular Clouds: The Initial Phase of a Stellar Cluster*; ApJ 501: L205 - 08 (1998)

[101] Klessen, R & Burkert, A. : *The Formation Of Stellar Clusters: Gaussian Cloud Conditions I*; ApJSS 128: 287 - 319 (2000)

[102] Koyama, H & Inutsuka, S. : *Molecular Cloud Formation In Shock-Compressed Layers*; ApJ, 532, 980 - 93 (2000)

[103] Kroupa. P. : *The Variation Of the IMF*; MNRAS 322: 231 - 46 (2001)

[104] Kroupa, P., Aarseth, S & Hurley, J. : *The Formation Of A Bound Star Cluster: From The Orion Nebula Cluster To The Pleiades* ; MNRAS 312: 4, 699 - 712 (2001)

[105] Kroupa. P. : *The IMF of stars: Evidence For Uniformity In Variable Systems*; Science 295: 82 - 91 (2002)

[106] Krumholz, M., McKee, C & Richard, K.: *The Formation Of Stars By Gravitational Collapse Rather Than Competative Accretion*; Nature 438: 332 (2005)

[107] Krumholz *et al*: *How Protostellar Outflows Help Massive Stars Form* ; ApJ 618: L33 - L36 (2005)

[108] Krumholz, M & Tan, J. : *Slow Star Formation In Dense Gas: Evidence and Implications*; ApJ 654: 304 - 15 (2007)

[109] Lada. C. : *Dust Extinction And Molecular Gas In The Dark Cloud IC 5146*; ApJ 429: 694 - 709 (1994)

[110] Lada *et al*: *Physical Properties Of Molecular Cloud Cores In L1630 And Implications On Star Formation*; ApJ 488: 286 - 306 (1997)

[111] Lada, C., Alves, F. & Lada, B. : *Infrared Extinction And The Structure Of The IC 5146 Dark Cloud*; A & A 512: 250 - 59 (1999)

[112] Lada *et al*: *The Dynamical State Of B68: ...*; ApJ 586: 286 - 95 (2003)

[113] Lada, C., Muench, A., Rathborne, J., Alves, J & Lombardi, M. : *The Nature Of Dense Core Population In The Pipe Nebula : Thermal Cores Under Pressure*; ApJ 672: 410 - 22 (2008)

[114] Landau, L & Lifschitz, D. : *Course In Theoretical Physics* ; Vol. 6, Pergamon Press, chapters 9 & 10 (1966).

[115] Larson. R. : *Numerical Calculations Of The Dynamics Of Collapsing Protostar*; MNRAS 145: 271 - 95 (1969)

[116] Larson. R. : *Turbulence And Star Formation In Molecular Clouds*; MNRAS 194: 809 - 26 (1981)

[117] Larson. R. : *Understanding The IMF*; astroph/ 0406624v2 (2004)

[118] Larson. R. : *Insights From Simulations Of Star Formation*; Rep. Prog. Phys. 70: 330 (2007)

[119] Lattanzio, J., Monaghan, J., Pongracic, H & Schwarz, M.: *Interstellar Cloud Collisions*; MNRAS 215: 125 - 47 (1985)

[120] Lattanzio, J & Monaghan, J. : *SPH And Star Formation History*; Mem. S.A. It, 65: 985 - 90 (1994)

[121] Ledoux. P. : *Sùr la Stabilitè gravitationnelle dùne nèbuleuse isotherme*; An. Ap. 14: 438 (1951)

[122] Lefloch, B., Cernicharo, J & Pardo, J.: *Star Formation In TRifid Nebula* AA 489: 157-71 (2008)

[123] Li, Z & Nakamura, F. : *Cluster Formation In Protostellar Outflow-Driven Turbulence*; ApJ 640(2): L187 - L190 (2006)

[124] Low, C & Lynden - Bell, D. : *The Minimum Jeans Mass*; MNRAS 176: 367 - 90 (1976)

[125] Lubow, S & Pringle, J. : *Magnetic Reconnection And Star Formation In Molecular Clouds* ; MNRAS 279: 1251 - 1262 (1996)

[126] Lucy, L. : *A Numerical Approach To The Testing Of The Fission Hypothesis*; AJ 82 : 1010 - 24 (1977)

[127] Makino. J. : *A Modified Aarseth Code For GRAPE And Vector Processors* ; PASJ 43: 859 - 876 (1991)

[128] Martin, C & Kennicutt Jr, R. : *Star Formation Thresholds In Galactic Disks* ; ApJ 555: 301- 21 (2001)

[129] Massey. P. : *The Stellar IMF* ; PASP Ed. Gilmore & Howell ASP Coference series, Vol. 142; p 17 (1998)

[130] Matthews, B & Wilson, C. : *Magnetic Fields In Star-Forming Clouds*; ApJ 531: 868 (2000)

[131] McCrea, W. : *Star Formation With Special Reference To Stellar Cluster*; Pro. Of Roy. Soc., London, 260, 1301, 152-59 (1961)

[132] McLow, M & Klessen, R. : *Control Of Star Formation By Supersonic Turbulence*; RvMP 76: 125 - 94 (2004)

[133] McMillan, S & Aarseth, S. : *An O(NlogN) Integration Scheme For Collisional Stellar Systems*; ApJ 414: 202 - 212 (1993)

[134] Meglicki, Z., Wickramasinghe, D & Bicknell, G. : *3D Structure Of Truncated Acrretion Disks In Close Binaries* ; MNRAS 264: 691 - 704 (1993)

[135] Mestel. L. : *Problems Of Star Formation - I*; QJRAS 161 - 98 (1965)

[136] Meyer, M & Lada, C. : *The Stellar Populations In L1630 (Orion B) Cloud. In 'The Orion Complex Revisited'*, ASP Conf. Ser. Ed. McCaughrean, M

[137] Miller, G & Scalo, J. : *The IMF And Stellar Birthrate In The Solar Neighborhood*; ApJS 41: 513 - 47 (1978)

[138] Monaghan, J. & Gingold, R. : *Shock Simulation By The Particle Method SPH*; Jour. Comp. Phys. 60(2): 253 - 62 (1985)

[139] Monaghan J. : *Smoothed Particle Hydrodynamics*; Ann. Rev. AA 30:543 - 74 (1992)

[140] Monaghan J. : *SPH and Riemann Solvers* ; Jour. Comp. Phy. 136: 298 - 307 (1997)

[141] Monaghan J.: *A Switch To Reduce SPH Viscosity*; Jour. Comp. Phy. 136: 41 - 50 (1997)

[142] Monaghan J. : *Smoothed Particle Hydrodynamics*; Rep. Prog. Phys. 68: 1703 - 1739 (2005)

[143] Nutter, D & Ward - Thompson, D. : *A SCUBA Survey Of Orion - The Low Mass End Of the CMF*; MNRAS 374, 1413 - 20 (2007)

[144] Ostriker, J. : *he Equilibrium of Polytropic and Isothermal Cylinders* ApJ, 140, 1056 (1964)

[145] Parzen. E. : *Modern Probability Theory And Its Applications* ; John Wiley Pub. Inc. (1960)

[146] Parzen. E. : *On Estimation Of Probability Density Function Ans Its Mode* ; Ann. Mat. Stat. 33: 1065 - 1076 (1962) Passot, T., Vàzquez-Semadeni, E & Pouquet, A.: *A Turbulent Model For The Interstellar Medium*; ApJ 455, 536 (1995)

[147] Penston. M. : *Dynamics Of Self Gravitating Gaseous Spheres III...*; MNRAS 144: 425 - 48 (1969)

[148] Pikelner. S. : *Energy Dissipation, Heating and Ionisation In The Interstellar Gas Due To Shock Waves*; Soviet Astron., 1, 310 (1957)

[149] Potter. D. : *Computational Physics*; John Wiley Pub Inc. (1966)

[150] Price. D. : *PhD Thesis*; (2004)

[151] Price, D & Monaghan, J. : *An Energy Conservation Formalism For Adaptive Gravitational Force Softening In SPH And N - body Codes*; MNRAS 374: 1347 - 58 (2007)

[152] Price, D & Bate, M. : *The Impact Of Magnetic Fields On Single And Binary Star Formation*; MNRAS 377, 77, (2007)

[153] Price *et. al* : *Dynamical Interactions Between YSOs & Collisional Model For Origin Of Stellar Mass Function*; MNRAS 273: 1041 - 68 (1995)

[154] Price. D. : *Modelling Discontinuities And K-H Instabilities In SPH* ; astroph/ 0709.2772 (2007)

[155] Price. D. : *SPLASH : An Interavtive Visualisation Tool For SPH Simulations* ; PASA 24(3) : 159 - 73 (2007)

[156] Pudritz, R. : *Clustered Star Formation & Origin Of Stellar Masses*; Science 295: 68 - 75 (2002)

[157] Rajaraman. V. : *Computer Programming In FORTRAN 77* ; Prentice-Hall (EEE) Pub. (1997)

[158] Raichoudhari. A. : *The Physics Of Fluids And Plasmas* ; Cambridge University Press, chapters (3), (6), (7) (1999)

[159] Ramsay, A. : *Theory Of Newtonian Attraction*; Cambridge University Pub., 1961

[160] Rees. M. : *Opacity Limited Heirarchical Fragmentation ...* ; MNRAS 176: 483 - 86 (1976)

[161] Reipurth, Bo & Bally, J. : *Herbig-Haro Flows*; Ann. Rev. AA 39: 403-55 (2001)

[162] Roberts. W. : *Large Scale Shock Formation In Spiral Galaxies And Its Implications On Star Formation* : ApJ 158: 123 - 43

[163] Rosolowsky. E. : *The Mass Spectra Of GMCs In The Local Group*; Pub. Of The Astronomical Soc. Of The Pacific 117: 1403 - 10 (2005)

[164] Sagar, R & Richtler, T. : *Mass Functions Of Five Young LMC Star Clusters*; AA 250: 324 - 39 (1991)

[165] Salpeter. E.: *The Luminosity Function And Stellar Evolution*; ApJ (1955)

[166] Sastry. S. : *Introduction To Numerical Analysis* ; Prentice-Hall (EEE) Pub. (1998)

[167] Shore. S. : *Astrophysical Hydrodynamics*; John Wiley Inc, chapter (6) (2007)

[168] Shu *et al* : *Galactic Shocks In An Interstellar Medium With Two Stable Phases*; ApJ 173: 557 - 92 (1972)

[169] Shu. F. : *Self Similar Collapse Of Isothermal Spheres and Star Formation*; ApJ 214: 488 - 97 (1977)

[170] Shu, F., Adams, F. & Lizano, S.: *Star Formation In Molecular Clouds: Observations And Theory*; Ann. Rev. AA 25: 23-81 (1987)

[171] Simon. R. : *Gravitational Instability In The Isothermal Stratified Nebula*; An. Ap. 28: 40 (1965)

[172] Sodrosky. T. : *The Physical Properties Of GMC Complexes In Outer Galaxies..*; ApJ 366: 95- 106 (1991)

[173] Solomon *et al* : *Mass, Luminosity And Line Width Relations Of Galactic Molecular Clouds*; ApJ 319: 730 - 41 (1987)

[174] Spitzer. L (Jr) : *Nebulae & Interstellar Matter*; ed. by Middlehurst. B & Lawrence. A, Chicago University Press, chap. 1 (1968).

[175] Spitzer. L (Jr) : *Physical Processes in The Interstellar Medium*; John Wiley Pub. Inc. (1972)

[176] Stahler, S & Palla, F. : *The Formation Of Stars*; Wiley-VCH Pub. (2004)

[177] Steinmetz, M & Müller, E. : *On The Capabilities And Limits Of SPH* ; AA 268: 391 - 410 (1993)

[178] Stevens *et al*: *Colliding Winds From Early Type Stars In Binary Syatems*; ApJ 386: 265 - 87 (1992)

[179] Stone. M. : *Collisions Between HI Clouds I: ...*; ApJ 159: 277 - 92 (1970)

[180] Stone. M. : *Collisions Between HI Clouds II: ...*; ApJ 159: 293 - 307 (1970)

[181] Strickland, R & Blondin, J. : *Numerical Analysis of the Dynamic Stability of Radiative Shocks* ApJ 449: 727 - 38 (1995)

[182] Stutzki *et al* : *On The Fractal Structure of Molecular Clouds* ; AA 336: 697 - 720 (1998)

[183] Taylor, C & Wilson, C. : *CO Observations Of Individual GMCs In M81*; ApJ 494: 581 - 86 (1998)

[184] Thomas, P & Couchman, H. : *Simulating The Foramtion Of A Cluster Of Galaxies*; MNRAS 257: 11 - 31 (1992)

[185] Usami, M., Hanawa, T. & Fujimoto, M. : *High-velocity Oblique Cloud Collisions And Gravitational Instability Of A Shock-Compressed Slab With Rotation And Velocity Shear*; PASJ, 47, 271 - 85 (1995)

[186] Vishniac. E. : *Dynamic & Gravitational Instabilities Of Spherical Shocks*; ApJ 274: 152 - 67 (1983)

[187] Vishniac. E.: *Shock Bounded Slabs*; ApJ 428: 186 - 208 (1994)

[188] Von - Neumann, J & Rictmeyer, R. : *A Method For The Numerical Calculation Of Hydrodynamic Shocks*; Jour. Of App. Phy 21: 232 - 38 (1950)

[189] Whitworth *et al* : *Fragmentation Of Shocked Interstellar Gas Layers*; AA 290: 421 - 27 (1994)

[190] Whitworth *et al* : *Binary Star Formation : Accretion - Induced Rotational Fragmentation*; MNRAS 277: 727 - 46 (1995)

[191] Whitworth, A., Bhattal, A., Francis, W & Watkins, S. : *Star Formation And The Singular Isothermal Sphere*; MNRAS 261, 1063 - 71 (1996)

[192] Whitworth, A & Stametellos, D. : *The Minimum Mass For Star Formation & The Origin Of Binary Brown Dwarfs*;AA 458: 817 - 29 (2006)

[193] Williams, J & McKee, C. : *Star Formation Thresholds In Galactic Disks*; ApJ 363: 435 (1997)

[194] Wolfire, M., Hollenbach, D. & McKee, C. : *The Neutral Atomic Phases Of The ISM*; ApJ 443: 152 - 68 (1995)